January 2012

Optimization of Bio-Impedance Sensor for Enhanced Detection and Characterization of Adherent Cells

Dorielle T. Price
University of South Florida, dorielle@mail.usf.edu

Scholar Commons Citation

Price, Dorielle T., "Optimization of Bio-Impedance Sensor for Enhanced Detection and Characterization of Adherent Cells" (2012). *Graduate Theses and Dissertations.*
http://scholarcommons.usf.edu/etd/4208

Optimization of Bio-Impedance Sensor for Enhanced Detection and Characterization of Adherent Cells

by

Dorielle T. Price

A dissertation submitted in partial fulfillment
of the requirements for the degree of
Doctor of Philosophy
Department of Electrical Engineering
College of Engineering
University of South Florida

Co-Major Professor: Shekhar Bhansali, Ph.D.
Co-Major Professor: Andrew Hoff, Ph.D.
Mark Jaroszeski, Ph.D.
Meera Nanjundan, Ph.D.
Stephen Saddow, Ph.D.
Shivshankar Sundaram, Ph.D.

Date of Approval:
November 22, 2011

Keywords: spectroscopy, ECIS, microelectrode, cancer cells, microfluidics

Acknowledgements

I would like to thank all the individuals, families, organizations, and fellowship programs that have supported me through this process. I was financially supported by the Ford Foundation (Predoctoral) Fellowship Program, NSF Graduate Research Program, McKnight Doctoral Fellowship (Florida Education Fund), and NSF's Bridge to the Doctorate Program. Thank you to my church family at First Baptist Church of College Hill for encouraging me and providing me with moral and spiritual support (along with great Sunday dinners and babysitting). To the BD family, thank you for your endless support, listening ears, and stress-relieving events. I obtained academic guidance and support from my advisor Dr. Shekhar Bhansali. I would like to thank him for bringing me on as a researcher in his group, developing me into a well-rounded student/researcher, and teaching me to always look at the "big picture". Thanks to Bernard Batson for all of his help in proposal writing, resume and professional development, and financial aid. Thank you to all of my committee members for their support and for taking the time to serve on my committee. And I would like to thank Dr. Frances Ligler for allowing me to join her research team for a semester at the Naval Research Lab.

Thank you to my husband, Tony Price, for his love, support, encouragement, and hard work through this entire process. To my sons, Tre and DJ, thank you for inspiring me to develop a work-family-life balance, and for pushing me to finish up the doctoral process. Last but not least, I would like to thank my late grandma (Beulah), parents (James and Dorothy), sister (Jamelah), and family for encouraging me and instilling in me the importance of education and a solid work ethic.

Table of Contents

List of Tables

List of Figures

Abstract

This research focuses on the detection and characterization of cells using impedance-based techniques to understand the behavior and response of cells to internal/environmental changes. In combination with impedimetric sensing techniques, the biosensors in this work allow rapid, label-free, quantitative measurements and are very sensitive to changes in environment and cell morphology. The biosensor design and measurement setup is optimized to detect and differentiate cancer cells and healthy (normal) cells. The outcome of this work will provide a foundation for enhanced 3-dimensional tumor analysis and characterization; thus creating an avenue for earlier cancer detection and reduced healthcare costs.

The magnitude of cancer-related deaths is a result of late-diagnosis and the fact that cancer is challenging to treat, due to the non-uniform nature of the tumor. In order to characterize and treat individual cells based on their malignant potential, it is important to have a measurement technique with enhanced spatial resolution and increased sensitivity. This requires the study of individual or small groups of cells that make up the entire tissue mass.

The overall objective of this research is to optimize a microelectrode biosensor and obtain statistically relevant data from a cell culture using an independent multi-electrode design. This would provide a means to explore the feasibility of electrically characterizing cells with greater accuracy and enhanced sensitivity.

Chapter 1 Introduction

This research focuses on the detection and characterization of cells using impedance-based techniques to understand the behavior and response of cells to internal/environmental changes. The biosensors in this work, unlike the patch clamp technique, use whole cells in culture as the primary transducer to detect a change in environment or physiological conditions. In combination with impedimetric sensing techniques, they allow rapid, label-free, quantitative measurements and are very sensitive to changes in environment and cell morphology. This research optimizes the biosensor design and measurement setup in order to detect and differentiate cancer cells and healthy (normal) cells. The outcome of this work provides a foundation for enhanced 3-dimensional tumor analysis and characterization; thus creating an avenue for earlier cancer detection and reduced healthcare costs.

1.1 Motivation

Cancer diagnosis and treatment in healthcare is a major area of concern in the United States today. Billions of dollars are being spent annually on medical research in order to develop devices and strategies to prevent, detect, and/or cure cancer and other illnesses. Annually, nearly 1 in 4 deaths are due to cancer [18, 19]. The four most common cancers include breast (women), prostate (men), lung and bronchus (men and women), and colon and rectum (men and women). The magnitude of cancer-related deaths is a result of late-diagnosis and the fact that cancer is challenging to treat, due to the non-uniform nature of the tumor. All cancer cells do not have equal malignant or invasive potential and thus need to be uniquely treated [20]. In order to characterize and treat individual cells based on their malignant potential, it is important to have a measurement technique with enhanced spatial resolution and increased sensitivity. This requires the study of individual or small groups of cells that make up the entire tissue mass. This research investigates methods to enhance cancer cell detection and provide fundamental information about cancer cell characteristics, through the design and optimization of a whole-cell biosensor and impedance-based measurement techniques. This research has the potential to advance drug discovery and ultimately lead to implementation of personalized healthcare.

1.2 Problem Definition

Successful development of the impedance biosensor will provide a means to electrically differentiate normal and cancer cells and quantify toxicology studies. Chemotherapeutic drugs, for instance, require extensive characterization and validation before they can be used clinically. This can be a cumbersome task, as many variables are present when determining the effectiveness of a drug, including concentration, time, cell line, and microenvironment. Qualitative methods, such as the use of biomarkers, light microscopy, staining, scanning electron microscopy (SEM), western analysis, are typically used to identify and validate chemotherapeutic drugs. However, such methods are time consuming and labor intensive.

Impedance spectroscopy, as a quantitative measure, can be used as a prerequisite tool to refine or design qualitative experiments by pinpointing specific time frames and drug concentrations; thus removing much of the guess-work and excess experimental trials. Long-term, continuous impedance measurements can capture the reactions of the cells to a stimulant at numerous time points. Thus, when a reaction is observed, qualitative measurements can be performed at that specific time point(s) to probe for further information. Impedance measurements can also aid in obtaining fundamental information about cellular responses and behaviors.

Repeatability, accuracy, spatial resolution, and high signal-to-noise ratios are required to successfully implement bioimpedance measurements for cell differentiation and toxicology studies. Therefore, this work aims to address these problems through electrode design optimization, designing multi-electrode devices, and automating data collection and analysis for large data sets.

1.3 Research Objectives

The objective of this research is to optimize a microelectrode biosensor and obtain statistically relevant data from a cell culture using an independent multi-electrode design. This would provide a means to explore the feasibility of electrically characterizing cells with greater accuracy and enhanced sensitivity. The specific objectives include:

a) Investigate the effect of electrode geometry on bioimpedance measurements

b) Explore methods to reduce measurement parasitic and enhance spatial resolution

c) Characterize and differentiate normal and abnormal cells

1.4 Dissertation Structure

Chapter 2 of the dissertation provides background information cancer, electromagnetic techniques, cell characterization techniques, impedance spectroscopy theory and modeling, and biological dispersion.

Chapter 3 describes the state-of-the-art and applications of impedance spectroscopy, including a comparison of this work's optimized electrode devices to existing commercial impedance systems.

Chapter 4 details the optimization of a microelectrode sensor design to eliminate the parasitic effects of the passivation coating. A design rule was derived to apply to future microelectrode designs.

Chapter 5 explores the use of the 4-electrode measurement setup to compare measurement sensitivity between the 2- and 4-electrode configurations in a microfluidic system.

Chapter 6 describes the optimized 8-electrode device and measurements performed on ovarian cancer cells.

In chapter 7, the commercial ECIS instrument was used to compare healthy and cancer ovarian cells, and validate measurements using the 8-electrode device.

Chapter 2 Background

The word cancer has been used by some researchers to describe both benign and malignant tumors; others have reserved the word specifically for malignant tumors [21]. In this research, the term ‘cancer’ will refer to malignant tumors and the term ‘abnormal’ will generally refer to both benign and malignant tumors. A tumor is defined as a mass of cells. Benign tumors do not invade local tissues and are generally harmless. Malignant tumors invade adjacent tissues and can spread throughout the body, causing deterioration or death. In general, tumor masses are less organized and structured than normal tissues. There are various degrees of abnormality of cells within tumors. Slightly abnormal tumors can contain only an excessive amount of cells, whereas in more abnormal tumors, the cells take on an irregular appearance. These cytological changes may include variability in the nuclear size, increased mitotic activity, and lack of cytoplasmic features [21]. Morphological changes in cells can be detected through impedance measurements, as changes in the structural features alter or restrict the path of the applied electrical signal. These structural changes in individual cells have a major impact on the tumor mass as a whole. In order to understand the functionality of a more complex tumor mass, small groups of cells will first be studied and characterized separately in this research.

2.1 Electromagnetic Techniques

The biosensor used in this work is a form of electromagnetic sensor. Medical imaging using electromagnetic waves, including X-rays and magnetic resonance imaging (MRI), has been traditionally used for many decades to detect abnormalities in tissues. The first medical use of X-rays occurred in 1896 [22] and over a century later, X-ray mammography is currently the standard screening technique for breast cancer. These techniques are well-established and are conducted across a wide frequency range. MRIs are performed between a few to hundreds of megahertz and X-rays are performed within 10^{16} and 10^{19} Hz. Electrical impedance tomography (EIT) and microwave imaging (MI) are newer technologies that are still in their trial stages. Figure 2-1 shows some of the most common electromagnetic medical imaging techniques and the frequency ranges in which they operate. This research expands on the existing technologies by increasing the traditionally used frequency spectrum and determining if additional information can be obtained to complement the existing techniques.

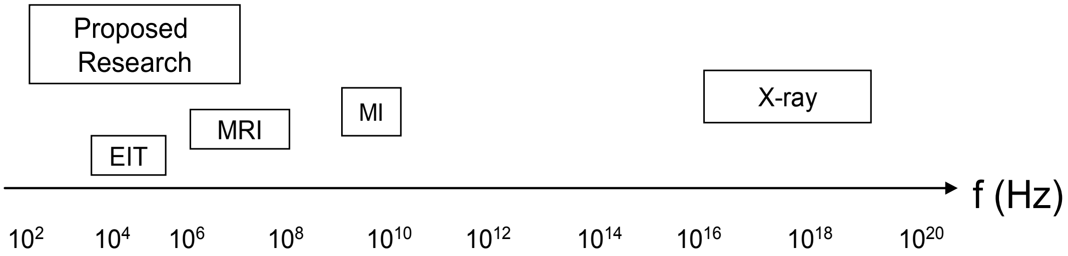

Figure 2-1: Frequency spectrum of electromagnetic medical imaging techniques

X-ray, MRI, EIT, and MI are all techniques used to image bone density, soft tissues, and/or organs. This research, however, begins with the study and characterization of cells, the foundation of these more complex structures.

Impedance spectroscopy is not the only known method of characterizing cells in culture. There are many existing methods that are used to study and characterize cell cultures, including but not limited to the use of electrochemistry/biomarkers, microscopy and fluorescence.

2.2 Cell Characterization Techniques

Conventional methods used in cancer cell biology include fluorescent imaging and radioactive detection; however, these techniques are costly, labor-intensive, and unable to provide continuous monitoring [23]. Optical microscopy is also standard practice used by pathologists or clinicians trained to identify suspicious regions or morphologies. Although reliable, this technique is qualitative and highly dependent on the expertise and experience of the clinician. In addition, such human resources are not always readily available, especially in areas with limited healthcare resources. Although these techniques are well-studied and widely used, they do not fit the criteria of being cost efficient, automated, and objective, as does the proposed sensor.

Biomarkers are indicators of normal biological processes, pathogenic processes, or pharmacologic responses; and they can be used for classification and staging of diseases, monitoring of clinical responses, and as diagnostic tools [24]. Biomarkers are typically associated with proteomics and genomics, the large-scale study of proteins and DNA/RNA respectively. Despite their great potential, only a few biomarkers are being used clinically due to the long and difficult path from discovery to clinical assay. Successful biomarker detection requires high sensitivity and high specificity, and the use of several biomarkers is often required to obtain such standards. Small sample sizes also make it probable that many protein biomarker candidates will be false positives [25].

Generally, the methods employed to study cellular properties could be classified into three major categories: microscopy/optical, biochemical, and electrochemical methods. In the abovementioned microscopic and biochemical methods, the protocols considered are known as endpoint assays. They provide a one-time analysis about a cell system at the end of an observation point. They require pre-labeling, post-labeling, and fixation. Optical techniques are limited by the use of expensive and bulky equipment that is not suitable for miniaturized, low-cost, automated systems [26]. In cases where the sample needs to be modified in order to obtain measurements, unknown, adverse effects could be imposed on the cells.

Alternatively, electrochemical sensors are inexpensive, sensitive, simple, and easily miniaturized. An electrochemical biosensor converts a biological recognition event to an electrical signal. Two of the most commonly used transducers are amperometric and potentiometric [27]. Amperometric biosensors apply a constant potential and monitor the current associated with the reduction and oxidation processes. They have been used to monitor and detect oxygen, glucose, nitric acid, adenosine triphosphate (ATP), and many more such analytes. However, lack of selectivity is a common disadvantage of amperometric cell biosensors [28]. Potentiometric biosensors convert the biorecognition process into a change in potential signal as a result of due to ion accumulation or depletion at the electrode surface [27, 28]. A limitation of this type of transducer is that it requires a very stable reference electrode [28].

Another electrochemical technique, normally placed in a category of its own, is electrochemical impedance spectroscopy (EIS). It can be separated into 2 different categories: non-faradaic and faradaic. Non-faradaic EIS describes a system in which a small AC signal is applied at equilibrium. The response is linear, and no charge-transfer reactions occur within the electrochemical system. A common *non-faradaic* EIS technique is Electrical cell-substrate impedance spectroscopy/sensing (ECIS), which will be discussed later in further detail. In *faradaic* EIS, electrons are transferred across the metal-solution interface, causing oxidation and reduction to occur. The cells create a barrier between the redox probe and the electrode surface, thus increasing the electron transfer resistance (R_{et}), which is related to the number of cells present (or change in number of cells due to proliferation or apoptosis) and changes to the electrode surface [28]. Faradaic EIS is a simple method for continuous monitoring of cell numbers; however, the recognition complex often leads to minute or undetectable changes in interface impedance, resulting in reduced reproducibility [28].

Non-faradaic impedance spectroscopy was chosen for this research due to its sensitivity, simplicity, cost-efficiency, and non-invasive properties, with a wide-range of applications (i.e. monitor cellular viability, morphology, adhesion, cell number, proliferation, apoptosis, and screening of medicinal compounds in drug development). Impedance spectroscopy may be combined with the abovementioned techniques to improve selectivity and sensitivity. Throughout the remainder of this text, the term impedance spectroscopy or sensing (IS) will refer to non-faradaic EIS, unless otherwise specified.

2.3 Impedimetric Measurement Theory

Electrical impedance measurement technique has the following advantages with respect to cell measurements: (1) small, non-destructive applied voltage signals, (2) ability to provide quantitative information about cell morphology, motility, attachment and spreading, mitosis, and apoptosis, and (3) sensitive measurements in a label-free and mediator-free environment.

This research implements the use of impedance sensing due to the above mentioned advantages, as well as (1) the ease of incorporation into a portable system, (2) the potential to be cost efficient, and (3) the ability to automate long-term measurements and data analysis. EIS can be used to characterize biological cells over a wide range of frequencies. Information about cell morphology, adhesion, and movement is obtained at low- to mid-range frequencies since most of the current flows around the dielectric cell membrane. At higher frequencies, the current penetrates the membrane and provides information about the cell interior. This research implements the use of impedance spectroscopy due to the above mentioned advantages, as well as the ease of incorporation into a portable system, the potential to be cost efficient, and the ability to automate long-term measurements and data analysis.

Microfabricated electrodes have properties which are useful for a wide range of applications. The use of microelectrodes would improve the signal to noise ratio, with minimal loss of sensitivity. An electrode array would impart the required sensitivity as well as amplify any discernible electrical response. Such a platform could be easily tailored to offer adequate isolation of cells and their immediate environment, which reduces background biological noise and interference. Implementation of microelectrodes would facilitate sensitive detection of cellular responses to either external or internal stimuli.

The impedance data can be used to differentiate between cells without the need for cell markers, which can adversely modify the cells. This is a major advantage of IS; thus eliminating the need for pre- and post-processing of cells and providing rapid, quantitative analysis.

Bioimpedance measurements are performed with small applied signals to (1) realize non-invasive measurements of biological cells/tissues and (2) confine measurements within a pseudo-linear region [29].

2.3.1 Visualization and Equivalent Circuit Analysis

Once the impedance spectroscopy data is collected, it can be visualized in several ways. One of the most common forms of presentation is the bode plot of the impedance

Figure 2-2. In a bode plot, the magnitude of the impedance and phase is plotted as a function of frequency on a log scale. The bode plot explicitly shows the frequency at which each data point was taken. This form of data presentation can be used to extract the parameters of the measured system, such as solution resistance, electrode polarization impedance, and cell resistance and capacitance. A slope in the bode magnitude diagram accompanied by a change of phase in the bode-phase plot is referred to as a dispersion. Figure 2-2 illustrates an electrode system with and without the presence of cells. When there are no cells present, a single dispersion is seen; and when cells are present on the electrode surface, a second dispersion develops, relevant to cellular characteristics. In the absence of cells (electrode-electrolyte system), the low-frequency slope of the bode magnitude plot is representative of the electrode polarization impedance (or double layer capacitance); whereas the mid- to high-frequency plateau corresponds to the solution resistance. In this simulation, the double layer capacitance value is 35 nF and the solution resistance is 1.5 kΩ. At low frequencies, the phase is -90°, thus signifying a capacitive (double layer) component. The phase approaches 0° as the frequency increases, thereby denoting a transition to a resistive component. When cells are present in the system, there is a noticeable change in the mid-frequency range of the bode plot, as seen in Figure 2-2. The simulated cell layer capacitance and resistance values are 5 nF and 20 kΩ respectively. Parameters from these systems can be extracted using equivalent circuit models and complex nonlinear least squares (CNLS) fitting. The equivalent circuits for the systems with and without cells are shown in Figure 2-3.

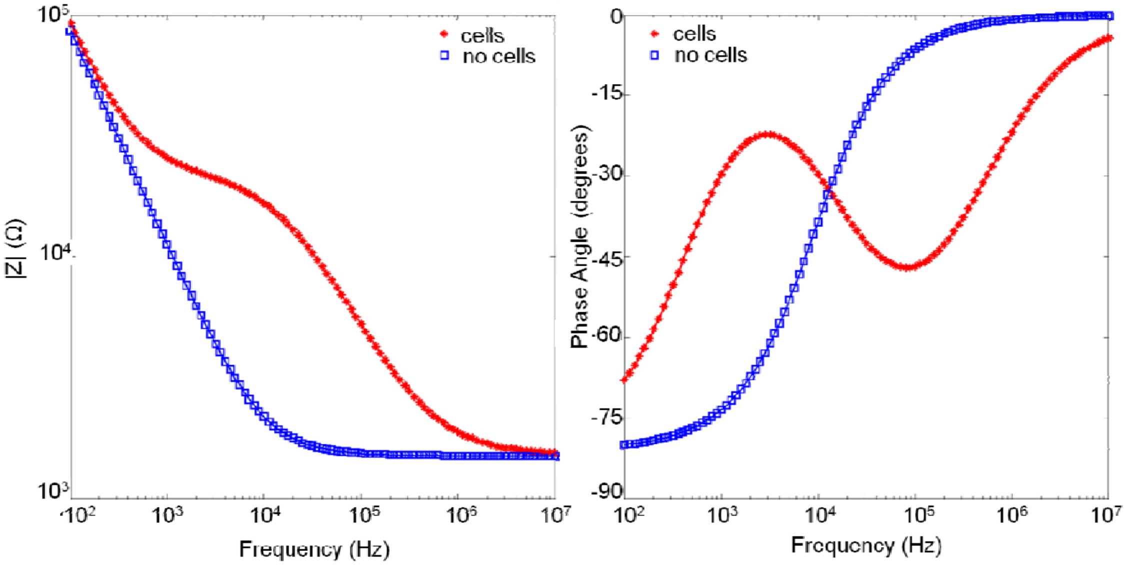

Figure 2-2: Bode plot simulating an electrode-electrolyte system and electrode-cells-electrolyte system

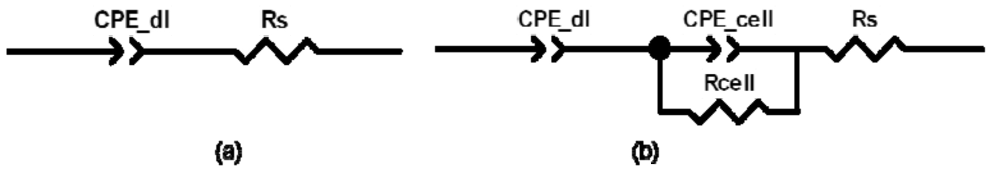

Figure 2-3: Equivalent circuits for systems (a) without cells and (b) with adherent cells

2.3.2 Constant-Phase Element (CPE)

The double layer capacitance at the electrode/electrolyte interface is not well-defined by an ideal, simple capacitor. A frequency dispersion exists at the interface; and therefore, capacitance is expressed as a constant-phase element (CPE). The CPE takes into account non-ideal properties such as surface roughness and heterogeneities, electrode porosity, coating composition, slow adsorption reactions, non-uniform potential and current distributions [30].

Equation 2-1 expresses the impedance of an ideal capacitor, as compared to Equation 2-2, which expresses the impedance of a CPE.

$$\boldsymbol{Z_C = \frac{1}{j\omega C}} \qquad \text{Equation 2-1}$$

$$\boldsymbol{Z_{CPE} = \frac{1}{Y(j\omega)^n}} \qquad \text{Equation 2-2}$$

where j = $\sqrt{-1}$, ω = 2πf, C is the ideal capacitance, Y is the CPE, and n is a factor between 0 and 1. When n = 1, Z_{CPE} = Z_C. The phase angle of Z_{CPE} is equal to –90*n in degrees.

2.3.3 Complex Non-Linear Least Squares Fitting (CNLS)

CNLS is a technique used to simultaneously fit data to a model (mathematical or equivalent circuit) of unknown parameters; and yields parameter estimates associated with the data. Advantages of this technique are that it provides uncertainty estimates to declare the “goodness of fit” of the estimated parameters; and very complex models with greater than 10 unknown parameters can be fit using this technique [31].

In CNLS, the sum of squares, SS, is minimized:

$$\mathbf{SS} = \sum\left(\mathbf{f_{exp}} - \mathbf{f_{th}}\right)^2 \qquad \text{Equation 2-3}$$

where f_{exp} is the experimental data and f_{th} is the theoretical model data, both as a function of frequency.

For a complex (impedance) data set,

$$\mathbf{SS} = \sum_{i=1}^{n}\left\{\left(\mathbf{Z}'_{i,exp} - \mathbf{Z}'_{i,th}\right)^2 + \left(\mathbf{Z}''_{i,exp} - \mathbf{Z}''_{i,th}\right)^2\right\} \qquad \text{Equation 2-4}$$

where Z’ and Z’’ are the real and imaginary components of the impedance, respectively, and n is the number of data points.

The aforementioned sum of squares is not weighted, also termed unity-weighted. To prevent the larger values from dominating the calculation of the sum of squares, weighting is performed when impedance values in a data set differ over several orders of magnitude. Equation 2-1 can then be re-written as

$$\mathrm{SS} = \sum\left\{\mathrm{w}\left(\mathrm{f}_{\mathrm{exp}} - \mathrm{f}_{\mathrm{th}}\right)^2\right\} \qquad \text{Equation 2-5}$$

where w is the weighting factor. There are multiple types of data weighting. Ideally, weights are determined by replicating experiments and calculating the experimental standard deviations

$$\mathrm{w}^{\mathrm{a}} = \frac{1}{(\sigma^{\mathrm{a}})^2} \quad , \quad \mathrm{w}^{\mathrm{b}} = \frac{1}{(\sigma^{\mathrm{b}})^2} \qquad \text{Equation 2-6}$$

where σ^a and σ^b are the experimental standard deviations, separated into two parts, for complex data (i.e. real and imaginary). Similarly, w^a and w^b are the weights, separated into two parts.

When replication is impractical, one can assume that the relative errors are constant, and the following relationship is applied.

$$\sigma^{\mathrm{a}} = \mathrm{f^a}_{\mathrm{exp}} \;, \quad \sigma^{\mathrm{b}} = \mathrm{f^b}_{\mathrm{exp}} \qquad \text{Equation 2-7}$$

Equation 2-7 is known as proportional weighting (PWT). In PWT, σ is proportional to the experimental data values.

Similarly, the theoretical value, f_{th}, can be used to determine the weight,

$$\sigma^a = f^a{}_{th} \ , \quad \sigma^b = f^b{}_{th} \qquad \text{Equation 2-8}$$

thus, this is known as function proportional weighting (FPWT) [32].

Another form of weighting is modulus weighting (MWT) or function modulus weighting (FMWT), in which σ is equivalent to the magnitude of the experimental and theoretical data, respectively. Modulus weighting is suitable when the magnitudes of the real and imaginary data values are similar across the entire data set; however, this is normally not the case [33]. In general, FPWT and FMWT lead to less biased data fitting than PWT and MWT; though PWT can me more reasonable than FPWT when one is uncertain about the fitting model [33]. FPWT is used in this work due to the drawbacks of the other weighting types and the use of established circuit models. This selection of weighting type was experimentally confirmed as the best weighting method for this work. The table below shows the different abovementioned weighting types applied to the same data sets of four different devices with and without confluent cells on the electrode surface.

Table 2-1: Comparison of weighting types on data sets.

MWT	**Rsp (kΩ)**	**Ydl (nF)**	**ndl**	**Rcell (kΩ)**	**Ycell (nF)**	**ncell**	**SS**
D1	1.25	1.96	0.95	6.65	39.12	0.66	7.32E-03
D2	2.41	2.12	0.91	-2.37	5.18	6.51	2.94E+00
D3	1.12	1.87	0.96	--	--	--	3.35E-02
D4	1.35	1.60	0.95	--	--	--	8.72E-02
Average							**7.66E-01**

FMWT	**Rsp (kΩ)**	**Ydl (nF)**	**ndl**	**Rcell (kΩ)**	**Ycell (nF)**	**ncell**	**SS**
D1	1.22	1.93	0.95	7.04	48.17	0.64	**5.82E-03**
D2	1.31	1.52	0.95	4.51	53.38	0.63	**2.44E-03**
D3	1.13	1.87	0.96	--	--	--	**3.33E-02**
D4	1.36	1.58	0.95	--	--	--	**8.51E-02**
Average							**3.17E-02**

PWT	**Rsp (kΩ)**	**Ydl (nF)**	**ndl**	**Rcell (kΩ)**	**Ycell (nF)**	**ncell**	**SS**
D1	1.26	1.88	0.95	7.00	38.91	0.66	**8.08E-04**
D2	1.34	1.55	0.95	4.08	33.97	0.66	**1.55E-03**
D3	1.11	1.74	0.96	--	--	--	**1.71E-02**
D4	1.34	1.53	0.95	--	--	--	**8.82E-02**
Average							**2.69E-02**

FPWT	**Rsp (kΩ)**	**Ydl (nF)**	**ndl**	**Rcell (kΩ)**	**Ycell (nF)**	**ncell**	**SS**
D1	1.22	1.91	0.95	7.35	54.67	0.64	**1.11E-03**
D2	1.36	1.58	0.95	3.97	29.69	0.67	**1.66E-03**
D3	1.11	1.81	0.96	--	--	--	**3.61E-02**
D4	1.15	1.58	0.95	0.25	13.99	0.79	**1.31E-03**
Average							**1.00E-02**

The devices consist of gold electrodes with 500μm-diameter sensors. D1 and D2 have confluent cell monolayers on the sensor surfaces, whereas D3 and D4 contain cells that are not yet confluent on the sensors. Details about the equivalent circuit model and extracted parameters will be explained later. From Table 2-1, it can be seen that FPWT yields the smallest error (weighted sum of squares), followed by PWT, FMWT, and lastly MWT, with the largest SS.

Applying the FPWT technique to calculate the sum of squares of impedance data yields

$$SS = \sum_{i=1}^{n} \left\{ \left[\frac{Z'_{i,exp} - Z'_{i,th}}{Z'_{i,th}} \right]^2 + \left[\frac{Z''_{i,exp} - Z''_{i,th}}{Z''_{i,th}} \right]^2 \right\} \qquad \text{Equation 2-9}$$

where n is the number of data points.

In CNLS fitting, ensuring that the minimum is found is a common issue. This problem has been addressed in [34] by implementing one program that usually converges, followed by a second program that uses the input of the first program. The second program converges only when a set of parameter values lead to an absolute or a good local minimum [31]. It is also recommended that data should be fitted in the form it was measured to reduce bias in the fitted results, caused by taking the inverse of data with errors [31]. In example, if the real and imaginary components of the impedance are measured, fitting should be done with the real and imaginary components and not the magnitude and phase components. A good fit is established when the relative standard deviations of the fitted parameters are less than 30% [31].

2.3.4 Biological Dispersions

Microelectrodes will be used in this work to perform IS measurements, which will provide frequency-dependent information about biological materials. Figure 2-4 shows a plot of the frequency dependence of relative permittivity and specific conductivity of biological tissue, reprinted from [35]. This plot shows three regions, originally defined by Schwan [36], as alpha (α), beta (β), and gamma (γ) dispersions, at low, mid, and high frequencies respectively. As measurement frequency increases, tissue conductivity increases and permittivity decreases.

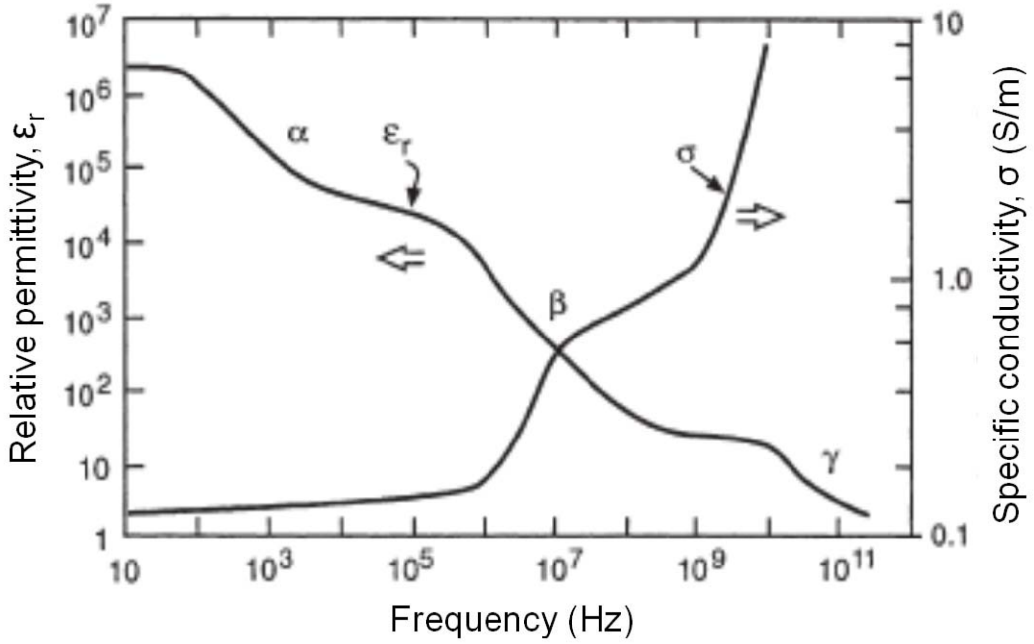

Figure 2-4: Frequency dependence of the relative permittivity and specific conductivity of complex biological tissue

Each of these dispersions is caused by a physical process. The alpha dispersion, which occurs below 10 kHz, is due to ionic diffusion in layers of the cell culture medium [37]. Within the beta dispersion region, between 1 MHz and 100 MHz, the electric field begins to penetrate the cell interior. According to Tamura et al., the beta-dispersion is dependent on the charging properties of the cell membranes, along with intra- and extra-cellular fluids [38]. Above 10 GHz (gamma dispersion), it has been shown that measured quantities tend to vary over frequency in proportion to the water content of the cells [39]. In this research, the region of interest is the beta dispersion in order to identify changes in cellular membrane structure.

2.3.5 Two- vs. Four-Electrode Impedance Measurements

The most common measurement configurations are performed with 2 and 4 electrodes. In 2-electrode measurements (primarily used in this research) current is passed and voltage and measured between the same set of electrodes. One electrode in the set is identified as the working electrode and the other, usually larger, electrode is named the counter electrode. If the area of the counter electrode is at least 300-times greater than the area of the working electrode, the impedance of the system is dominated by the impedance of the working electrode [14]; thus simplifying the analysis of the system. Alternatively, in 4-electrode measurements, current is passed through one pair of electrodes and voltage is measured between another pair. Normally, the voltage sensing electrodes are placed linearly between the current carrying electrodes. Both measurement configurations have advantages and disadvantage. For 2-electrode measurements, electrode polarization impedance, caused by the adsorption of electrolytic ions/molecules on the electrode surface, is geometry dependent. As electrode area decreases, the effect of electrode polarization impedance becomes greater, causing relevant data to be masked at lower frequencies. On the other hand, electrode polarization impedance has negligible effects 4-electrode measurements since the current passing and voltage sensing electrodes are separate. However, with this configuration, multi-electrode array configurations are not easily achieved for increased spatial resolution.

Impedance detection, using either configuration, can be performed continuously and long-term since the measurements are non-destructive and label-free. This research leverages on noninvasive, nondestructive, label-free characteristics of impedance measurements for long-term analysis of cells and their surrounding environment.

Chapter 3 State-of-the-Art and Applications of Impedance Spectroscopy

3.1 Impedance Detection of Normal and Abnormal Cells

Impedance measurements of adherent cells have been shown to detect changes in cell morphology on the order of nanometers [6], providing sensitivity much greater than that obtained through visual inspection. Cellular morphology is one of the most important parameters in cancer biology [23]. There are numerous examples in literature demonstrating a change in impedance with a corresponding change in the physical properties of cells [1, 2, 9, 40]. In general, impedance measurements can detect a change in cellular capacitance and resistance at the electrode interface. When cells attach and spread onto the surface of the electrode, the measured impedance increases because the cell membranes act as insulators and block current flow. A schematic of the current flow in tissue culture medium with and without cells is shown in Figure 3-1, from [41]. A small current is passed through the electrodes, thus making the measurements non-invasive and non-destructive.

Beginning in the 1920s with Frick and Morse, significant capacitive differences have been found between malignant breast tumors and normal tissues [42]. Due to increased cellular water and salt content, altered membrane permeability, and changed packing density, malignant tumors typically exhibited a lower electrical impedance [42]. Han et al. demonstrated that cancer cells at different stages had unique impedance signatures. Since the cell membrane of cancer cells are more permeable, a decrease in capacitance resulted, relative to the stage of cancer [43]. A study by Beetner et al. demonstrated differences between basal cell carcinoma (BCC), benign lesions, and normal skin using electrical impedance measurements. They noted that BCC had a larger nuclei and smaller intercellular spacing, causing a difference in measured impedance [44].

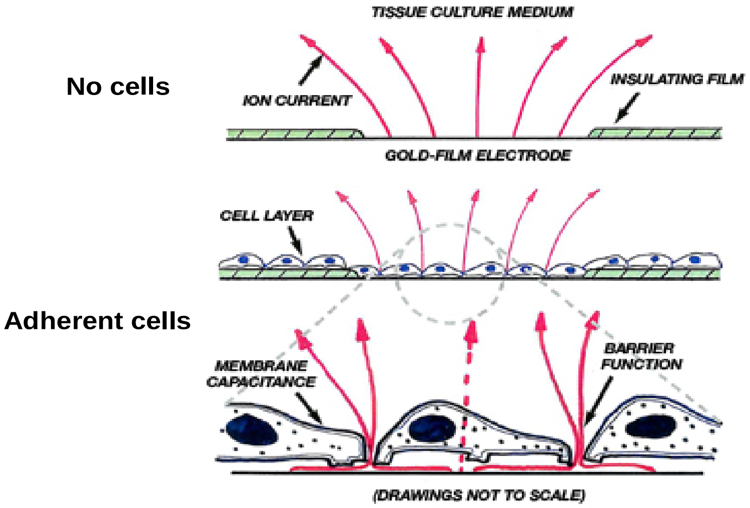

Figure 3-1: Schematic of current flow in tissue culture medium with and without cells present on electrode

The basis of this research originates from the findings of the abovementioned work, which verifies that there are measurable impedance differences between normal and cancer cells.

Some differential electrical characteristics between normal and cancer cells are summarized below:

- Cancer cells have a lower electrical membrane potential and lower electrical impedance than normal cells [45]
- Cancer cells have an accumulation of an excessive amount of negative charges on their exterior surface [46]

- Electrical conductivity and permittivity of cancerous cells is greater than that of normal cells [47]

In a controlled, static environment, cell characterization can provide fundamental information about cells' long-term behavior, functional characteristics, and growth-cycle. This fundamental information can prove to be invaluable with applications such as cancer research, toxicology and cytopathic studies, drug screenings, wound healing, personalized healthcare, and development of flow-through cell characterization systems. Development of a practical biosensor for cancer research requires (1) sensor design optimization, (2) configuration and optimization of measurement setup, and (3) sensitive detection and differentiation of cancer cells.

3.2 State-of-the-Art: Adherent Cell Characterization

The interactions between in vitro cells and substrates have been studied for many decades to obtain vital information about the condition of cells. Normal anchorage-dependent cells secrete extracellular matrix (ECM) proteins and proteoglycans that adhere to the substrate to attain traction for migration and acquire signals for growth and differentiation from the ECM. Other cell functions such as gene induction, motility, wound healing, and tumor metastasis are all dependent on the binding of cells to ECM [48]. The study of cell-substrate interactions has applications in drug screenings, toxicity and cytotoxicity studies, cancer research, wound healing, and cytopathic studies.

Analysis of cell attachment using a microscope has been a commonly used technique; however the analysis is qualitative and performed at a single point in time. Cinematography is used to continuously record an event; however, data quantification is difficult and requires extensive data manipulation [49]. Some other quantitative methods that measure cell substrate interactions include quartz crystal microbalance (QCM), optical waveguide lightmode spectroscopy (OWLS), and electric cell-substrate impedance sensing/spectroscopy (ECIS) [50]. QCM monitors changes in resonant frequency of piezoelectric quartz crystals to measure cell adhesion, proliferation, and cytotoxicity. OWLS uses evanescent waves to monitor cell adhesion and proliferation.

A detailed review of these techniques, along with a few others, can be found in [51, 52]. OWLS and QCM, both being optical-based techniques, would add expense and complexity to the measurement setup. The use of ECIS-based measurements was chosen for this research due to its simplicity, ease of miniaturization, and wide range of applications.

3.2.1 Electric Cell-Substrate Impedance Sensing (ECIS)

ECIS was developed by Giaever and Keese in 1984 to study the electrical properties of adherent cells. A small, 250μm diameter, gold working electrode and a larger counter electrode is used in the two-electrode system. When cells attach and spread onto the surface of the electrode, the measured impedance increases because the cell membranes act as insulators and block current flow. The sensitivity of these measurements is on the order of nanometers [6], meaning that changes in morphology or micromotion can be detected on a nanoscale. A photograph of a commercial ECIS device is shown in Figure 3-2.

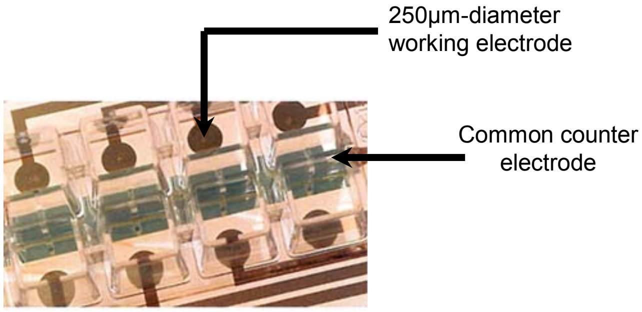

Figure 3-2: Photograph of commercial ECIS device

Equivalent circuit modeling and/or numerical analyses can be performed to quantify and monitor system parameters such as cell membrane capacitance, solution resistance, cell-cell junction resistance, and cell-substratum contact resistance. ECIS is very sensitive to micromotion, the constant movement of cells on the electrode surface driven by their microfilaments [8]. Therefore, small changes can be detected even before observations are visible under a microscope.

Applied Biophysics offers various electrode designs, including one with 2 independent working electrodes within a cell culture chamber, shown in Figure 3-3. It is a well-known and widely accepted technique; however, some of its shortcomings include limited frequency range and preset data points, and minimal spatial resolution. The high end of the frequency range is limited by the presence of the passivation layer over the unexposed gold traces. This results in a parasitic coating capacitance at higher frequencies, where current preferentially travels through the least resistive pathway [53]. Spatial resolution and statistically relevant data can be enhanced by implementing more independent working electrodes to obtain multiple impedance datasets within a cell culture chamber.

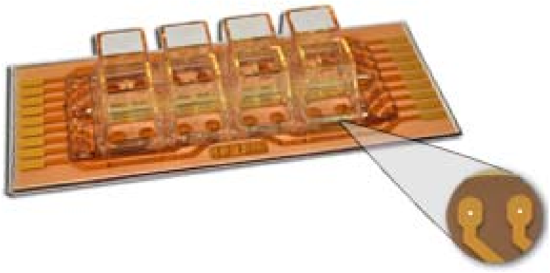

Figure 3-3: Applied Biophysics' ECIS device 8W2x1E

The final device described in this research contains 8 independent electrodes to improve statistical relevance of measured data and obtain information position-dependent data across the cell culture.

3.2.2 Applications of ECIS in Literature

Many studies have been performed in literature using ECIS to study the effects of toxin, drugs, and environmental changes on normal and cancerous cells [1, 2, 4-9, 11, 12, 15, 17, 54]. In general, when the adherent cells were faced with an adverse challenge (bacterial/viral infection, deprivation of glucose, induced apoptosis), they retract from the electrode surface and neighboring cells, causing a decrease in resistance and increase in capacitance. A review of this literature is summarized in Table 3-1. From the literature review, it has been shown that cells faced with various challenges can be identified using ECIS measurements. This research fills-in the gaps by optimizing electrodes for ECIS-based measurements and designing multi-electrode devices to obtain multiple data points from within a cell culture, resulting in statistically relevant data, to electrically characterize cells for subsequent microfluidic impedance sensing and 3-dimentional tumor spheroid cultures.

Table 3-1: Summary of relevant ECIS literature.

Cause / Challenge	Effect	Reference
(a) No challenge: studied micromotion of WI-38 VA13 and WI-38 fibroblastic cells (b) Added 10% formalin treatment to kill cells	(a) Derived a model to calculate the specific impedance of a cell-covered electrode, based on cell-free electrode impedance, membrane capacitance, and resistivity of medium (b) No fluctuation (micromotion)	Giaever, et al.; 1991, [2]
(a) Temperature (27°C and 37°C) (b) Deprivation of glucose (c) Cytochalasin D	(a) Decreased temperature decreases cell fluctuations (b) Reduced glucose reduced micromotion of cells (c) Decreased resistance due to morphological changes	Lo, et al.; 1993, [6]
Effect of applied electric fields	At 40 μA, microfilaments relax & move away from the surface (decreased resistance); at 200 μA, electroporation occurs	Keese, et al.; 1994, [8]
Microbial challenge: indigenous oral spirochete Treponema denticola, varying concentration	At highest concentration, initial increase in impedance was observed (cell swelling); Decreased micromotion and junctional resistance; relatively constant cell-substrate resistance	Ko, et al.; 1998, [10]
No challenge: resistance & capacitance of epithelial MDCK cells	Between 200 Hz & 5 kHz, resistance increased first due to attachment and spreading, then tight junctions; high-frequency (40 kHz) capacitance is most sensitive parameter for monitoring attachment & spreading	Wegener, et al.; 2000, [14]
Bovine aortic endothelial cells (BAECs) exposed to fluid flow (forces)	Sharp increase in resistance at flow onset; resistance decreased after 60 min. Capacitance slightly decreased at flow onset then increased after 10 min. until flow was removed Changes in capacitance (5%) were small compared to change in resistance (30%)	DePaola, et al.; 2001, [16]

Table 3-1 (Continued)

Addition of metastatic cell suspensions to confluent human umbilical vein endothelial cells	Endothelial cell junctions retracted; thus impedance decreased; Change in impedance correlated with the strength of the metastatic cells	Keese, et al.; 2002, [1]
Wounding of African green monkey kidney cells, NRK cells, MDCK cells with elevated current pulses (3V at 40kHz)	Wounding resulted in drop in resistance and increase in capacitance from 1 nF to 5 nF. Resistance increased back to level of cell-covered electrode after a few hours due to migration of cells	Keese, et al.; 2003, [3]
Addition of mercuric chloride at various concentrations	Cells died; Impedance decreased. Resistance changed as a function of cell attachment, spreading, mitosis, and cytotoxicity effect	Xiao, et al.; 2003, [5]
Induced apoptosis in porcine brain capillary endothelial cells (PBCECs) using cycloheximide (CHX)	25 μM CHX: Impedance decreased after ~30 min.; impedance reached cell-free value after 6 hours. Values for cell-cell resistance, cell-substrate resistance, & cell membrane capacitance were extracted	Arndt, et al.; 2004, [9]
Introduced toxins (tamoxifen and menadione) to Human hepatocellular carcinoma cell (HepG2)	Dead cells detached and impedance decreased. Change in impedance consistent with intensity of fluorescence using conventional fluorescent assays	Yeon, et al.; 2005, [12]
Addition of influenza A viral infection to MDCK cells	Cells became rounded and detached from surface. Impedance decreased in dose-dependent manner	McCoy, et al.; 2005, [15]
(a) Differentially coated surfaces (b) Integrin and actin cytoskeleton disrupting agent (c) Interfering with Src tyrosine kinase expression and activity	(a) Increase in cell index (resistance) correlated with cell attachment and spreading; able to distinguish adhesion quality (b) Function-blocking antibodies prevented cell attachment and spreading (c) Cell attachment and spreading was inhibited, indicated by decrease in cell index	Atienza, et al.; 2005, [17]

Table 3-1 (Continued)

CHSE-214 cells infected with infectious pancreatic necrosis virus (IPNV) EPC carp cells infected with infectious hematopoietic necrosis virus (IHNV)	Resistance increased with initial attachment and spreading. Resistance decreased & capacitance increased due to cell death ~ 50 hours after introduction of virus. Virus had no effect at room temperature; its effect was dose-dependent	Campbell, et al.; 2007, [4]
Aspirin added to HT-29 colon cancer cells after 24 hours	Inhibited HT-29 cell growth; Impedance decreased Changes most sensitive at 40 kHz	Yin, et al.; 2007, [7]
(a) No challenge: studied NCI-H460 cancer cell attachment on collagen (b) NCI-H460 concentration (1x10^4 vs. 3x10^4 cells/chip) (c) Effect of antibodies against β1 & α2β1-integrin	(a) Impedance change increased with time (b) 92-135% difference in impedance change when cell concentration increased; highest sensitivity reported (c) Increased antibody concentration decreased total impedance change	Chen, et. al; 2008, [11]
Wound edges formed using SAMs to inhibit cell adherence (a) Measured migration speed of 4 cell lines (CaSki, HeLa, Vero-E6, & NIH-3T3) with/without serum (b) Effect of migration inhibition agent (colchicine)	(a) Speed of migration significantly higher in media with serum; NIH-3T3 (fibroblast cells) showed the highest migration speed (b) Colchicine inhibited cell migration in a concentration-dependent manner	Wang, et al.; 2008, [13]

3.2.3 xCELLigence

The xCELLigence system, also known as the real-time cell electronic sensing (RT-CES) system, was developed in the early 2000’s. It has similar traits to the ECIS setup; though one major difference is that the xCELLigence system incorporates a circle-on-line electrode design that covers approximately 80% of the surface area of 16, 96, 384-well plate chambers [55]. Each individual electrode has a diameter of 90 μm, and the spacing between two rows of electrodes is approximately 10 μm. The design mirrors that of interdigitated electrodes. An image of the system and electrode, from the Roche Applied Science website (http://www.roche-applied-science.com/sis/xcelligence), is shown in Figure 3-4.

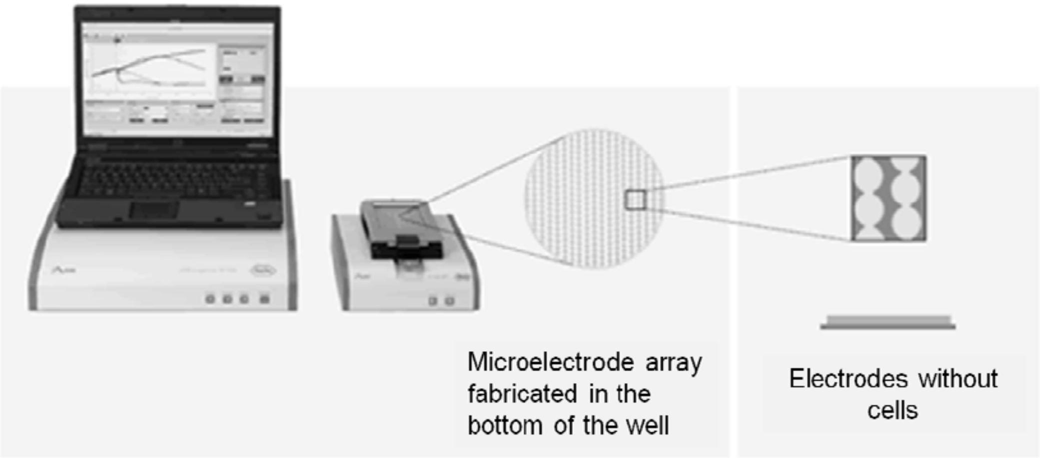

Figure 3-4: Photograph of xCELLigence system and enlarged image of microelectrode, circle-in-line design

This system uses a measure termed cell-index, (CI) which can be associated to monitor cell viability, number, morphology, and adhesion. The CI is a dimensionless number that is proportional to the ratio of the measured impedance with cells present and without cells. As cells attach and spread onto the electrodes, the CI increases from zero. Impedance measurements are taken at 10, 25, and 50 kHz, though 10 kHz is primarily used to calculate the cell index. CI is defined by the following equation:

$$CI = max_{i=1,\dots,N}\left[\frac{R_{cell(f_i)}}{R_{b(f_i)}} - 1\right] \qquad \text{Equation 3-1}$$

where R_{cell} and R_b is the frequency-dependent resistance when cells are attached and when no cells are attached, respectively [56]. Further reading and illustrations can be found in [57, 58]. Advantages of the optimized electrode design in this research include independent working electrodes, and impedance spectroscopy to characterize frequency-dependent system parameters.

3.2.4 Electrode Optimization

Impedance characterization of biological cells, using microelectrodes, is an emerging diagnostic tool for studying electrophysiological and biophysical changes due to viral infections [15], cancer detection [59], and drug response [60]. Microelectrodes offer many advantages over their conventional counterparts including: economy due to batch fabrication [61], small signal and large current densities (current per unit area) due to enhanced mass transport [62], and the ability to integrate electrodes with other instrumentation to develop portable measurement systems [63]. The small currents associated with microelectrodes have the potential to perform non-destructive measurements and facilitate the study of high resistivity samples [64].

There are also disadvantages associated with microelectrodes, commonly resulting in measurement error. At low frequencies, microelectrodes are challenged with interfacial polarization impedance in 2-electrode measurements. Interfacial, or double layer, capacitance is indirectly proportional to interfacial impedance and arises from the inability of charge carriers to move across the solid–liquid barrier [65]. The result of this barrier is accumulation of charges in response to an applied potential to the electrode; thus giving rise to a capacitive effect. Since capacitance is directly proportional to area, in the case of microelectrodes, this effect can lead to very large impedances, particularly at low frequencies.

Researchers have performed experiments to optimize the electrode designs for various applications. Fosdick and Anderson [66] optimized the geometry of a microelectrode array flow detector; with respect to amperometric response; and Min and

Baeumner [67] investigated geometric parameters (i.e. electrode height, material, gap size, and electrode width) of interdigitated ultramicroelectrode array (IDUAs) to optimize oxidation and reduction reactions of ferro/ferrihexacyanide. Sandison and coworkers [68] studied electrode sensor array geometry (center-to-center spacing and diameter) and porosity of electrode sensors using Si_3N_4-coated silicon substrate and Lempka and coworkers [69] optimized silicon-substrate microelectrodes for neural activity recordings.

While the aforementioned works studied the optimization of electrodes for flow detectors, neural recordings, and microfluidic biosensors; design rules for optimization of microelectrodes for ECIS-based measurements had received little attention in published literature. One example of ECIS-based optimization was performed by Wang and colleagues. They investigated the sensitivity and frequency characteristics of interdigitated array microsensors for ECIS [70]. Other studies have been performed for numerical optimization of cell data analysis [71], and determination of the most robust and sensitive cell lines for field-portable toxicology studies [72]. Part of this work focuses on optimizing ECIS-based electrodes to reduce measurement noise. The other part of this research uses this optimized electrode design to characterize and differentiate normal and cancer cells with enhanced detection sensitivity and statistically-significant data. This research will serve as a foundation for cancer cell characterization and detection.

Chapter 4 Electrode Optimization for High-Frequency Impedance Measurements

4.1 Introduction

As mentioned previously, microelectrode designs need to be optimized to reduce interfacial impedance as well as to extend the useful frequency probing range. One of the objectives of this research is to suppress these parasitics and optimize microelectrode design for ECIS-based measurements within the beta dispersion region. Electrode design optimization of microelectrodes is critical to the efficient employment of detection techniques in drug discovery, cancer research, and toxicology studies. Pejcic and De Marco [73] reiterate that sensor optimization is one of the most crucial steps in the realization of an electroanalytical device.

In this work, a design rule was derived for optimization of microelectrodes used in Electric Cell–Substrate Impedance Sensing (ECIS) up to 10 MHz [53]. Previous work [74], studying the effect of electrode geometry (sensor diameter), demonstrated the parasitic effects of the passivation coating at higher frequencies. The effect of electrode design (electrode area, lead trace widths, and passivation coating thickness) on the contribution of the passivation coating impedance was experimentally evaluated using Electrochemical Impedance Spectroscopy (EIS) measurements. The parasitic coating impedance was successfully minimized by designing electrodes with either a thicker coating layer or a smaller lead trace width. It was observed that passivated lead trace area to coating thickness ratio has a critical value of 5.5, under which the impedance contribution of the coating is minimized.

The optimized design of ECIS-based microelectrode devices reported in this work will make it possible to probe the entire beta dispersion region of adherent biological cell layers.

4.2 Fabrication

Gold microelectrode devices were fabricated on glass wafers using standard photolithography and metal deposition techniques. The fabrication process flow is illustrated in Figure 4-1 (a-f).

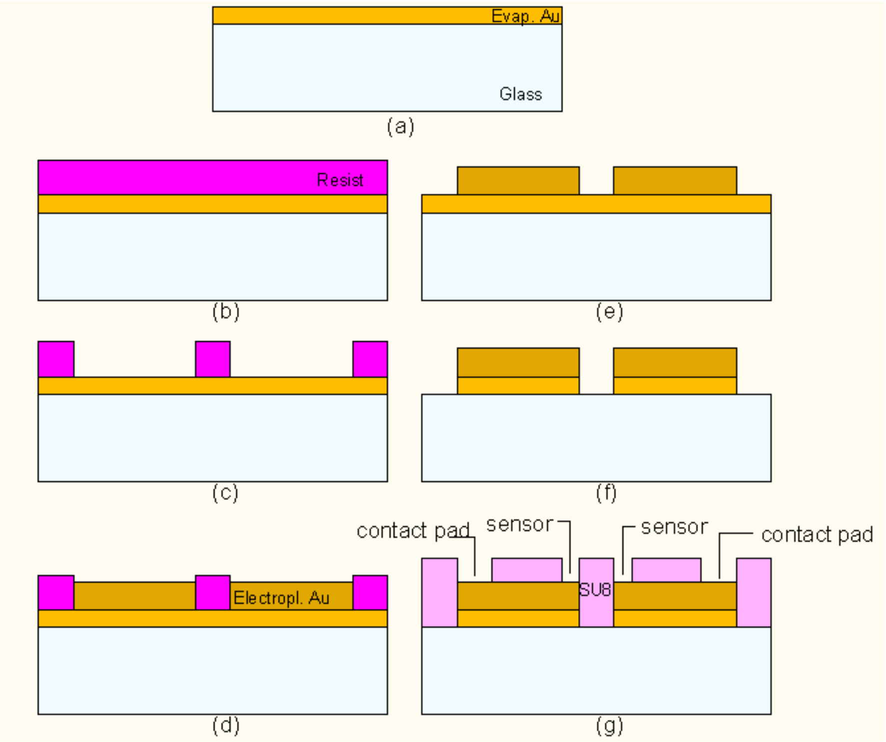

Figure 4-1: Fabrication process for microelectrode devices. (a) clean glass substrate and thermally evaporate chromium and gold layers; (b) apply and pattern photoresist; (c) electroplate gold onto uncovered electrode sensors, traces, and contact pads; (d) lift-off; (e) wet etch to remove evaporated gold and chromium; (f) apply and pattern photoresist to insulate the traces and expose the sensors and contact pads

Four-inch glass wafers were solvent cleaned (acetone and methanol) and dried with nitrogen. Chromium (200 Ǻ) and gold (1000 Ǻ) were thermally evaporated onto the wafers. Next, the wafers were solvent cleaned in preparation for the first of two photolithography steps. The first photolithography process, performed with NR1-3000PY (Futurrex) negative photoresist, opened patterns in the resist in the shape of the electrode device seen in Figure 4-3. 3000PY was spun at 3000 rpm for 30 seconds. The wafers were soft-baked on a hotplate for 1 minute at 155°C. (Note: the bake times are double the times typically seen on data sheets because the data sheets are optimized for silicon; however, glass, being insulating, requires longer bake times). The photoresist was exposed for 60 seconds using an EVG mask aligner, followed by a 2-minute post exposure bake at 110°C. Lastly, the resist was developed in RD6 (Futurrex) for 18 seconds. Subsequently, gold was electroplated onto the exposed evaporated gold. Electroplated gold is rougher than evaporated gold. The rougher surface increases the surface area of the electrode sensors and thus reduces the effect of the parasitic impedance caused by the double layer at low frequencies. Approximately 1 μm of gold was electroplated onto the evaporated gold, which acted as a seed layer. Electroplating was performed using RTU TG25E (Technic) gold plating solution. The solution was warmed to 55°C on a hotplate with a magnetic stirrer (Figure 4-2).

The negative terminal of a current source was connected to the wafer and the positive terminal was connected to a platinum mesh. The gold plating solution contains positively charged gold metal salt, which is attracted to the negatively charged wafer and reduced to metallic form. A 2 mA DC current was applied for 30 minutes, resulting in approximately 0.4 μm of gold. Profilometer measurements were completed before and after plating to confirm the height of the gold.

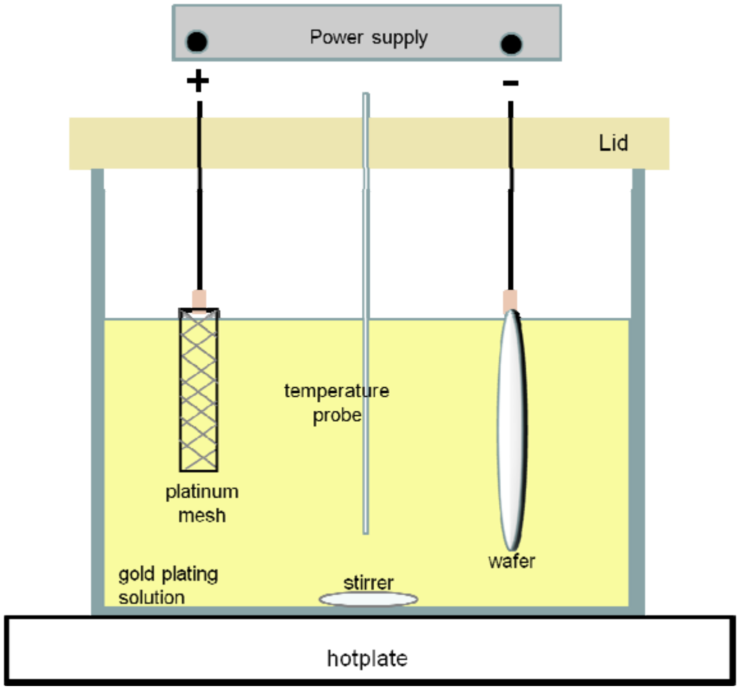

Figure 4-2: Schematic of electroplating setup

Next, the 3000PY photoresist was removed by solvent cleaning the wafers. The evaporated gold (seed layer) was removed via wet etching in gold etchant for approximately 20 seconds. The seed layer is removed; however, sufficient electroplated gold remains since the electroplated gold is 10 times greater than that of the evaporated gold. The chromium seed layer is subsequently removed by wet etching with a chromium etchant for approximately seven seconds. The wafers a solvent cleaned and prepared for the second photolithography step.

The wafers were diced into single devices and cloning cylinders were attached to serve as the electrolyte reservoir. The cylinders were centered and attached around the four sensors by slowly heated photoresist around the outer circumference of cylinder, using a hotplate.

Subsequently, the photoresist harden as it slowly cooled and to form a tight seal with few air pockets. Schematics of the 500 μm and 30 μm trace-width devices are illustrated in Figure 4-3.

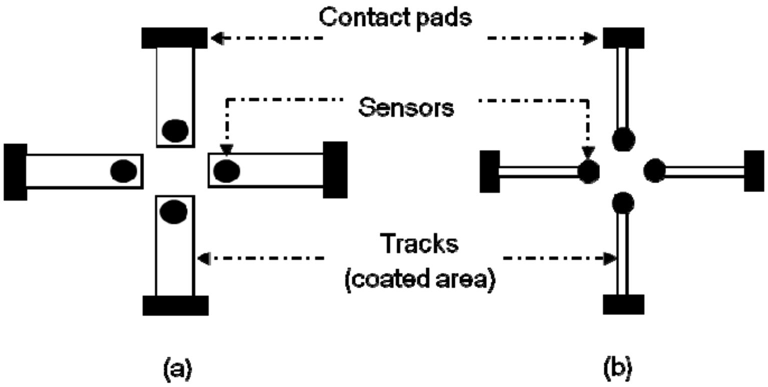

Figure 4-3: Top-view schematics of (a) 500μm and (b) 30μm trace-width devices

Electrode devices with different sensors diameters were fabricated for each trace width, using standard photolithography techniques. The 500 μm trace-width devices had sensor diameters of 500, 250, and 100 μm. The 30 μm trace-width devices had sensor diameters of 500, 250, and 125 μm.

4.3 Theory

Theoretically, capacitance decreases as area decreases, according to the following equation,

$$C = \frac{\varepsilon_o \varepsilon_r A}{d} \qquad \text{Equation 4-1}$$

where ε_0 is the permittivity of free space (8.85 x 10^{-12} F/m); ε_r is the relative permittivity of the polymer coating in this case (4-8); A is the area of the coated traces; d is the thickness of the coating.

Therefore, decreasing the polymer-covered trace area or increasing the thickness of the coating should decrease the coating capacitance. In previous work [74], experiments were performed on electrode devices with a 500 μm trace width and 2 μm-thick resist. The area of coating exposed to the electrolyte was approximately 1 mm^2, and the coating impedance appeared at approximately 1 MHz. This is a result of current flowing through the coating, a pathway of lower resistance at higher frequencies. To validate this theory, new electrode devices were designed and fabricated with a 30 μm trace-width; thus reducing the coating area to 7.65×10^{-2} mm^2, more than an order of magnitude smaller than the devices with a 500 μm trace width.

4.4 Effect of Increasing the Passivation Coating Thickness

Impedance measurements were performed on the 500 μm trace-width devices to investigate the effect of increasing the coating thickness on upper-frequency impedance measurements using potassium chloride (KCl) as the electrolyte. When the resist thickness was increased from 2 μm to 20 μm, there was a significant reduction in the coating impedance component. A comparison of measurements with 2 μm- and 20 μm–thick coatings is illustrated in the bode plot of Figure 4-4.

The coating impedance calculated at 10 MHz was less than the spreading resistance for the devices with 2 μm-thick coating for all sensor diameters; hence current flows through the coating as seen with the 250 μm sensor diameter, 2 μm-thick resist trace (□) in Figure 4-4.

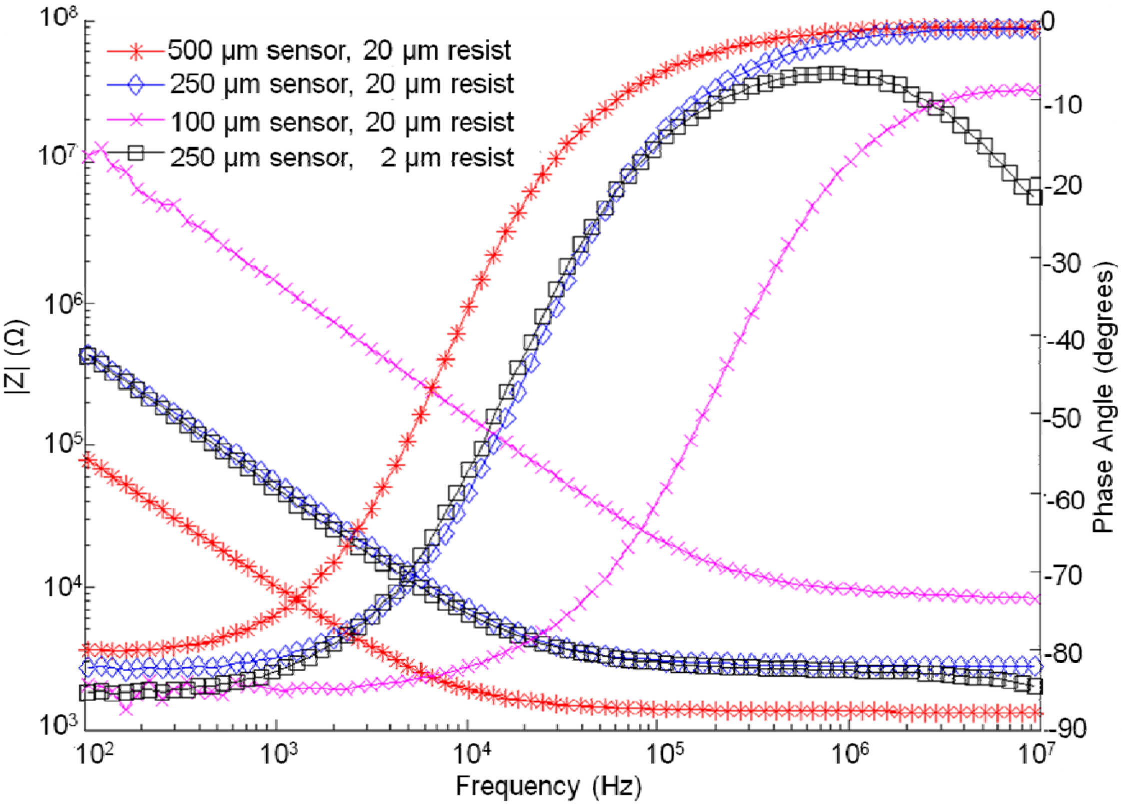

Figure 4-4: Bode plot of 500 µm trace-width devices, of varying sensor diameters, with 2 µm-thick resist and 20 µm-thick resist. * (500 µm sensor diameter, 20 µm thick resist); ◊ (250 µm sensor diameter, 2 µm thick resist); x (100 µm sensor diameter, 20 µm thick resist); □ (250 µm sensor diameter, 20 µm thick resist). Increasing the coating thickness to 20µm suppressed the coating

In contrast, the coating impedance of the devices with 20µm-thick coating is less than the spreading resistance for sensor diameters less than 250µm; so the coating capacitance component is not seen on the 250 µm (◊) and 500 µm (*) traces in Figure 4-4, however it is slightly apparent in the 100 µm sensor diameter, 20 µm thick resist trace (x). The results confirm that increasing the coating thickness to 20 µm eliminates the coating component for devices with sensor diameters of 250 µm or greater.

4.5 Effect of Decreasing the Coating Area

To study the effect of trace width, electrodes were designed and fabricated with 30 μm trace width and impedance was measured using KCl as the electrolyte. Decreasing the coating area from 1.1 mm^2 to 7.65x10^{-2} mm^2 eliminated the high-frequency coating component on all measured sensors, including the 500μm, 250μm, 125μm-diameter sensors, as illustrated in Figure 4-5.

The theoretical coating impedances (at 10 MHz) of the 30 μm trace-width devices averaged 9.6 x 10^3 Ω, a value greater than the spreading resistances of the 500μm diameter sensor (R_{sp} = 1.4 x 10^3 Ω), 250μm diameter sensor (R_{sp} = 2.8 x 10^3 Ω) and 125μm-diameter sensor (R_{sp} = 5.6 x 10^3 Ω). This demonstrates that theoretically as well as experimentally, the coating component is no longer dominant at high frequencies on the 30 μm trace-width devices.

By removing the high-frequency coating component, the equivalent circuit of the KCl-electrode system was simplified to a resistor-constant phase element (CPE) series circuit. The simplified R-CPE series circuit was used to fit the data and the extracted system parameters. The percent error of each fitted parameter was no greater than 3.5%, indicating a good fit with the R-CPE series circuit. This demonstrates that the coating capacitance component was successfully eliminated up to 10 MHz.

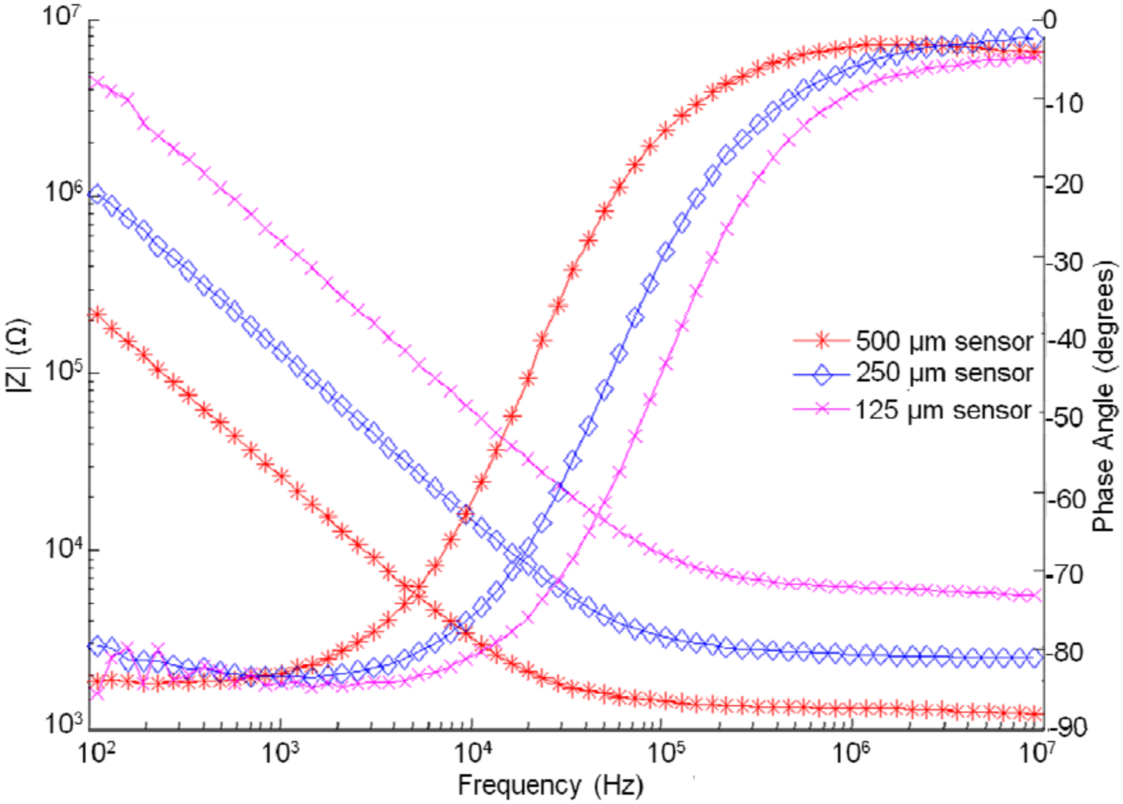

Figure 4-5: Bode plot of 30 µm trace-width devices with 2 µm-thick coating of varying sensor diameters. * (500 µm sensor); ◊ (250 µm sensor), x (125 µm sensor). Decreasing the coating area suppressed the coating impedance contribution.

4.6 Design Rule

The coating area is defined as the area of the polymer-covered lead trace in contact with the electrolyte (within the cylinder). The coating area was calculated with the following assumptions: (1) the arc formed by the cylinder across the traces was assumed linear and (2) the majority of the current flowed directly between the two traces.

Table 4-1 shows the calculated ratios of coating area to coating thickness for the 500 and 30 µm trace-width devices. The enclosed ratios are for those electrode configurations in which a coating capacitance component was not present in impedance measurements up to 10 MHz.

From the data in Table 4-1, the following inequality is derived:

$$\frac{coating\ area}{coating\ thickness} < 5.5 \qquad \text{Equation 4-2}$$

This signifies that if the ratio of coating area to coating thickness is less than 5.5, then a coating capacitance will not be present in impedance measurements up to 10 MHz.

Table 4-1: Ratio of coating area to coating thickness of 500µm and 30µm trace-width devices of varying sensor diameters. The coating capacitance component was not present in designs with enclosed ratio

	Coating area (mm^2)	RATIO 2µm-thick coating	RATIO 20µm-thick coating
500µm trace-width devices			
500µm sensor	8.07×10^{-1}	40.37	4.04
250µm sensor	1.10	55.09	5.51
100µm sensor	1.18	59.21	5.92
30µm trace-width devices			
500µm sensor	6.90×10^{-2}	3.45	
250µm sensor	7.65×10^{-2}	3.83	
125µm sensor	8.03×10^{-2}	4.01	

A coating capacitance component was not seen in the 500-, 250-, and 125µm –diameter sensors of the 30µm trace-width devices. The coating area to coating thickness ratio for all sensor diameters fell below the critical value of 5.5, previously derived; thus verifying the design rule.

4.7 Design Rule Applied to ECIS Commercial Devices

The commercial 8W1E ECIS (Applied BioPhysics) cell culture impedance device has a coated area of approximately 14 mm^2. For a coating thickness of 2 μm, the coating area to coating thickness ratio is calculated to be approximately 700, which is much greater than the critical ratio of 5.5. From this calculation, it can be inferred that the 8W1E ECIS device has a coating capacitance component at high frequencies. This was verified with previous measurements [75].

It has been experimentally proven that microelectrode devices, particularly those used for ECIS measurements, can be optimized by decreasing the coating (trace) area and/or increasing the coating thickness to eliminate the high-frequency coating component. A relationship between coating area and coating thickness was derived to aid in the design of ECIS-based microelectrode devices for high-frequency impedance measurements. A critical ratio of 5.5 (coating area to coating thickness) was defined in order to completely eliminate the coating capacitance component. The redesigned system reduces measurement artifacts and improves the quality of data across the beta-dispersion region. The new design will enable the use of the commonly used ECIS technique to measure real-time cellular properties in high frequency ranges (beta dispersion) that was not possible thus far.

Chapter 5 Comparison of Measurement Sensitivity Between 2- and 4-Electrode Configurations

5.1 Introduction

This work was performed in collaboration with the Naval Research Laboratory's Center for Biomolecular Science and Engineering. The effects of diffusion between non-conductive sheath and conductive sample fluids in an impedance-based biosensor were investigated using 2- and 4- electrode impedance configurations. Sections of this work, namely the surface chemistry, *E. coli* culture, and confocal microscopy, were performed by co-authors of this work published in [http://dx.doi.org/10.1039/C005257D] – Reproduced by permission of The Royal Society of Chemistry.

Hydrodynamic focusing addresses the problem of clogged channels by using laminar flow streams to provide virtual channels with flexible interfaces that can be much smaller than the physical dimensions of the solid channel. Biosensors employing hydrodynamic focusing have been reported for cell or particle detection [76], cytometry [77, 78], sorting [79] and mixing applications [80, 81]. Most incorporate optical analysis, usually fluorescence, for increased sensitivity and specificity. However, such systems include bulky optical components which are not easily integrated into lab-on-a-chip systems [82]. An alternative is to achieve target detection of species with techniques based on measurement of electrical signal, especially impedance.

Impedance measurements have been made with 4- and 2-electrode configurations, with each configuration providing unique information about the cell-electrode-electrolyte system. In 2-electrode measurements, current is passed between the same pair of electrodes as is used for the voltage measurement. Two-electrode measurements are very sensitive to changes at the electrode interface, but the formation of electrical double layer and other parasitic capacitances means that low frequency measurements are difficult with this setup [83-85]. In a 4-electrode system an oscillating signal is applied between the two outer electrodes and the impedance is measured across the two inner electrodes. Physical separation of the current and sensing electrodes in the 4-electrode configuration results in reduced parasitic double layer impedance, especially at lower frequencies [86]. Most impedance based biosensors in the literature use the 2-electrode configuration and only a few 4-electrode based systems have been reported [86-88].

A simple flow-focusing design is utilized, in which one sheath stream is used to focus a sample stream. By increasing the sheath-to-sample flow-rate ratio (FRR), the sample stream was focused along the sensing surface. Sensing was achieved using 2- and 4-electrode configurations, with an applied 10mV signal (1 kHz frequency). By choosing the sheath fluid to be non-conductive (deionized water) and the sample a conducting fluid (phosphate buffer saline or PBS), the injected current was confined to the focused stream.

5.2 Theory

The system involving sensing electrodes and bulk media can be represented with an equivalent circuit shown in Figure 5-1. R_b and C_b are the bulk resistance and capacitance of the conductive medium and C_{dl} represents the double layer capacitance at the sensing electrodes [89].

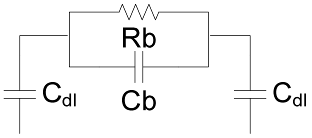

Figure 5-1: Equivalent circuit of electrode-electrolyte (medium) system; where Rb and Cb are the bulk resistance and capacitance of the conductive medium and Cdl represents the double layer capacitance at the sensing electrodes.

The main advantage of the 4-electrode setup is that the double layer capacitance at the current electrodes does not play a part since the current and sense electrodes are physically separated and therefore it can be ignored. The equivalent impedance (Z_{eq}) consists of the R_b in parallel with C_b (Figure 5-2).

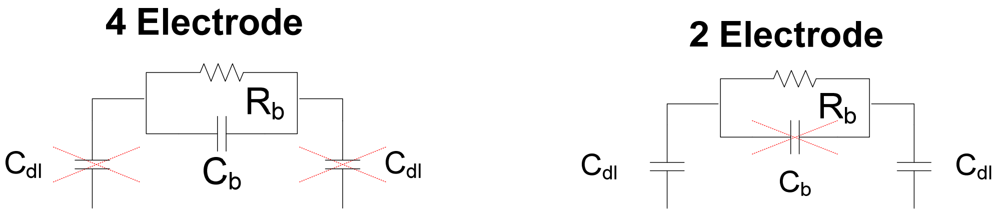

Figure 5-2: Modified equivalent circuits for 4- and 2-electrode measurement configurations.

The LCR meter measures the real R_M and imaginary X_M components of the equivalent circuit impedance, Z_{eq},

$$Z_{eq}= R_M+ jX_M \qquad \text{Equation 5-1}$$

Parallel combination of the bulk resistor and capacitor results in the following relationships, relating the bulk counterparts to the real and imaginary components.

$$R_M = \frac{R_b}{1+\omega^2 R_b^2 C_b^2}$$ Equation 5-2

$$X_M = \frac{-\omega R_b^2 C_b}{1+\omega^2 R_b^2 C_b^2}$$ Equation 5-3

The two equations can be solved to find the desired R_b and C_b values, using

$$R_b = \frac{R_M^2 + X_M^2}{R_M}$$ Equation 5-4

$$C_b = \frac{-X_M}{\omega\left(R_M^2 + X_M^2\right)}$$ Equation 5-5

In the 2-electrode system the current and sense electrodes are the same and therefore double layer capacitance cannot be ignored, especially at the low signal frequencies used in this study (1 kHz). In the simplest approximation, C_b is generally negligible as compared to C_{dl} and may be ignored. The equivalent circuit, as shown in Figure 5-2, thus includes R_b in series with C_{dl} (at each electrode). The resistance and capacitance measured by the LCR in this case are related to the circuit elements through

$$R_b = R_M$$ Equation 5-6

$$C_{dl} = \frac{-1}{\omega X_M}$$ Equation 5-7

5.2.1 Interfacial Impedance

The gold electrodes in this system are considered completely polarizable and thus pass no faradaic current. In addition, impedance measurements are performed with a small AC signal applied at equilibrium; thus the response is linear, and no charge-transfer reactions occur within the electrochemical system. When the electrodes are in contact with the liquid electrolyte,, the electrodes attract ions and form a double layer across the electrode/electrolyte interface with a thickness on the order of angstroms. The double layer consists of a layer of ions that are specifically adsorbed to the surface of the electrodes and a diffuse layer, in which ions are dispersed perpendicularly away from the electrode surface due to thermal motion. The thickness of the diffuse layer increases in more dilute solutions. Since the adsorbed (ads) and diffuse (diff) layers are in series, the equivalent double layer (dl) capacitance can be described by the following equation

$$\frac{1}{C_{dl}} = \frac{1}{C_{ads}} + \frac{1}{C_{diff}} \qquad \text{Equation 5-8}$$

At sufficiently high conductivities of electrolytes the thickness of the diffuse layer decreases (C_{diff} increases) [90] and

$$C_{dl} \approx C_{ads} \approx \frac{\varepsilon_o \varepsilon_r A}{d} \qquad \text{Equation 5-9}$$

The typical values are in the range of 10 to 40 μF/cm^2 [89, 91]. In 2-electrode configurations, in the absence of any Faradaic processes, the equivalent impedance is thus described by the series combination of double layer capacitance and solution (bulk) resistance.

The corresponding double layer impedance Z_{dl} is inversely proportional to capacitance as described by

$$Z_{dl} = \frac{1}{j\omega C_{dl}} \qquad \text{Equation 5-10}$$

where j is the standard imaginary unit with the property $j^2 = -1$ and ω is angular frequency. Thus as the electrode area increases, the double layer capacitance increases and in turn the impedance decreases. For 4-electrode configurations, the contribution of the double layer capacitance is negligible and equivalent impedance is found by a parallel combination of bulk resistance and capacitance.

5.2.2 Bulk Impedance

Bulk resistance for coplanar electrodes is given by

$$R_{bulk} = \rho\kappa \qquad \text{Equation 5-11}$$

where ρ is the measured resistivity of the focused stream, κ is geometric factor called the cell constant. This equation holds for the 2- and 4-electrode systems although the expression for cell constant is different in each case.

The bulk capacitance of the 4-electrode system is inversely proportional to its cell constant. The cell constant of the 4-electrode configuration can be estimated using a point-electrode model shown in Figure 5-3. The model consists of four electrodes that are located on the surface of the glass slide. The electrodes are in contact with the focused sample stream of thickness z which is sandwiched by the sheath stream from the top. The resistivity of glass ρ_{Glass} is assumed to be infinite for the purpose of this model.

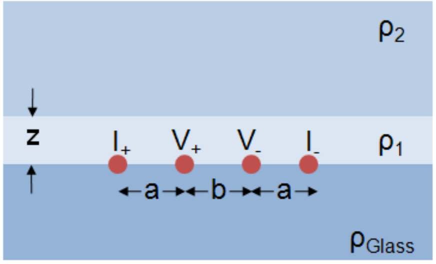

Figure 5-3: A point-electrode model for the tetrapolar configuration where the current is injected in the outer two electrodes and voltage is sensed from the inner two. The distance between current and sense electrodes is a and between sense electrodes is b. The conductive focused stream with resistivity ρ1 has a height x. The non-conductive sheath with resistivity ρ2 extends infinitely above the focused stream in this model.

Using the imaging method the cell constant can be approximated to the first order by

$$\kappa_{4pt} = \frac{1}{\pi}\left[\frac{b}{a(a+b)} + 2\Gamma\left(\frac{1}{\sqrt{a^2+4z^2}} - \frac{1}{\sqrt{(a+b)^2+4z^2}}\right)\right] \qquad \text{Equation 5-12}$$

where *a* is the distance between current and sense electrodes and *b* is the distance between sense electrodes [92]. The interface between the high conductivity focused stream and low conductivity sheath stream is seen as a semi-transparent mirror having a reflection coefficient Γ defined as

$$\Gamma = \frac{\rho_2-\rho_1}{\rho_2+\rho_1} \qquad \text{Equation 5-13}$$

where ρ_1 and ρ_2 are the resistivities of sample and sheath fluids respectively [93]. In an aqueous solution, there is also a capacitive pathway for the current, which can be modeled as a capacitor in parallel with the resistance of the sample.

The bulk capacitance is given by

$$C_{bulk} = \frac{\varepsilon_o \varepsilon_r}{\kappa_{4pt}} \qquad \text{Equation 5-14}$$

where ε_0 is the permittivity of vacuum and ε_r is the relative permittivity of the conductive PBS [94]. The permittivity of ionic solutions is inversely proportional to conductivity and approaches the permittivity of water (~78) as the conductivity decreases [95, 96]. For the frequency range of 1k Hz used in our data, the permittivity can be assumed to be constant [95]. From Equations 5-11 and 5-12 it can be seen that as the thickness of the focused stream decreases, the resistance increases while Equation 5-14 suggests that bulk capacitance decreases as the focused layer thickness decreases. The cell constant for a 2-electrode model has been found using conformal mapping techniques elsewhere [94, 97].

5.3 Methods and Fabrication

5.3.1 Electrode Fabrication

Standard photolithography techniques were used to fabricate the electrodes. Borosilicate glass microscope slides (Daigger, Vernon Hills, IL) were used as the substrate. The slides were thoroughly cleaned to allow good adhesion of electrodes to the glass surface. The slides were initially cleaned with HCl:MeOH 1:1 v:v for 30 minutes and then rinsed with water. This was followed by immersion in H_2SO_4 for 30 minutes and then rinsing in water. Finally, the slides were placed in 100°C water for 10 minutes and dried with nitrogen.

Clean slides were dehydrated on a 150°C plate for 5 minute and subjected to O_2 plasma for 4 minutes just before the photolithography step. A 1μm thick layer of negative photoresist (NR7 1000PY-Futurex, Franklin, NJ) was patterned using a transparency mask (Pageworks, Boston, MA). An electron beam evaporator was used to deposit a film of gold (300 nm) onto the slides with a thin film of titanium (30 nm) as the adhesion layer. The electrodes were defined by photoresist lift-off in acetone. The current electrodes were 1000 μm wide while the widths of the sense electrodes and the inter-electrode distances were both 500 μm. A schematic of the electrode device is shown in Figure 5-4a.

5.3.2 Microchannel

The microchannel design used in this study had two inlets for the sheath and sample fluids and one outlet. The sheath inlet (0.5 x 1 mm^2) was oriented at 90° with respect to the sample and focusing channels. The sample channel had a smaller cross-section (0.15 x 0.3 mm^2) than the focusing channel (0.25 x 1 mm^2); the sheath fluid focused the sample from the sides as well as the top with this geometry. The length of the channel from the sample inlet to the outlet was 30 mm.

The devices were milled from polymethyl methacrylate (PMMA) (Plexiglas G, Atofina Chemical, Inc. Philadelphia, PA) using a HAAS Mini Mill (HAAS Automation, Inc., Oxnard, CA). The sheath inlet and the focusing channel were machined with a 0.254mm long-reach endmill, and a 0.787mm endmill respectively. The sample channel was machined with a 0.254mm endmill (Harvey Tool, Rowley, MA). A 0.5mm wide trench was milled around the microchannel and inlets using a 0.381mm endmill. This trench prevents the glue from running into the microchannel [98]. A bench top drill press was used to widen the upper half of the inlets and outlet where 0.58mm wide metal tubing was inserted and glued into place using 5-minute epoxy (Devcon, Danvers, MA).

The PMMA pieces with milled microchannels and metal tubing were glued to the microscope slides with prepared electrodes and antibodies using UV-curable adhesive (Optical adhesive #72, Norland Products, Cranbury, NJ). Figure 5-4b shows the representation of a fully assembled device.

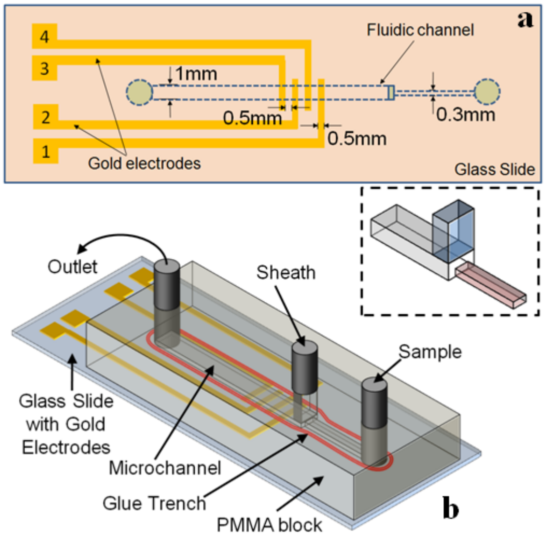

Figure 5-4: (a) A top-view schematic of the gold electrodes and microfluidic channel, along with their corresponding dimensions. Outer electrodes (1 and 3) supply current while the inner two (2 and 4) sense the signal. The width of the sensing electrodes as well as the spacing between them is 0.5 mm while the current electrodes are 1mm wide. The sample channel width is 0.3mm which increases to 1mm in the focusing channel. (b) Figure of an assembled microchannel and electrodes. The channel machined in PMMA is glued to the glass slide using a UV curable glue. The inset shows the channel junction where sheath and sample streams meet.

5.3.3 Immobilization Chemistry

The electrode patterned slides were cleaned with O_2 plasma for 2 minutes prior to protein immobilization. To immobilize the antibody directly onto the gold electrode, the procedure used by Chatrathi et al. was employed [99]. Briefly, 250 μg of goat anti-*E. coli* antibody (2 mg/ml in PBS, Fitzgerald Industries International, Concord, MA) was incubated with 40μl 20 mM sulfo-LC-SPDP(Pierce, Rockford, IL) for 60 minutes at room temperature with mixing. To the mixture, 150 mM DTT in acetate buffer pH 4.5 was added and incubated with mixing for 30 min. The entire mixture was then exposed to the gold electrodes for 60 minutes. The slides were rinsed with water, dried, and stored at 4°C until use.

5.3.4 E. coli Assay Preparation

The cells used for this study were *E. coli* rosetta and were cultured in LB broth with 1% glucose and 0.1% ampicillin. For the assays, 1.5 mL of cell culture was spun down in an Eppendorf tube at 3000 rpm for 5 min. The supernatant was removed and 1 mL 50 mM borate buffer pH 8.0 was added to the cells. A tube of Cy3 monoreactive succinimide ester (GE Health care, Piscataway, NJ) was dissolved in 50 μL DMSO. Fifteen microliters of the dye was added to the cell solution and the sample was incubated for 30 min at room temperature in the dark with shaking. The cells were respun and the supernatent was removed. The cells were washed 3 times with PBS pH 7.4 (Sigma Chemical, St Louis, MO) and stored in 1 ml PBS at 4°C until use. The cells were used within 24 hours. Cell concentrations were typically 10^9 cfu/ml.

5.3.5 Flow Simulations

Finite element modeling of the channels was performed using the COMSOL Multiphysics finite element analysis package (COMSOL Inc., Palo Alto CA). The channel dimensions in the model were chosen to be identical to the ones used in experiment. However, in order to reduce computation time, only half of the width of the channel was used in simulations, assuming channel symmetry.

Relative sample and sheath flow rates were varied to simulate changing cross-sectional area of the focused stream. The simulations were conducted in two steps. In the first step, the flow model was solved for incompressible flow. A zero-slip velocity boundary condition was assumed on the channel walls. The inlet boundary conditions were specified by the desired volumetric flow rate, and outlet boundary conditions were fixed at atmospheric pressure. Flow in the inlets was specified to be fully developed. After the velocity field was determined, the second step simulated mass transport to provide the concentration distribution, assuming a diffusion coefficient typical of a low molecular weight solute ($1x10^{-9}$ m^2/s). The presence of conducting ions in sample stream had an initial concentration of 1 in the diffusion/convection simulation. Similarly, the initial concentration of the sheath stream, which was devoid of ions, was chosen to be 0. An automesh with tetrahedral elements was used for all simulations. In order to accurately resolve the mass transport along the interface between the sheath and sample streams, adaptive meshing was used to increase mesh density in subsequent simulations. The mesh refinement process was repeated until no change in result was observed (h-method). It was assumed that there were no chemical reactions and the ionic nature of the sample does not affect the outcome of simulations; therefore the only factors affecting the distribution of the model species were diffusion and convection. The details of the multiphysics modules and the equations used to define flow and mass transport characteristics were previously [88].

5.3.6 Confocal Microscopy

Visualization of flow focusing in the channel was performed using a Nikon Eclipse TE2000-E inverted microscope equipped with a Nikon D-Eclipse C1si confocal spectral imaging system (Nikon, Japan). Confocal images were obtained by scanning in the region downstream from where the sheath and sample streams intersect. The hydrodynamic focusing experiments were performed using de-ionized water for the sheath flow and de-ionized water mixed with FWT Red Powder fluorescent dye (Bright Dyes, Miamisburg, OH) for visualization of the flow from sample stream inlet.

A dual syringe pump (Harvard Apparatus Model 33) provided precise control of the flow rates and flow-rate ratios. Confocal microscopy was performed using a 10X objective (NA 0.45, WD 4.00 Dry). Image resolution was 512 x 512 pixels, with a Z-step size spacing of 5 μm and a pixel dwell time of 7.06 μsec. A 40 mW Argon laser was used at the 514.5 nm excitation line, and the spectral detector of the confocal imaging system was set to detect emission between 583-593 nm. Image stacks were rendered and analyzed in three-dimensions using NIS-Elements AR confocal image processing software (Nikon, Japan).

5.3.7 Electrical Impedance Measurements

An Agilent 4284A LCR meter was used to perform all 2- and 4-electrode impedance measurements using a 10 mV, 1 kHz signal. For the 2-electrode system, the current was applied and the response was measured from the inner two electrodes. Baseline measurements were performed after bovine serum albumin (BSA) was passed through the channel to prevent nonspecific binding. Phosphate buffer solution (PBS) with a conductivity of 12.8 mS/cm was used as the sample fluid, and deionized (DI) water with a conductivity of 0.08 mS/cm was used as the sheath fluid. Impedance data was collected at different sheath-to-sample flow-rate ratios (FRRs) and flow velocities. In order to increase the focusing, the FRR was increased by increasing the sheath flow rate while the sample flow rate remained constant at 2 μL/min. In other cases, flow rates of both sheath and sample were increased proportionally to maintain a FRR of 50. A Labview program was developed to control the syringe pump and automate data collection from the LCR meter. After the baseline measurements were completed, *E. coli* was passed through the channel and allowed to settle and bind for 20 minutes to the immobilized antibodies. Unbound bacteria were flushed out of the channel, and impedance measurements were conducted. Both baseline and *E. coli* measurements were repeated three times. Resistance and reactance values were extracted from the measured impedance data.

5.4 Results and Discussion

5.4.1 COMSOL Simulations and Confocal Microscopy

Figure 5-5 illustrates transverse slices of the COMSOL simulations of a microfluidic channel for FRRs of 25 and 100. Since only half of the channel was simulated, the cross-sections were mirrored and stitched to allow easier comparison with confocal images. All cross-sections were taken 3mm downstream from sheath inlet. The electrodes are positioned at the bottom surface along the length of the channel. The concentration value of 0 of the nonconductive sheath fluid is shown as blue and the concentration value of 1 of the conductive sample fluid is shown as red. The intermediate colors signify the diffusion between the two streams. Figure 5-5 shows confocal microscopy images of an actual channel with a 0.25 mm height and 1 mm width. The decrease in image brightness in confocal images is attributed to the diffusion between the sheath and sample fluids.

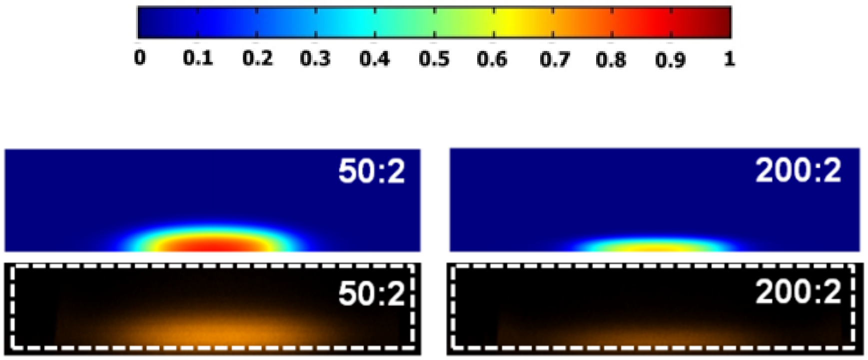

Figure 5-5: COMSOL simulations (top) and the corresponding cross-section images from confocal microscopy (bottom) with sheath-to-sample flow-rates of 50:2 and 200:2 (in µL/min). The same channel was used for the confocal experiment in both cases. The outline shows the boundary of the channel. The diffusion co-efficient for the simulations was 10^9 m^2/s. The concentration is specified by the color bar with 0 (blue) as the minimum and 1 (red) as the maximum. The intermediate colors show diffusion region between the sheath and sample streams. The confocal cross-sections were taken 3mm downstream from the junction where sheath and sample streams met.

The channel cross-sections from simulations and confocal demonstrate how the sheath fluid focused the sample stream from both sides and the top, resulting in a half ellipse-shaped focused stream. Furthermore, both modes of investigation show that an increase in FRR resulted in greater flow focusing toward the electrode surface. The degree of focusing at a specified FRR was roughly the same for both simulations and confocal experiments. The width of the focused stream remained fairly constant due to the geometry of the channel but the change in the height was significant. Thus the effective cross-section of the sample fluid was significantly reduced without minimizing the physical dimensions of the channel.

As the FRR became higher, the sample stream was focused more and thus pushed closer to the bottom channel wall. The focused layer heights for FRR of 25 and 100 were roughly 64µm and 30µm respectively. The velocity profiles for the flow in the focusing channel are parabolic. Although the fluid was flowing faster and the residence time was smaller when FRR was 100, the characteristic length over which the diffusion took place was also more significant as compared to focused layer height. The higher FRR resulted in a smaller cross-sectional stream with lower overall concentration of sample electrolyte. In confocal images, this lowering of sample concentration manifested as a reduction in brightness of the focused region for 200:2 µL/min as compared to 50:2 µL/min and was also accurately predicted by the simulations (Figure 5-5).

Diffusion in parallel laminar flow streams inside microchannels has been studied previously [100-102] and has also been used for biosensing applications [103, 104]. However, for impedance sensors that rely on flow-focusing for enhancement of detection sensitivity, this diffusion has deleterious effects. The electric field confinement relies on a sharp gradient between the conducting sample and non-conducting sheath streams. Therefore, any mixing due to transverse diffusion between sheath and sample fluids reduces the confinement of the electric field. The overall effect is a loss in detection sensitivity.

5.4.2 Baseline and E. coli Measurements

Baseline and *E. coli* measurements were performed using 2- and 4-electrode configurations at different FRRs (25, 50, and 100). The resistance and reactance components of the impedance were measured using the LCR meter, and resistance and capacitance values were extracted assuming parallel RC circuit for the 4-electrode case and series RC circuit for the 2-electrode case.

Table 5-1 and Table 5-2 list mean values and standard deviations of three repeated impedance measurements using the 2- and 4-electrode configurations.

Table 5-1: Baseline and E. coli resistance and capacitance values for the 2-electrode configuration sensor

FRR	Bulk Resistance (kΩ), R			Interfacial Capacitance (nF), C		
	Baseline	*E. coli*	%Δ	Baseline	*E. coli*	%Δ
50:2	33.1 ± 0.6	37.5 ± 0.3	13.5%	16.2 ± 1.0	14.0 ± 1.0	-13.9%
100:2	52.9 ± 0.8	58.8 ± 0.5	11.2%	12.4 ± 0.1	11.1 ± 0.1	-10.2%
200:2	79.3 ± 0.7	85.6 ± 2.2	8.0%	9.2 ± 0.1	9.0 ± 0.2	-2.3%

Table 5-2: Baseline and E. coli resistance and capacitance values for the 4-electrode configuration sensor

FRR	Bulk Resistance (kΩ), R			Bulk Capacitance (nF), C		
	Baseline	*E. coli*	%Δ	Baseline	*E. coli*	%Δ
50:2	31.5 ± 0.7	38.1 ± 1.0	20.8%	1.36 ± 0.02	1.31 ± 0.02	-3.7%
100:2	53.0 ± 0.5	61.2 ± 0.2	15.6%	1.29 ± 0.01	1.26 ± 0.01	-2.3%
200:2	78.6 ± 1.3	90.3 ± 0.9	14.8%	1.20 ± 0.01	1.18 ± 0.01	-1.7%

The percent change in resistance and capacitance due to the presence of *E.coli* was calculated using

$$\%\Delta = \left(\frac{E.coli - Baseline}{Baseline}\right) x\ 100 \qquad \text{Equation 5-15}$$

For both the 2- and 4- electrode baseline measurements, as the sample fluid became more focused at higher FRRs, the measured resistance values increased. This is expected since the cross-sectional area of the focused stream decreases thus causing an increase in resistance. In addition, resistivity also depends on the number and types of ions in solution, as was experimentally demonstrated by Larsen, et al. [105]. Therefore, the diffusion between the sample and sheath fluids contributed to a further increase in resistance.

For the 2-electrode baseline measurements, the reduction in interfacial capacitance with increased FRR was mostly due to the decrease in the width of the focused stream which effectively decreased the electrode area as described by Equation 5-8. In the 4-electrode system, the slight decrease in the bulk capacitance was attributed to an increase in cell constant (Equation 5-14). As seen from Equation 5-12, the cell constant is inversely proportional to the focused layer height, which decreased with increasing FRR.

The resistance and capacitance values with immobilized *E. coli* followed the same trend as the baseline measurements. The presence of *E. coli* caused an increase in the resistance and a decrease in capacitance in both configurations. Bacteria and other cells act as insulators due to the impermeability of cell membrane at low frequencies [106]. The increase in resistance demonstrated that the *E. coli* were insulating and partially blocking the current paths on the electrodes, and thus contributed an additional impedance component to the system. The presence of insulting bacteria resulted in a decrease in capacitance which was due to a decrease in the effective electrode area as per Equation 5-8. The two-electrode system was more sensitive to changes at the electrode surface, as is highlighted by a greater change in capacitance due to the presence of the *E. coli* cells on the electrodes.

Interestingly, when the FRR was increased, the percent change in resistance and capacitance decreased. This effect is attributed to the diffusion of ions from the conducting stream into the non-conducting sheath fluid. As shown earlier, the amount of diffusion was roughly the same, but the characteristic length over which the diffusion occurred became more significant as the cross-sectional area of the focused stream decreased. This increased the bulk resistance and competed with the insulating effect of the *E. coli.* The overall effect was a decrease in percent change in resistance as FRR increased. From Equations 5-11 and 5-14, it can be seen that an increase in resistivity also caused an increase in the capacitance which counteracted the decrease in capacitance due to presence of cells on the electrodes. Overall, the percent change in capacitance decreased slightly as FRR was increased. Thus as the sample fluid became more focused, the diffusion had more impact on the measured data (also seen in Figure 5-5).

The amount of diffusion between the sheath and sample is dictated by the residence time or the time sheath and sample streams are in contact with each other and the distance over which transverse diffusion takes place. As the FRR increased, fluid flowed faster in the channel and decreased the residence time and, therefore, the diffusion of the ions out of the sample fluid. At the same time, increasing the FRR pushed the focused stream closer to the channel wall decreasing the mean distance of an ion to the sample-sheath interface.

In order to delineate these two phenomena, confocal microscopy, simulations and impedance measurements were performed for cases with same FRR but with increasing sheath and sample flow velocities. As the fluid flowed faster, the residence time decreased and resulted in less diffusion within a fixed distance. Figure 5-6 shows confocal images of sample only, and sheath-to-sample flow rates of 50:1, 100:2 and 200:4 μL/min. All three cases have FRR equal to 50; however, the sheath and sample fluids of the 200:4 ratio were flowing 4-times faster (13.6 mm/s).

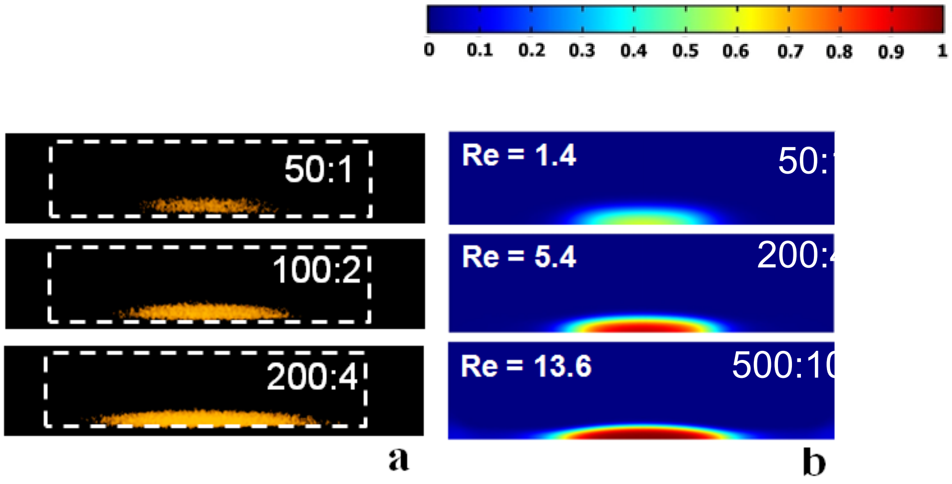

Figure 5-6: (a) Confocal images for sheath-to-sample flow rates (in μL/min) of 50:1, 100:2 and 200:4 (FRR = 50) are shown. The contrast was adjusted by same measure for all cross-sections to allow easier visualization of focused stream. (b) Channel cross-sections show concentration distributions from COMSOL simulations. Flow velocities of both sheath and sample streams were increased proportionally to maintain the FRR at 50. The diffusion coefficient was 1 x10-9 m2/s for all cases. The concentrations are specified by the color bar with 0 (blue) as the minimum and 1 (red) as the maximum.

Both confocal images and simulations show that there was relatively little change in focused stream height since the FRR was unchanged. The results also showed that more diffusion occurred when the fluids were flowing slower, as signified by the loss in brightness of the focused region at slower flow velocities. COMSOL simulation results further confirmed this finding. Based on the results shown in Figure 5-5 and Figure 5-6, it is clear that in order to improve the detection sensitivity, without introducing the deleterious effects of diffusion, both the FRR and absolute flow velocities must be increased simultaneously.

At the highest flow velocities, 200:4 µL/min and 500:10 µL/min in Figure 5-6, as the *Re* increased, the sheath stream lost its ability to focus the sample stream from the sides and this resulted in widening of the focused stream along the bottom surface of the channel wall. A further increase in the flow velocities led to the splitting of the sample stream into two focused streams. The optimal condition for this design to provide maximum focusing but with the least effect of diffusion appears to be for sheath-to-sample flow rates of 100:2 µL/min (FRR = 50, Re = 2.7). The diffusion between sheath and sample fluid can also be reduced by using ionic species with slower diffusion coefficients or by using fluids that are immiscible i.e. two-phase. However, two-phase parallel flows are only possible in narrow FRR regime and more generally result in droplet formation [107].

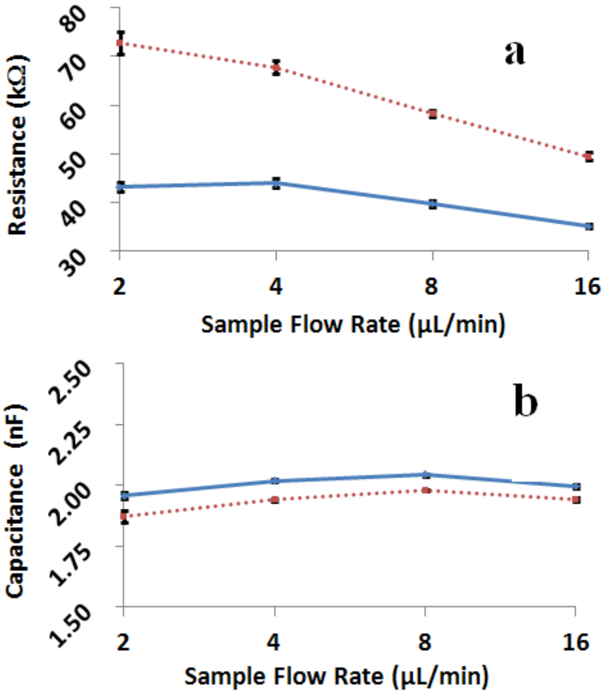

Figure 5-7: Sample and sheath flow rates were increased while keeping the FRRs constant (--■-- = FRR of 50, —♦— = FRR of 25). Sheath flow rates are: *FRR x Sample flow rate*. A 4-electrode configuration was used to measure (a) resistance and (b) capacitance.

Impedance measurements were performed at FRRs of 25 and 50 using the 4-electrode configuration. The sample flow rates were set to 2, 4, 8, and 16 µL/min, and the sheath flow rates were increased accordingly to obtain the corresponding FRR. The plot in Figure 5-7 shows that the resistance decreased as flow velocities increased due to a decrease in diffusion. The values of capacitance were largely unaffected.

5.5 Conclusions

A two-dimensional (2D) flow focusing technique was implemented for a modified T-junction design. Two- and four-electrode configurations for impedance measurements were characterized for detection sensitivity. Measuring a change in resistance using the 4-electrode configuration was the most sensitive technique to detect the presence of *E. coli* at low frequencies in a flow focusing system. The 2-electrode technique showed a greater percent change in capacitance than the 4-electrode sensor because the cells were bound to the electrode surface and the 2-electrode configuration is more sensitive to changes at the electrode interface. The fact that the percent change in impedance decreased with increasing FRRs indicated that the presence of the bacteria became less significant with increased focusing, even though they represented a higher proportion of the cross-sectional area of the conducting stream. This effect was attributed to the increased effect of the diffusion of ions out of the focused stream as the focused stream height decreased. One way to reduce diffusion was to increase the actual sheath and sample flow velocities in addition to increasing the FRR. Diffusion must be properly controlled in order to prevent a loss in detection sensitivity using flow focusing and impedance measurements.

Chapter 6 Multi-Device, Multi-Electrode Bio-Impedance System

6.1 Introduction

Impedance spectroscopy (or bio-impedance) offers a non-destructive, non-invasive, label-free technique to continuously monitor and quantitatively characterize biological cells. This technique, applied to adherent cells, is also referred to as electric cell-substrate impedance sensing (ECIS). Researchers Giaever and Keese pioneered the design and development of the ECIS technique and system [108]. In this technique, a small AC signal is applied, and the resulting voltage or current is measured across a pair of electrodes. The impedance of the system is calculated to obtain frequency-dependent data of the electrode-cell system. When cells attach and spread onto the electrodes, their insulating membranes cause an in increase in impedance. Strikingly, changes in cell morphology, viability, death, and micromotion can be detected with high sensitivity, even prior to changes observed microscopically [2, 8].

The majority of electrode designs for the ECIS system and similar impedance-based microelectrode devices contain (1) a single electrode [4, 74], (2) parallel (connected) electrodes [17, 56], or (3) interdigitated electrodes (IDEs) [109, 110]. The IDEs and parallel electrodes cover more surface area and measure a greater quantity of cells thus resulting in an averaging of the changes across the cell culture. On contrast, the single electrode design typically only covers a very small percentage of the cell culture area and thus, does not provide encompassing data of the cell culture in its entirety. Therefore, a major challenge in ECIS is the collection of statistically-significant data from single culture wells. A solution to this problem is via incorporation of independent electrodes within a cell culture to enhance the spatial resolution and statistical analyses of impedance measurements.

Few designs have implemented multiple independent electrode measurements within a cell culture. Wegener et al. [111], for example, designed a device with a row of 4 independent working electrodes (2 mm-diameter) to conduct trans-epithelial and trans-endothelial electrical resistance (TER) measurements of cell cultures. Their multi-electrode design allows one to measure local inhomogeneities within the cell culture [111]. Similarly, Arndt et al. [9], developed a device with 3-independent electrodes (4 mm-diameter) on a microscope slide. In both studies, quantitative analyses and comparisons of the individual electrodes were not demonstrated. Additionally, the large sensing (working) electrodes result in a greater averaging effect than if microelectrodes were used.

Giaever and Keese have developed the ECIS technique into a commercial system (available through Applied Biophysics) that allows real-time impedance measurements inside a humidified incubator. A variety of electrode designs are offered, including single electrode devices, IDEs, and a device with 2 independent working electrodes (250 μm) within a cell culture chamber. While it is a well-known and widely accepted technique [2, 5, 6, 8, 9, 11, 14, 17, 112], its shortcomings include limited frequency range, limited number of acquired data points, and minimal spatial resolution. In the commercial ECIS system, the high end of the frequency range is limited by the presence of the passivation layer over the unexposed gold traces. This coating results in a parasitic capacitance at higher frequencies, where current preferentially travels through the least resistive pathway [53].

Our approach to enhance spatial resolution and statistically significant data acquisition is to increase the number of independent working electrodes to obtain redundant impedance datasets within the same cell culture chamber. Herein, we present an evaluation of a cell culture chamber with eight independent sensing electrodes to improve statistical significance of measured data and obtain position-dependent data across the cell culture. A switching circuit was designed to control four separate wells to simultaneously evaluate multiple cell cultures and variables. One challenge in implementing a multi-device, multi-electrode system is analyzing the large datasets, especially frequency-dependent data. A Matlab program was designed to automate data analysis and model the data with corresponding (cell or cell-free) equivalent circuit models. The system was evaluated by investigating the effects of a cytotoxic agent, arsenic trioxide (As_2O_3), on the well-established ovarian carcinoma cell line.

6.2 Methods and Materials

6.2.1 Cell Culture

HEY ovarian carcinoma cells were kindly provided by Dr. Gordon Mills (MD Anderson Cancer Centre, Houston, Texas). The cell line was cultured in RPMI 1640, supplemented with 8% FBS and penicillin/streptomycin. The cells were maintained in a humidified incubator containing 95% air and 5% CO_2 at 37^0C. For all experiments, cells were detached from flasks with trypsin-EDTA solution and seeded into the electrode devices at a concentration of 500,000 cells/mL prior to any treatment with drugs. Arsenic trioxide (As_2O_3) was obtained from Sigma-Aldrich. Cells were treated with varying doses of As_2O_3 (0-50µM).

6.2.2 Fabrication of 8-Electrode Arrays

Four-inch glass wafers were solvent cleaned (acetone and methanol) and dried with nitrogen. The first photolithography process, with NR1-3000PY (Futurrex) negative photoresist, was performed to define patterns in the resist in the shape of the electrode device. Chromium (150 Ǻ) and gold (350 Ǻ) were deposited onto the wafers using an e-beam evaporator. Subsequently, a lift-off was performed with acetone to remove the resist and the metal on it, leaving metal only on the defined areas of the wafer. The wafers were descummed in oxygen plasma to remove any resist residue. Next, the wafers were solvent cleaned and dehydrated, in preparation for the second lithography step. This lithography step is performed to passivate the traces with SU8-5 and define the working electrodes. The lithography ensured that the 250μm-diameter working electrodes (sensors), counter electrode, and contact pads are exposed. The wafers were descummed in oxygen plasma at 50 Watts for 2 minutes to remove any resist residue and to activate the plasma to enhance biocompatibility [113]. The wafers were then hard baked then diced into individual devices, 20 mm x 21 mm. Cloning cylinders (10 mm-diameter) were attached to define the culture well around the electrodes. SU8-5 was also used to attach the cylinders and form a tight seal. The devices, with secured cylinders, were cleaned with IPA and descummed in oxygen plasma to remove any debris. Lastly, the devices were autoclaved for five minutes to sterilize the devices in preparation for cell culture. Figure 6-1(a) shows a photograph of the fabricated device.

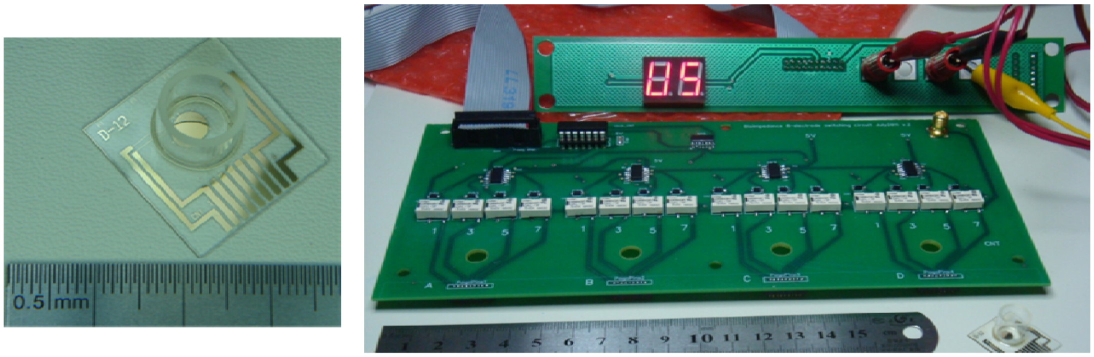

(a) (b)

Figure 6-1: Photographs of (a) fabricated electrode device with attached cloning cylinder and (b) power board and switching circuit before being enclosed in aluminum box.

6.2.3 Switch Circuit

A switching circuit (Figure 6-1(b)) was designed to rapidly and continuously measure four separate electrode devices containing eight independent working electrodes. The circuit was controlled by a Microchip PIC16F688 microcontroller that controlled five shift registers (Fairchild Semiconductor, 74VHC164), which in turn actuated 36 SPST (Omron, G6L-1F) relays. Thirty-two relays were used to control each working electrode (8x4) and the remaining four relays controlled the counter electrode of each device. The relays were connected to four separate nine-pin pogo pin headers (Mill-Max), which served as the interface between the switching circuit and the contact pads of the electrode devices. An SMA connector/cable was used to transmit the working and counter electrode signals to and from the Agilent 4294A impedance analyzer. After the circuit board was populated, it was covered with an acrylic conformal coating (Techspray, 2108-12S) to protect it from the humidity within the incubator; and finally it was mounted inside of an aluminum box. A separate PCB board, connecting the power supply, ground, and trigger, was positioned outside of the incubator and connected to the switching circuit via a ribbon cable. The outside power board also contained a two-digit LED display to indicate the active electrode being measured.

6.2.4 Impedance Measurements

Impedance measurements were performed with an Agilent 4294A impedance analyzer across a frequency range of 500 Hz to 100 kHz at 5 mV. System parameters including solution resistance, double layer capacitance, cell resistance, and cell membrane capacitance were extracted using equivalent circuit modeling and CNLS fitting algorithm.

6.3 Impedance Theory

Measurements of cells (bio-impedance measurements) are performed with a small AC signal (< 25 mV) across a variety of frequencies ranges. The use of small applied signals allows (1) non-invasive and non-destructive measurements of biological cells/tissues and (2) confinement of measurements within a pseudo-linear region. Typically a constant voltage (<25 mV) or current (~1 μA) is applied across the electrodes, and the resulting current or voltage is measured. Impedance is calculated according to Ohm's Law: $V = IZ$.

Equivalent circuit modeling was used to extract system information and required multi-frequency data points to extract system parameters. When adherent cells are present, at lower frequencies, characteristics of the electrode interface (double layer capacitance) are prominent; at mid-frequencies, cellular characteristics are dominant; and at higher frequencies, properties of the electrolyte (solution resistance) dominate. Therefore, it is important to obtain a wide range of frequency-dependent data. One of the most common forms of frequency-dependent presentation is the bode plot, in which the magnitude of the impedance and phase is plotted as a function of frequency on a log scale.

The bode plot explicitly shows the frequency at which each data point was taken. This form of data presentation can be used to extract the parameters of the measured system, such as solution resistance, electrode polarization impedance, and cell resistance and capacitance.

When there are no cells present, a single dispersion is seen in the bode plot; and when cells are present on the electrode surface, a second dispersion develops, relevant to cellular characteristics. A slope in the bode magnitude diagram accompanied by a change of phase in the bode-phase plot is referred to as a dispersion. When adherent cells are present in the system, there is a noticeable increase in impedance in the mid-frequency range of the bode plot because the cell membranes act as insulators and 'impede' current flow.

The equivalent circuits used to model the measured data (with and without cells) are illustrated in Figure 6-2(a)-(b). Constant phase elements (CPEs) are used in place of a simple capacitor because the double layer capacitance at the electrode/electrolyte interface is not well-defined by an ideal, simple capacitor. A frequency dispersion exists at the interface; and therefore, system capacitance is better expressed as a CPE. The CPE takes into account non-ideal properties such as surface roughness and heterogeneities, electrode porosity, coating composition, slow adsorption reactions, non-uniform potential and current distributions [30]. Equation 6-1 expresses the impedance of an ideal capacitor, as compared to Equation 6-2, which expresses the impedance of a CPE.

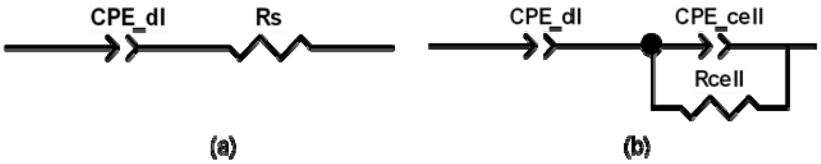

Figure 6-2: Equivalent circuit used to model (a) cell-free or non-adherent cell data; (b) adherent cell data. Constant phase elements (CPE) are used to account for the non-ideal nature of the system.

$$Z_C = \frac{1}{j\omega C} \qquad \text{Equation 6-1}$$

$$Z_{CPE} = \frac{1}{Y(j\omega)^n} \qquad \text{Equation 6-2}$$

where $\omega = 2\pi f$, C is the ideal capacitance, Y is the CPE, and n is a factor between 0 and 1. When $n = 1$, $Z_{CPE} = Z_C$. The phase angle of Z_{CPE} is equal to $-90{*}n$ in degrees.

6.4 Results and Discussion

6.4.1 Baseline Impedance Measurements

Before cell measurements were performed, baseline measurements were conducted with potassium chloride (KCl) to determine the variance among electrodes. This is an important step to confirm that changes in impedance are a function of cell presence, and not electrode variation. An example of KCl measured in one of the devices is shown in Figure 6-3. At low frequencies, properties of the electrode-solution interface are seen, particularly electrode polarization impedance (double-layer capacitance). In the bode magnitude plot (left-axis) it is indicated by a slope. At higher frequencies, the plateau signifies the solution resistance. The phase (right-axis) follows the magnitude plot as it increases from -80 degrees (capacitive) at lower frequencies to less than 15 degrees (resistive) at higher frequencies. Negligible variation was detected between electrodes.

The KCl data was modeled with the equivalent circuit in Figure 6-2a. The average solution resistance and double layer capacitance of eight electrodes in one devices was 1.72 ± 0.04 kΩ and 44.54 ± 3.21 nF, respectively. This was common among all the devices. This shows the consistency among the electrodes themselves.

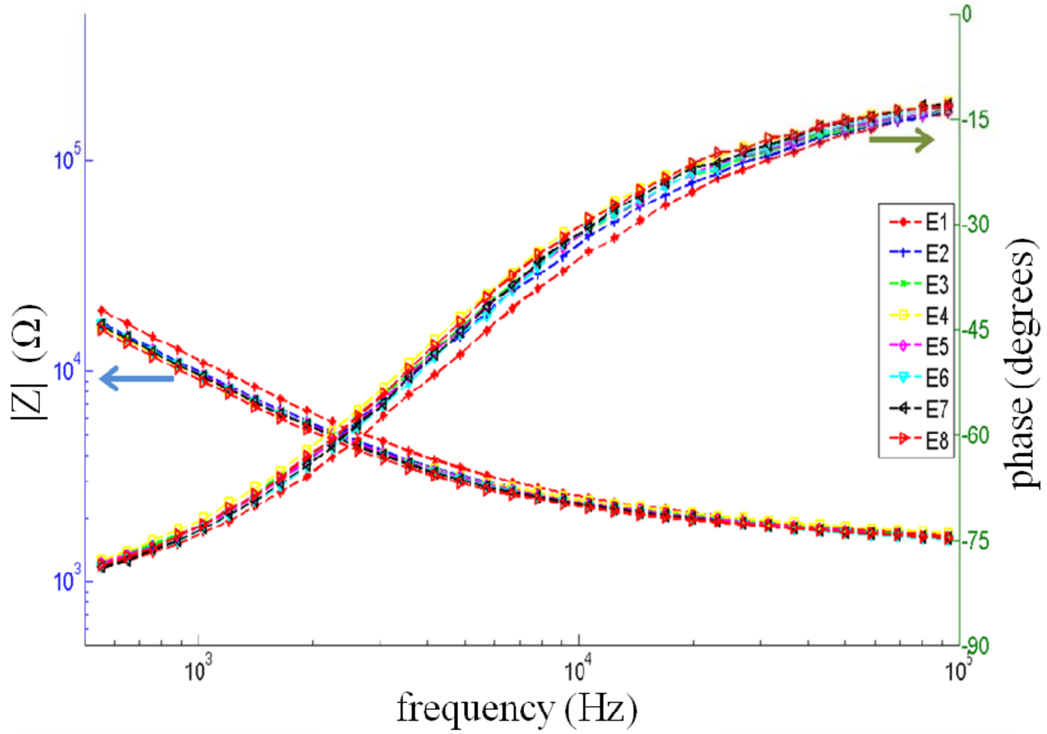

Figure 6-3: Bode plot (magnitude impedance and phase vs. frequency) of baseline measurements using potassium chloride (KCl), showing minimal variation between the eight electrodes of a single device.

6.4.2 Impedance Measurements of Ovarian Cancer Cells

HEY ovarian cancer cells were then seeded onto four electrode devices, each designated for 0, 10, 25, and 50 μM As_2O_3. The cells were allowed to settle and adhere to the electrodes 24 hours before the introduction of As_2O_3. Shortly after As_2O_3 was added to the cells, impedance measurements commenced inside the incubator. Figure 6-4 shows an impedance vs. time plot (averaged across the eight electrodes) illustrating the effects of varying concentrations of the cytotoxic agent on the cells. The variation seen in the measured data highlights the importance of performing multiple measurements within a cell culture. The inset in Figure 6-4 shows an impedance vs. time plot of the 10 μM As_2O_3 device, illustrating the individual impedances of the eight independent electrodes. Two subsets of data are seen in the inset. The impedance of electrodes #1, 2 and 8 is slightly higher than that of the remaining electrodes (#3, 4, 5, 6, and 7). According to the layout of the electrode device, electrodes 1, 2, and 8 are adjacent to each other in the circular array. This demonstrates the enhanced spatial-resolution of this electrode design by quantitatively illustrating that cells had stronger adherence and tight junctions within a location-specific area of the cell culture.

In the main plot, the standard deviation (error bars) show the variance among the independent electrodes for all concentrations of As_2O_3. As the concentrations increase, the magnitude of the standard deviations decreases. The average standard deviations of the impedance over the 24 hour time frame were 2.38, 2.62, 1.03, and 0.35 kΩ for the 0, 10, 25, and 50 μM concentrations respectively. This illustrates the variance of viable cell cultures. As cells begin to die and detach from the electrode surface, the variance decreases since there is less variability across a cell-free electrode. This is also demonstrated by the baseline KCl measurements discussed previously.

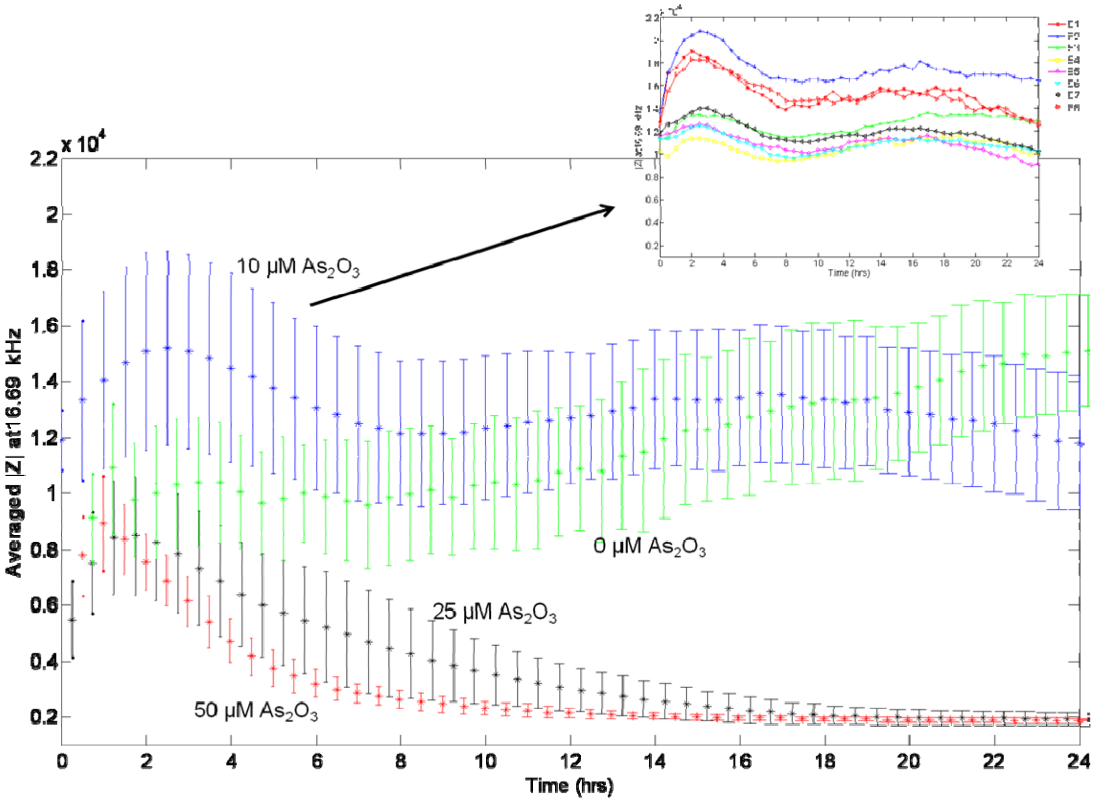

Figure 6-4: Averaged |Z| vs. time at 16.69 kHz of HEY cells introduced to 0, 10, 25, and 50 µM As_2O_3. Measurements of 8 electrodes have been averaged and the standard deviation (error bars) are shown. (Inset) Shows individual impedances (|Z| vs. time) of the 8 independent electrodes within a single device (10µM As_2O_3). Location-specific variation is seen in the impedance data.

The data in the main plot confirms that the HEY cells were able to resist 10µM of As_2O_3 within the time frame shown; however, increased concentrations of As_2O_3 affected the cells and ultimately the cells succumbed and started dying after 3 hours. The impedance of the cells exposed to 10µM of As_2O_3 increase above that of the control, suggesting that the cells formed tighter cell-cell junctions and stronger adherence to the substratum in an effort to resist the cytotoxic agent. Towards 24 hours, the impedance of the control (0µM As_2O_3) cells trended upwards, whereas the impedance of the cells exposed to 10µM As_2O_3 began to trend downwards. The impedance of the control cells steadily increased as the cells adhered and spread onto the electrodes, and subsequently piled on top of each other. The 10μM As_2O_3-treated cells began to succumb to the cytotoxic agent after 22 hours. Further analysis (not shown) demonstrated that the cells eventually died 40 hours after the introduction of 10μM As_2O_3.

Figure 6-5(a)-(d) shows microscopic images of the cells in the electrode devices, 24 hours after the cytotoxic agent was added. The 0 and 10μM As_2O_3-treated cells remained confluent on and around the electrode devices; whereas the 25 and 50μM As_2O_3-treated cells became detached (rounded cells).

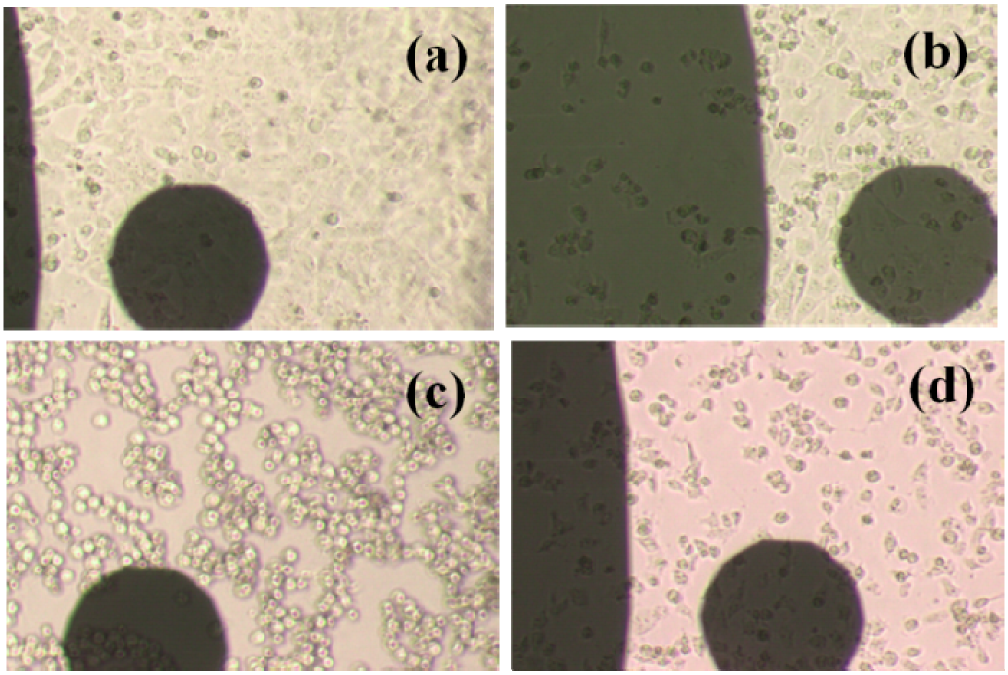

Figure 6-5: Microscopic images of cells 24 hours after the introduction of (a) 0, (b) 10, (c) 25, (d) 50μM of As_2O_3. Cells remained confluent in images (a) and (b); whereas the cells became detached (rounded cells) in images (c) and (d).

6.4.3 Modeling of Impedance Data

Thirty-two frequency-dependent datasets were obtained for each time point, resulting in thousands of datasets per experiment. The vast amount of data required automated data collection and analysis, to facilitate rapid analysis. A Labview program was designed to collect and store the data and a MATLAB program was derived to analyze and model the data to extract system parameters. The MATLAB program used a complex nonlinear least squares (CNLS)-fitting algorithm to fit the data to an equivalent circuit in Figure 6-2(a)-(b). Figure 6-6 shows an example of the measured data overlaid by the modeled data in the form of a bode plot. The equivalent circuit parameters that describe the system are shown underneath the plot.

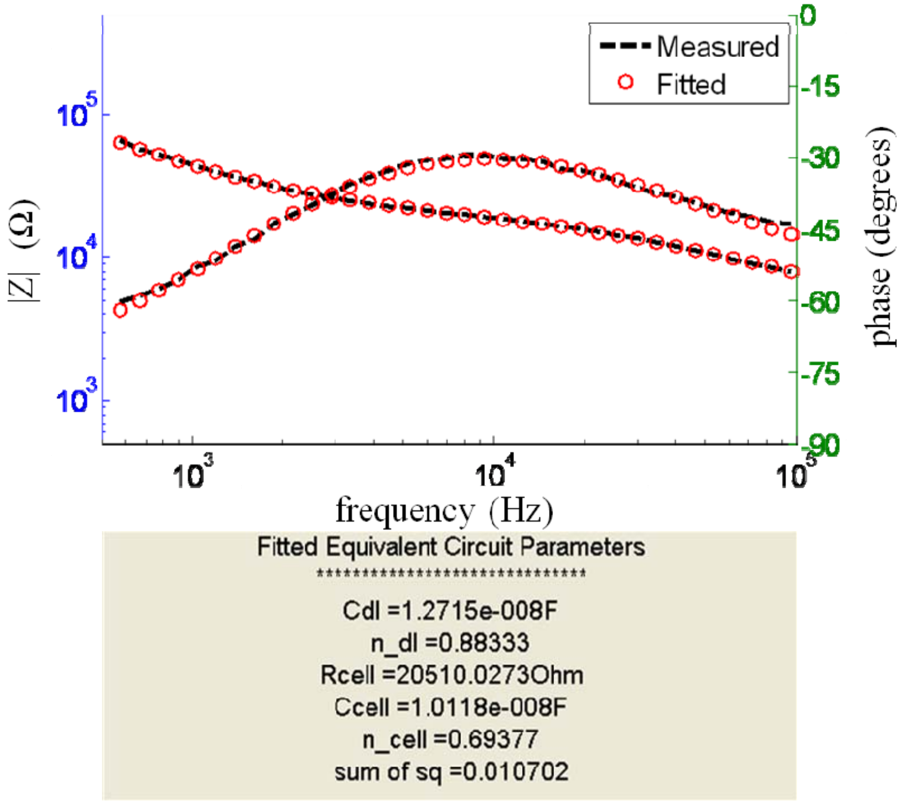

Fitted Equivalent Circuit Parameters
****
Cdl =1.2715e-008F
n_dl =0.88333
Rcell =20510.0273Ohm
Ccell =1.0118e-008F
n_cell =0.69377
sum of sq =0.010702

Figure 6-6: Bode plot of measured and fitted data 12 hours after the introduction of 10μM of As_2O_3 for a single electrode (Electrode #2). Equivalent circuit parameters are shown below the plot.

At low frequencies (<3 kHz), the bode plot exhibits electrode polarization impedance or double layer capacitance. At mid frequencies (>3 kHz and <20 kHz), cell resistance dominates. Above 20 kHz, cell capacitance dominates. Since the impedance of the cell capacitance and resistance is greater than the solution resistance up to 100 kHz, solution resistance cannot be modeled within this frequency range. Table 6-1 contains averages of the extracted system parameters using the equivalent circuits in Figure 6-2(a)-(b), 12 hours after the introduction of 0, 10, 25, and 50μM As_2O_3. The extracted parameters include solution resistance, Rs; double layer capacitance, Cdl; cell resistance, Rcell; and cell capacitance, Ccell. The sum of squared error (SSE) parameter in Table 6-1 describes the 'goodness of the fit' (the smaller the number, the better the fit). The average SSE value for all measurements was between 0.5 and 13.5%.

Table 6-1: Extracted system parameters (solution resistance, Rs; double layer capacitance, Cdl; cell resistance, Rcell; cell capacitance, Ccell; and sum squared error, SSE) 12 hours after the introduction of 0, 10, 25, 50μM of As_2O_3 (averages and standard deviations).

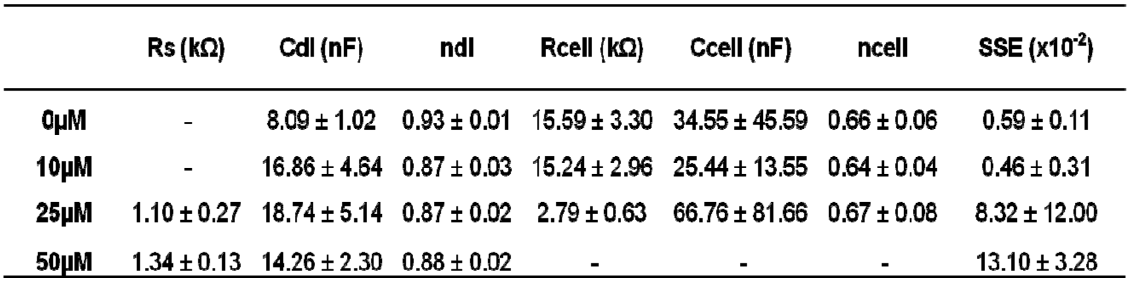

	Rs (kΩ)	Cdl (nF)	ndl	Rcell (kΩ)	Ccell (nF)	ncell	SSE ($x10^{-2}$)
0μM	-	8.09 ± 1.02	0.93 ± 0.01	15.59 ± 3.30	34.55 ± 45.59	0.66 ± 0.06	0.59 ± 0.11
10μM	-	16.86 ± 4.64	0.87 ± 0.03	15.24 ± 2.96	25.44 ± 13.55	0.64 ± 0.04	0.46 ± 0.31
25μM	1.10 ± 0.27	18.74 ± 5.14	0.87 ± 0.02	2.79 ± 0.63	66.76 ± 81.66	0.67 ± 0.08	8.32 ± 12.00
50μM	1.34 ± 0.13	14.26 ± 2.30	0.88 ± 0.02	-	-	-	13.10 ± 3.28

The average cell resistances and cell capacitances for the 0 and 10μM As_2O_3-treated cells were similar: $Rcell_{0\mu M}$ = 15.59kΩ and $Rcell_{10\mu M}$ = 15.24kΩ, and $Ccell_{0\mu M}$ = 34.55nF and $Ccell_{10\mu M}$ = 25.44nF. The average cell resistance for the 25μM As_2O_3-treated cells decreased ($Rcell_{25\mu M}$ = 2.79kΩ), as cells began to detach from the surface, in contrast, the capacitance increased ($Ccell_{0\mu M}$ = 66.76nF). Some of the electrodes showed no cell presence, as the detachment of cells were more prominent.

Therefore, some electrodes within this device were modeled with the cell-free equivalent circuit. At 12 hours, the 50μM As_2O_3-treated cells showed no presence of adherent cells on the electrodes, as the majority of the cells detached from the electrode surface as a result of cell death.

In Figure 6-7(a), the electrodes in the 0 and 10 μM As_2O_3 wells show some location-specific variation, with an average cell resistance value close to 15 kΩ. This demonstrates that within certain areas of the cell culture, the cells had a stronger adherence to the substratum and each other than in other areas. Similarly, Figure 6-7(b) shows some variance in cell capacitance, though an outlier exists from electrode 5 in the 0 μM As_2O_3 well. The lower resistance and significantly higher capacitance of electrode 5 indicates that the cells did not adhere as well, and highlights the importance of making multiple measurements within a cell culture, to account for such variations. The 10 μM As_2O_3 well had similar properties to that of the control because the toxin had a negligible effect on the HEY cells at 12 hours. A difference, however, is seen in the double-layer capacitance (Table 6-1), which increased with the addition of As_2O_3. This increase occurred in all As_2O_3-containing cell cultures and could be attributed to the change in ion concentration with the addition of As_2O_3 to the culture medium.

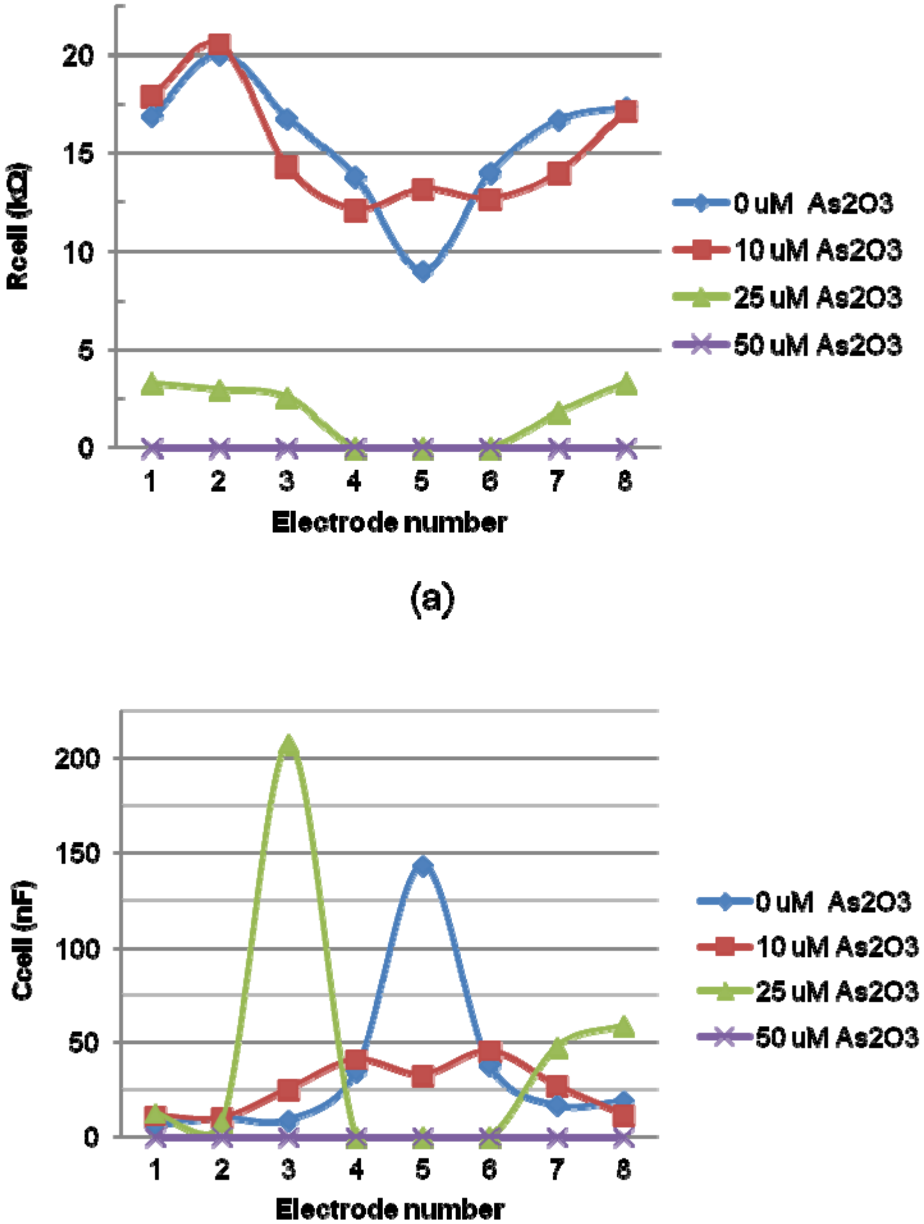

(a)

(b)

Figure 6-7: (a) Extracted cell resistance and (b) cell capacitance 12 hours after the introduction of 0, 10, 25, 50μM of As_2O_3 for each independent electrode within the four wells. (●-0μM, ■-10 μM, ▲-25 μM , x-50 μM).

The well containing 25 μM As_2O_3 showed apparent differences in cellular properties compared to the 0 and 10 μM As_2O_3 wells. There was a heterogeneous reaction of the cells to the cytotoxic agent. At 12 hours, there was complete detachment of cells from some electrodes, and on other electrodes, cells remained loosely attached. This is indicated by the low resistance values in Figure 6-7(a) for the electrodes showing some cell presence. The low resistance values are a result of the cells detaching from the surface and reduced formation of cell tight junctions. As a result, the current can flow more easily underneath and between the cells, causing a decrease in resistance. When the majority of the cells are detached from the electrode, cell presence is not detected and the Rcell value is zero. The data from these electrodes are then modeled with the cell-free equivalent circuit (Figure 6-2(a)), which provides a more acceptable SSE value. The SSE value for the 25 μM As_2O_3 well was higher than the 0 and 10 μM As_2O_3 wells because it is harder to fit partially covered electrodes to the equivalent circuit model, which is most suitable for confluent cell layers [111]. Therefore, the high capacitance outlier of electrode 3 could be a result of a poor fit. The slightly higher capacitance values of electrodes 7 and 8 (10 μM As_2O_3) are attributed to membrane folding (increased surface roughness) [114]. The 50 μM As_2O_3 well has completely succumbed to the toxin at 12 hours, so the Rcell and Ccell values are zero for all electrodes, indicating complete cell detachment. All electrodes were modeled with the cell-free equivalent circuit.

6.5 Conclusion

A novel 8-electrode impedance system has been evaluated and the importance of multiple measurements within a cell culture has been demonstrated through monitoring the effect of As_2O_3 on ovarian cancer cells. Impedance spectroscopy, a non-destructive, label-free technique, allowed continuous measurement of cellular properties over 24 hours, without adversely affecting the cells. The data illustrated that the non-uniform response of cells within a culture required the need for redundant measurements in order to obtain statistically-significant data, especially in drug discovery applications. High-throughput systems are vastly desirably in drug discovery, and these systems typically output large datasets. This work validated an impedance system that implemented automated and rapid data collection and analysis through the design and implementation of a switching circuit, Labview, and Matlab programs. This design can serve as a foundation for higher-level multiplexed systems with a greater number of independent electrodes and/or devices to obtain statistically-significant data for numerous applications.

Chapter 7 Electrical Comparison of Healthy and Cancer Ovarian Cells

7.1 Introduction

Ovarian cancer is the 5th most common cancer among women, with approximately 22,000 new cases and over 15,000 deaths estimated in 2011 [19]. Treatment typically involves surgical debulking followed by chemotherapy (i.e. platinum and taxane-based agents used specifically for ovarian cancer treatment) [115], which often targets normal cells in addition to the abnormal cells. This leads to side effects such as hair loss, fatigue, and low blood cell counts. As a result, chemotherapeutic drugs require extensive characterization and validation before they can be used clinically. This can be a cumbersome task, as many variables are present when determining the drug's effectiveness, including concentration, time, cell line, and microenvironment.

Qualitative measurements (i.e. western blots, optical microscopy, biomarkers) used to identify and validate the effects of chemotherapeutic drugs are typically performed at standard intervals (such as 0, 3, 9, 18 hours) [116]. These intervals are chosen based on other published studies, predefined protocols, or trial-and-error. However, when a new cell line or drug is introduced, these intervals may not be optimal, i.e. a reaction occurring one hour after the introduction of a stimulant may be overlooked. Since qualitative methods are time consuming, labor intensive, and typically endpoint assays, it is not feasible to determine cell- or drug-specific time points through real-time monitoring. Additionally, it is unrealistic to perform qualitative measurements continuously. Impedance spectroscopy, on the other hand, offers a label-free, non-destructive, quantitative measurement technique that can be used to continuously monitor cells. With real-time impedance measurements, cellular responses can be captured at numerous time points. Thus, when a reaction is observed, qualitative measurements can be focused at that specific time point(s). Therefore, it is hypothesized that impedance monitoring performed prior to qualitative studies can (1) determine the optimum time points for measurements, (2) reduce the number of qualitative measurements needed to obtain relevant data, and (3) reduce the amount of time and expensive reagents needed to complete an experiment.

In impedance spectroscopy measurements, a small AC electrical signal is passed and measured between a pair of electrodes. The technique uses a small gold electrode (250 μm in diameter) that can measure approximately 50 to 100 cells, dependent on cell-type. When cells attach and spread onto the surface of the electrode, the measured impedance of the system increases because the insulating cell membranes block current flow. Thus, cell viability, death, and micromotion can be detected with high sensitivity [2, 6, 8, 74]. This technique is commonly referred to as electric cell-substrate impedance sensing (ECIS). Giaever and Keese pioneered the ECIS technique [108] and developed it into a commercial system (available through Applied Biophysics) that allows real-time impedance measurements inside a humidified incubator.

This chapter replicates a recently reported qualitative study [116] to understand the effects of arsenic trioxide (As_2O_3) on both T80 (normal) and HEY (cancer) ovarian cells. There are only a few reports that investigate specifically T80 and HEY cells [117-119], comparing their response to chemotherapeutic drugs (normal versus cancer cells). There is one known impedance study using HEY cells [120] in which impedance was measured to monitor the invasive potential of ovarian cancer cells into a peritoneal mesothelial cell monolayer by quantifying the timing and extent of invasion. In particular, they emphasize the advantages of the impedance measurement system, including high sensitivity and the ability to follow real-time changes (as opposed to endpoint assays) [120]. Herein, we performed continuous impedance measurements on normal and cancer ovarian cells to determine if biologically significant information could be obtained at time points other than the standard intervals used previously [116]. In addition, a quantitative comparison of the impedance signatures of the T80 and HEY cells was performed to show that the cells could be differentiated based on their electrical properties.

7.2 Methods and Materials

7.2.1 Cell Culture

HEY ovarian carcinoma cells and T80 (large T antigen/hTERT immortalized normal ovarian surface epithelial cells) were kindly provided by Dr. Gordon Mills (MD Anderson Cancer Center, Houston, Texas). Both cell lines were cultured in RPMI 1640, supplemented with 8% FBS and penicillin/streptomycin. The cells were maintained in a humidified 37^0C incubator containing 95% air and 5% CO_2. For all experiments, cells were detached from flasks with trypsin-EDTA solution and plated into the ECIS chamber at a concentration of 300,000 cells/mL prior to any treatment with drugs. Arsenic trioxide (As_2O_3) was obtained from Sigma-Aldrich. Cells were treated with varying doses of As_2O_3 (0-50 µM).

7.2.2 Impedance Measurements

The ECIS ® Zθ system, provided by Applied Biophysics [41], was used to perform all impedance measurements. The system supplies a small AC current between 64 Hz and 64 kHz across the electrodes and performs continuous measurements of the cell cultures while inside an incubator. 8W1E electrodes arrays (8-well plates with a single 250 µm-diameter working electrode) from Applied Biophysics were used for all experiments. Figure 7-1 shows an image of the device, provided by Applied Biophysics.

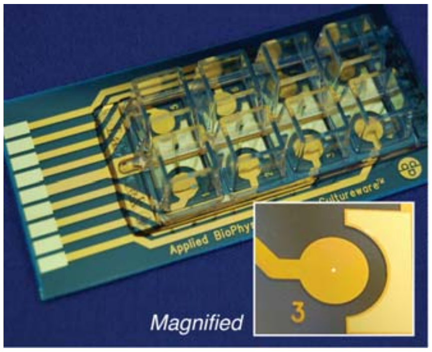

Figure 7-1: Photograph of ECIS 8W1E device (Applied Biophysics)

Three independent experimental designs were conducted. In the first experimental design (Experiment 1), T80 and HEY ovarian cells were seeded into two 8W1E devices. The cells were allowed to settle and adhere to the electrodes for approximately eight hours prior to the introduction of As_2O_3. As_2O_3 was then added directly to the existing medium. All treatments were performed in duplicates (replicate wells) as follows: (1) two wells served as the controls (in the absence of As_2O_3, 0 µM); (2) two wells contained 10 µM of As_2O_3; (3) two wells contained 25 µM of As_2O_3; and (4) two wells contained 50 µM of As_2O_3. Impedance measurements commenced immediately after the introduction of As_2O_3, and continued for up to 20 hours following treatment. In the second experimental design (Experiment 2), the setup was similar to Experiment 1 with the exception of As_2O_3 being added via a change in cell culture medium. In the third experimental design (Experiment 3), the cells were allowed to settle and adhere for 24 hours prior to the addition of As_2O_3, which was similarly added via a change in medium.

7.3 Results and Discussion

Impedance responses of the T80 (normal) and HEY (cancer) cells to the cytotoxic effects of As_2O_3, a pro-death agent used in the clinic to treat patients with acute promyelocytic leukemia (APL), were assessed via use of the ECIS system. Three different experimental designs (as described in the Materials and Methods section) were evaluated to investigate the effects of medium change and confluence on cellular responses to the cytotoxic agent. The results are displayed in graphical format as changes in impedance across time (Figure 7-2 through Figure 7-4) after the introduction of As_2O_3 to the cell cultures.

7.3.1 Experiment 1: No Culture Medium Change

Figure 7-2(a) shows the results of Experiment 1 for T80 and HEY cells, respectively. The curves are averages of the 2 wells, with error bars, displayed as standard deviations. Due to occasional leakage or electrical disconnects, some data from the duplicate well was not collected; in this regard, data from single wells is displayed without error bars. Based on the impedance measurements shown in Figure 7-2(a), the impedance of the T80 control cells (0 µM) gradually increased from 4 to 8.5 kΩ over the 20 hour time frame. This increase is attributed to the cells adhering and spreading on the electrode surface. Cell membranes are insulating and thus block current flow as it travels from one electrode to another. Current is subsequently forced to travel between the tight-junctions of the cells or between the cell and substratum, typically nanometer-sized gaps. As cells continue to spread onto the electrode, these gaps become less prominent and measured impedance continues to increase over time. T80 cells treated with 10 µM As_2O_3 appeared to resist the effects of As_2O_3 for a longer time period (approximately 5 hours) and underwent complete cell death beyond 20 hours.

In contrast, As_2O_3 at a concentration of 25 and 50 µM had the most detrimental effects on the normal T80 cells with a marked effect on cell viability a little more than one hour following the addition of the cytotoxic agent.

In contrast to the normal T80 cells, the HEY ovarian carcinoma cells (in Figure 7-2(b)) appeared to be more resilient to the cytotoxic effects of As_2O_3. Within the first two hours, the impedance of the As_2O_3 treated HEY cells sharply increased above that of the control. On average, the impedance of the As_2O_3 treated cells nearly doubled that of the control. We propose that this could be attributed to the formation of tighter cellular junctions between the cells with increased substrate adherence leading to resistance to the detrimental cytotoxic effects of As_2O_3. The HEY cells treated with 25 and 50 µM As_2O_3 underwent cell death after 4-5 hours of treatment, whereas the HEY cells were completely resistant to the effects of 10 µM As_2O_3. The impedance of the HEY control cells (0 µM) gradually increased from 3 to 4 kΩ over the 20 hour time frame. The overall impedance of the HEY cells was less than that of the T80 cells. The cause of this impedance difference is discussed later on in this section.

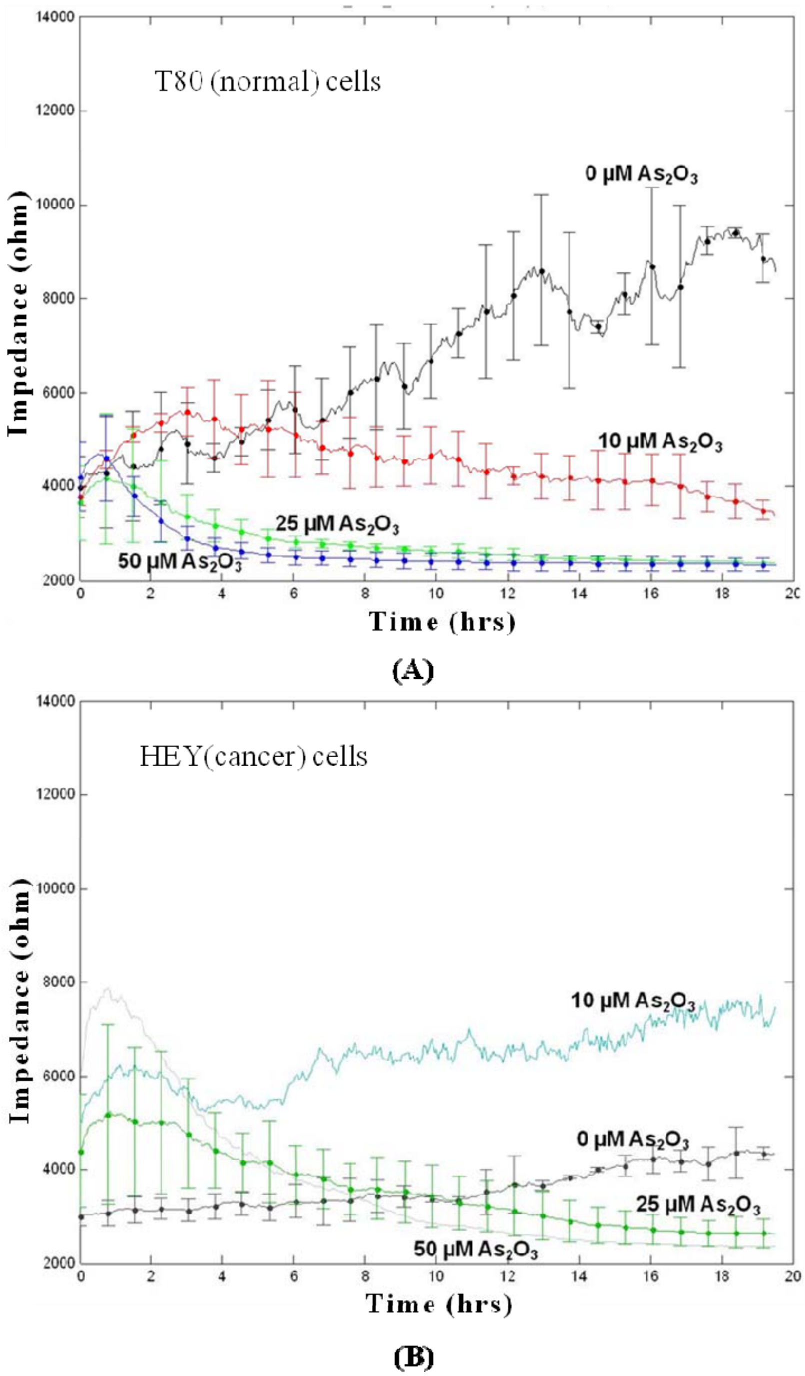

Figure 7-2: Experiment 1- Impedance vs. time plots of (A) T80 and (B) HEY cells, where As_2O_3 was added to existing medium 8 hours after seeding cells. All concentrations of the cytotoxic agent had an effect on the T80 cells; more so the 25 and 50 µM than the 10 µM As_2O_3. On the contrary, the HEY were able to resist the 10 µM As_2O_3; however, the cells did succumb to the 25 and 50 µM.

7.3.2 Experiment 2: Culture Medium Change

In Experiment 2, As_2O_3 was added to the T80 and HEY cells through a change in culture medium. The impedance trends (Figure 7-3(a-b)) were similar to that of Experiment 1, with minor differences. One of the differences is noticed between the control (0 μM) cells. When the medium was not changed on the T80 cells (Figure 7-2(a), 0 μM As_2O_3), the impedance gradually and consistently increased over time; however, when the medium was replaced (Figure 7-3(a), 0 μM As_2O_3), the impedance remained nearly constant for the initial seven hours, and then it gradually increased thereafter. We hypothesize that these changes could be due to removal of non-adherent cells in conjunction with a lengthened time for the cells to adhere across the entire electrode surface thus resulting in a delayed increase in impedance. The influence of the As_2O_3 on the T80 cells is similar in both Experiments 1 and 2. On the contrary, 10 μM As_2O_3 had a greater effect on the HEY cells that experienced a medium change. This suggests that the medium change resulted in less cell presence and thus reduced formation of tight-junctions and reduced cell-cell communication to fend off the cytotoxic agent.

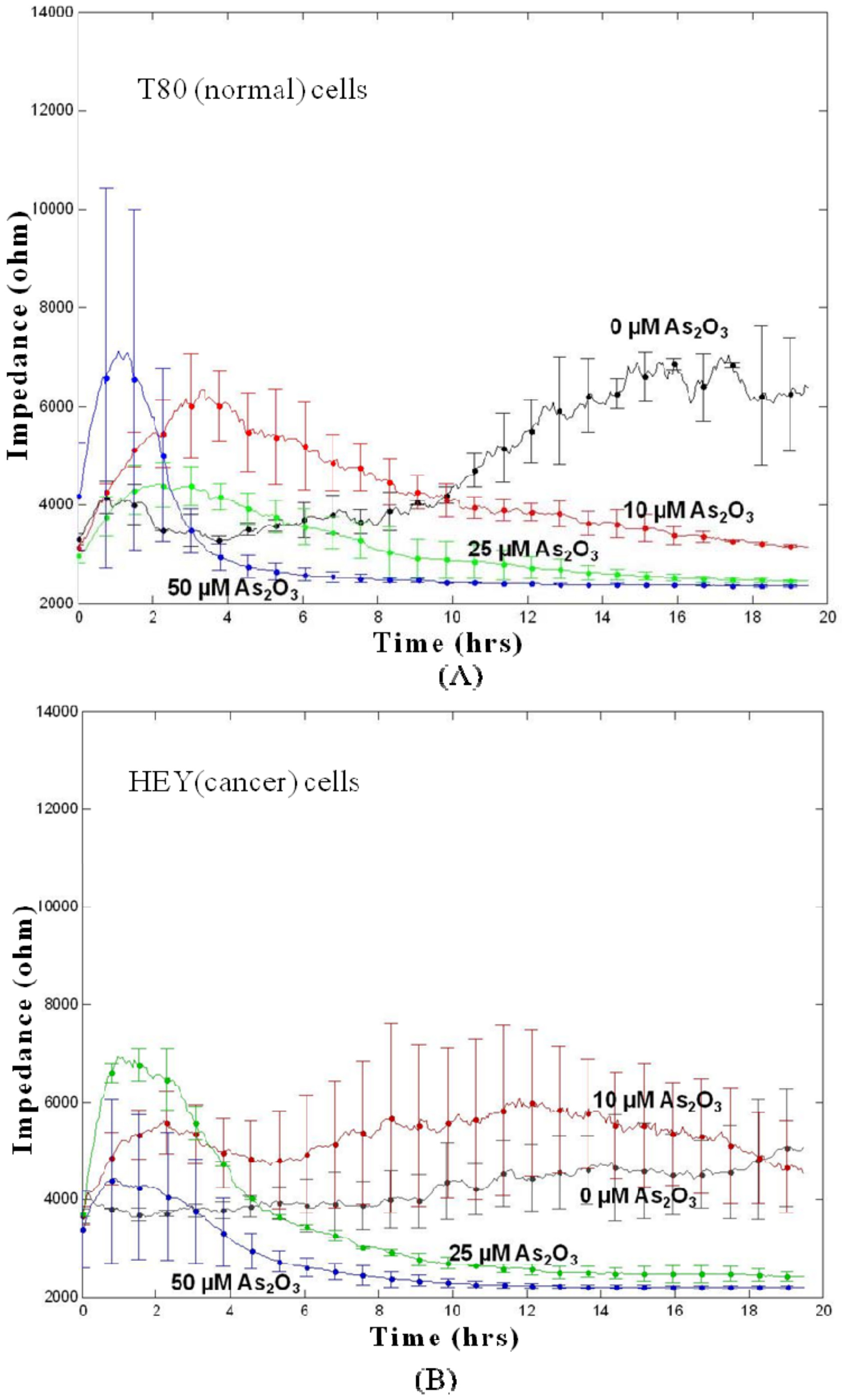

Figure 7-3: Experiment 2- Impedance vs. time plots of (A) T80 and (B) HEY cells from Experiment 2, where As_2O_3 was added through a medium change 8 hours after seeding cells. Different from Experiment 1, when the medium was changed, non-adherent cells were removed, resulting in a delayed increase in impedance.

7.3.3 Experiment 3: Increased Cell Confluence

In Experiment 3 in which the cells settled and adhered for 24 hours prior to the introduction of As_2O_3 (Figure 7-4(a-b)), the cells formed a completely confluent layer across the electrodes prior to treatment with the cytotoxic agent. The higher impedance values of Experiment 3, compared to Experiments 1 and 2, signify that the cells are confluent and even forming multiple layers. The impedance data indicates that increased cellular confluence before cytotoxic agent treatment allows the cells to become more resistant to the As_2O_3. This in part was due to the cells forming confluent, multiple layers, stronger cell-cell tight junctions, and potentially more signaling pathways. This is consistent with studies indicating that 3D cell cultures can resist cytotoxic agents better than 2D cultures[121], due to the complex mechanical and biochemical interactions of 3D cell cultures.

The impedance of the T80 cells with 10 μM of As_2O_3 initially spiked, and then gradually decreased. However, 20 hours after the addition of As_2O_3, there were still some viable cells present, as seen by the micromotion or small fluctuations in the impedance. The impedance of the T80 cells with 25 μM of As_2O_3 increased sharply immediately after its addition; however, in contrast to the 10 μM concentration, the impedance quickly dropped after six hours. The cells were unable to resist the higher concentrations of As_2O_3 and complete cell death occurred around 15 hours. Similarly, the impedance of the 50 μM As_2O_3–treated T80 cells sharply increased within the first hour, though quickly decreased within two hours, and complete cell death followed shortly thereafter.

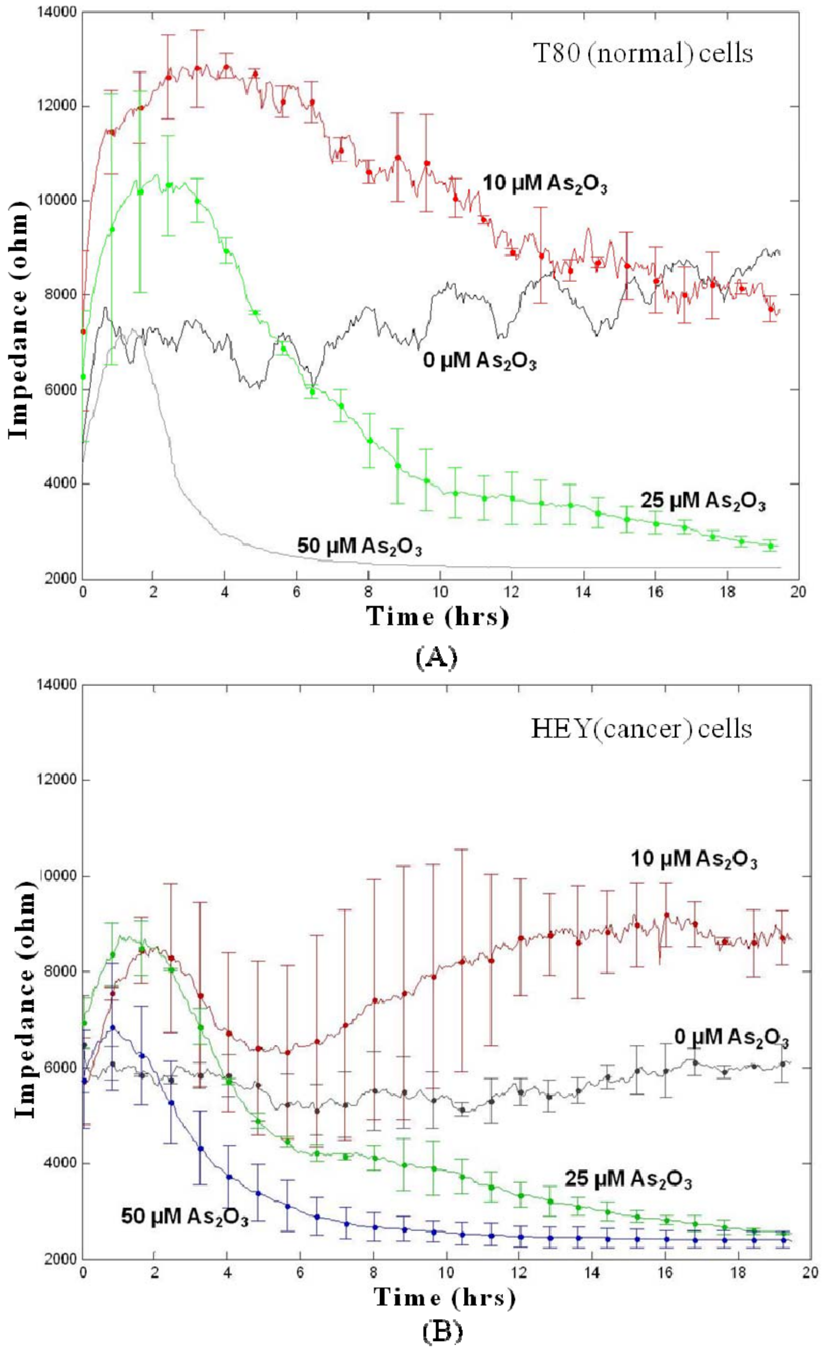

Figure 7-4: Experiment 3- Impedance vs. time plots of (A) T80 and (B) HEY cells from Experiment 3, where As_2O_3 was added through a medium change 24 hours after seeding cells. Both cell lines were less sensitive to the lower concentrations of the cytotoxic agent, compared to Experiments 1 and 2. This is attributed to the cells forming confluent multi-layers, resulting in stronger tight-junctions and substratum adherence, and thus an increased resist to the As_2O_3. The initial impedance spikes within the first 2 hours also validate that the cells are developing a stronger adherence to resist the cytotoxic agent.

The effect of the As_2O_3 on the HEY cells was similar to that of the T80 cells; however, the main difference is that the 10 μM As_2O_3 –treated cells were able to resist the cytotoxic agent. The impedance of these cells was greater than that of the control, indicating that stronger adhesions and tight-junctions were formed. Microscopic images of the cells treated with 0, 10, 25, and 50 μM of As_2O_3 after 24 hours is shown in Figure 7-5.

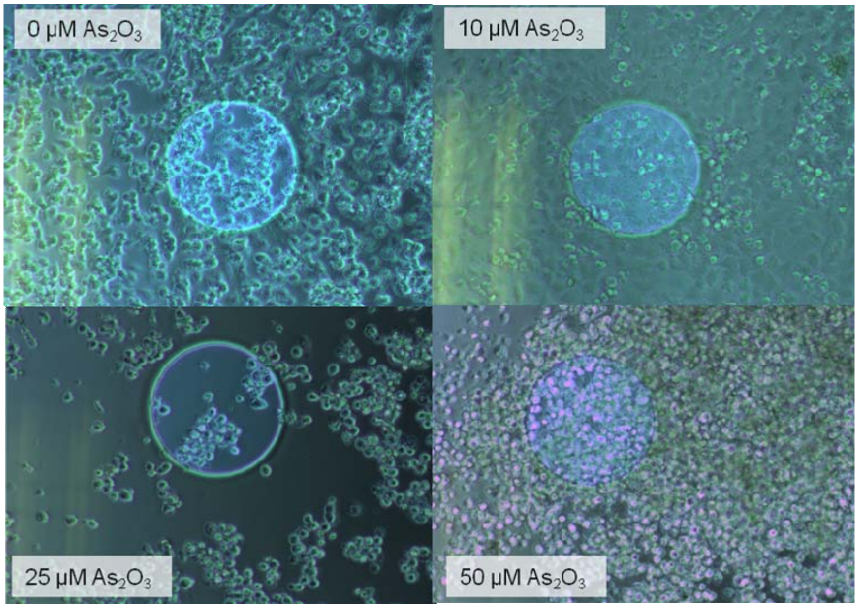

Figure 7-5: Microscopic images of HEY cells 24 hours after the addition of 0, 10, 25, and 50μM of As_2O_3. Complete cell death is seen in the wells containing 25 and 50uM of As_2O_3; whereas cells treated with 0 and 10uM of As_2O_3 remain mostly adherent.

Table 7-1: Significant time points from Experiments 1, 2, and 3 for the T80 and HEY cells

	T80	HEY
	Significant time points (hours)	Significant time points (hours)
Exp 1	1, 3, 5	1, 8
Exp 2	1, 4, 10	2, 5, 19
Exp 3	1, 5, 15	1, 6, 16

The time points in which significant events occurred with the ovarian cells are highlighted in Table 7-1. The times were chosen based on changes observed in the impedance vs. time plots. For example, the key time points from Experiment 3 (T80 cells) were (a) 1, (b) 5, and (c) 15 hours. At these points, (a) the initial spike occurred, (b) the cells containing 50 μM As_2O_3 die off and detach from the electrode, and (c) then the cells containing 25 μM As_2O_3 begin to die and the impedance of the 10 μM began to decrease below that of the control. The time points varied with cell type, confluence (cell-substratum adherence and cell-cell tight junctions), and drug concentration, demonstrating the importance of pinpointing unique time frames for different cell types and drug concentrations. To obtain more insight into the underlying mechanisms of these observed changes, biological assays can be performed at these personalized times.

Light microscopic images (Figure 7-6(a-d)) of cells treated with As_2O_3 within the initial 2-hour time frame were captured to determine whether observable physical changes were occurring to the cells' morphology, which could likely correlate with the increased impedance measured during this time initial time frame (see Figure 7-2 through Figure 7-4). As_2O_3 (25 μM) was added to HEY cells 24 hours following seeding. Images were captured at 0, 1, 1.5, and 2 hours following the introduction of the cytotoxic agent. The images demonstrate that the morphology of the cells changed from an elongated shape to a more rectangular structure with clear protrusions along the cellular edges. These observable physical changes in the cells appear to correlate with the altered impedance within the same time period.

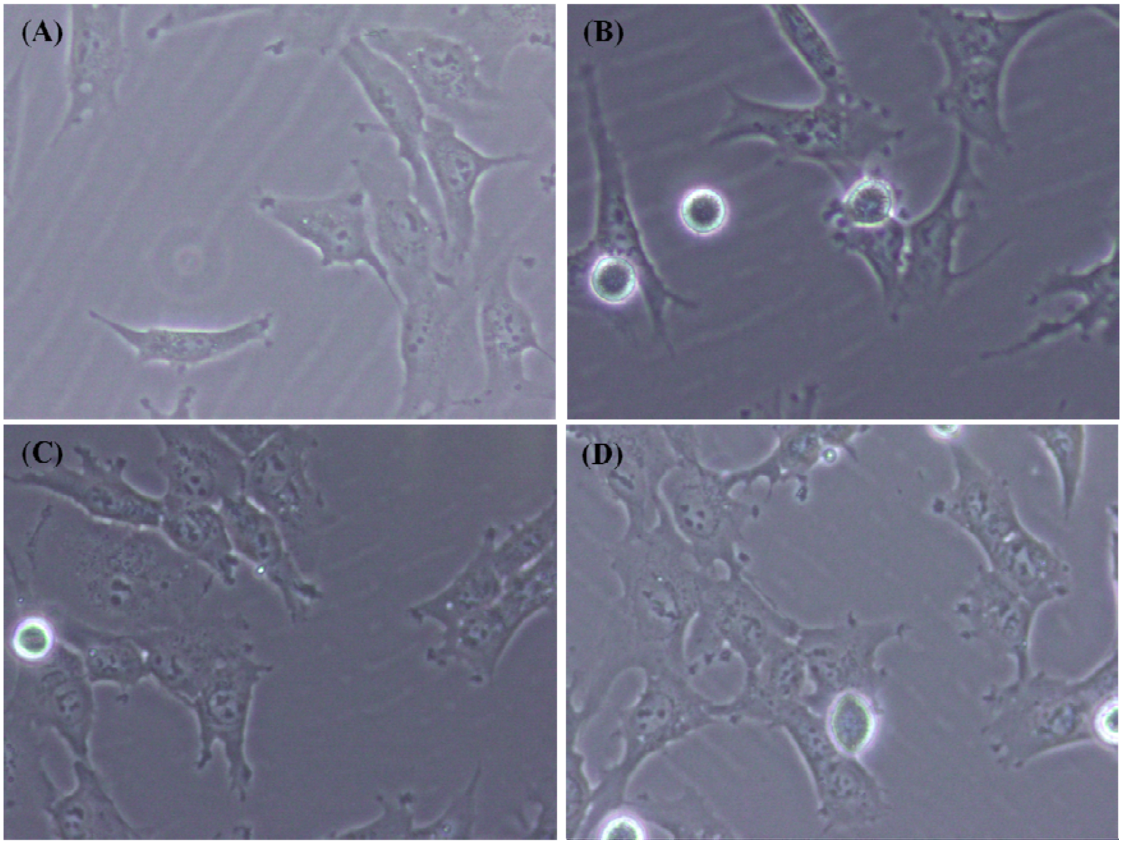

Figure 7-6: Microscopic images of HEY cells 0, 1, 1.5, and 2 hours after the introduction of 25 μM As_2O_3. The images illustrate the effect of the cytotoxic agent on the cells within 2 hours. The morphology of the cells changed from a more elongated shape to a more rectangular structure and there are additional protrusions along the edges of the cells.

7.3.4 Comparison of T80 and HEY Cell Impedance Signatures

The results of this work also demonstrated that normal and cancer ovarian cells can be quantitatively differentiated using impedance analysis. Figure 7-7 illustrates a difference in impedance between T80 and HEY cells from Experiment 1. After 20 hours of monitoring, the T80 cells had a greater overall impedance, and a smaller capacitance than the HEY cells, in all three experiments. The extracted impedances and capacitances of the T80 and HEY cells after 20 hours of monitoring are listed in Table 7-2.

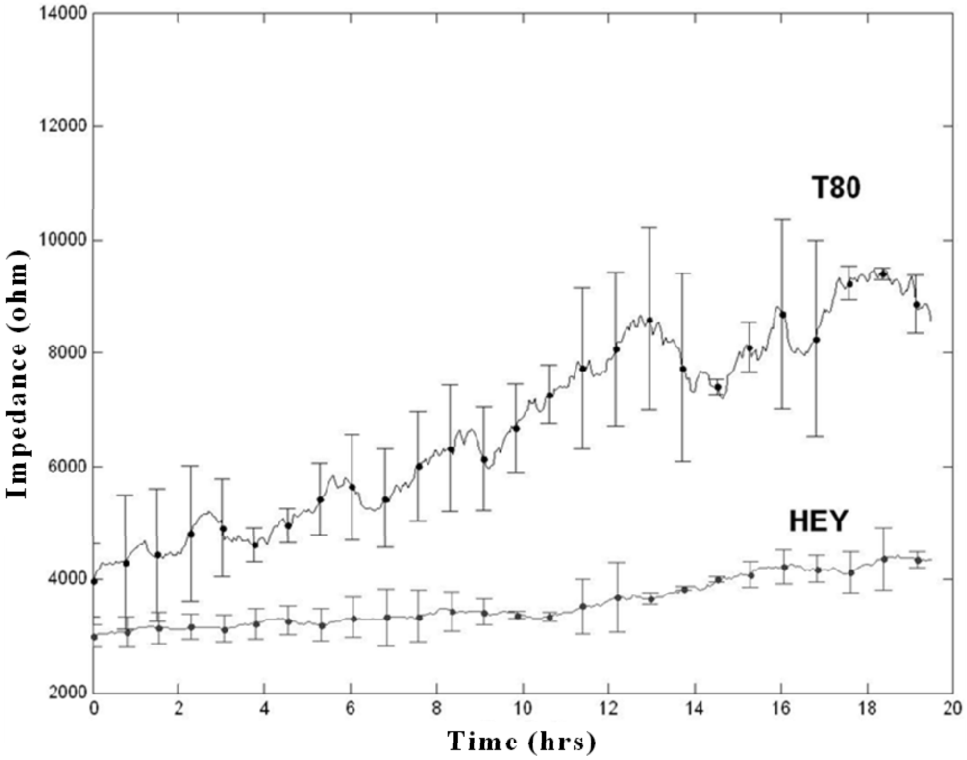

Figure 7-7: Comparison of the impedances of T80 and HEY ovarian cells from Experiment 1, 0 μM As_2O_3. Measurements commenced 8 hours after seeding cells and the cell culture medium was not changed. The impedance of the cells increased over time as the cells adhered and spread onto the electrodes; however the impedance of the normal T80 cells is greater than that of the HEY cells. This is attributed to a weaker adhesion of the HEY cells to the substratum because they are less contact inhibited.

Table 7-2: Impedances and capacitances of the T80 and HEY cells after 20 hours of monitoring, for the three experiments

	T80		HEY	
	Impedance (kΩ) at 16 kHz	Capacitance (nF) at 16 kHz	Impedance (kΩ) at 16 kHz	Capacitance (nF) at 16 kHz
Experiment 1	8	1.75	4	3.2
Experiment 2	6.5	2.5	4.5	3.25
Experiment 3	13	2	10	2.75

The impedances are notably higher in Experiment 3 because the cells adhered and spread for 24 hours prior to monitoring as opposed to 8 hours of adherence for Experiments 1 and 2. A cell membrane capacitance of 1 μF/cm^2 is generally accepted in literature[122]. In Experiment 3, the average cell capacitances of the T80 and HEY cells were 4 μF/cm^2 and 5.6 μF/cm^2. These values are higher than the generally accepted value because they also incorporate properties of the entire cell layer(s), including trans-cellular junctions and folded cell walls [75]. It is hypothesized that the HEY cells have a higher capacitance per area because they are more likely to form multiple layers.

The higher impedance of the T80 cells over the HEY cells can be attributed to the smaller capacitance and a higher resistance, which results from stronger substratum-cell adhesion and cell-cell interactions. It is expected for cancer cells to have a weaker adhesion to the substratum because they are less contact inhibited. Zou and Guo [42] also suggests that due to increased cellular water and salt content, altered membrane permeability, and changed packing density, malignant tumors typically exhibit a lower electrical impedance.

This is consistent with our results presented herein in that the HEY cells have a higher capacitance, which translates to a lower impedance by the following definition:

$$Z = \frac{1}{j\omega C} \qquad \text{Equation 7-1}$$

7.4 Conclusion

This work demonstrates that impedance measurements may be a beneficial tool for optimizing drug-screening biological assays by pinpointing specific time points for functional assessments generating important data regarding (1) cell type, (2) confluence (time), and (3) drug concentrations. As a result, this eliminates excessive experimental trials needed to prior to the identification of optimal time points for biological measurements and obtaining relevant information with respect to cell-drug interactions. The impedance data indicates that 25 and 50 µM As_2O_3 is detrimental to both the T80 and the HEY cells, leading to extensive cell death within a 6 hour period. In contrast, both cell lines treated with to 10 µM of As_2O_3 were able to resist its effects for a longer time frame. In addition, we noted that the normal T80 cells, as reported [116], were more sensitive to the As_2O_3 than the ovarian cancer HEY cells. This was especially apparent in the cell cultures treated with 10 µM of As_2O_3. The impedance of the T80 cells fell below that of the controls (0 µM As_2O_3) faster than the HEY cells, which in some experiments did not succumb to the cytotoxic agent at 10 µM. This variance in cell responses with different variables reveals the need for unique timestamps when studying cell-drug interactions. Therefore, we propose that measurements of impendence can be utilized to identify critical time points when investigating cell-drug interactions.

Chapter 8 Conclusions and Future Work

This work has demonstrated the cycle of electrode optimization, design, fabrication, testing, and validation. An existing electrode design was modified to suppress the parasitic contribution of the passivation layer to allow measurements at higher frequencies. The design rule derived in this work was applied to the new design, which incorporated 8 independent working electrodes to allow multiple measurements within a cell culture chamber. In order to obtain statistically relevant data, acquisition of multiple data points in a cell culture is essential since cells may adhere, react, and behave slightly different in under various conditions and locations. The effect of arsenic trioxide (As_2O_3) on ovarian cancer cells was continuously monitored inside of an incubator. A switching circuit and Labview program was developed to automate the measurements, and switch between the 8 electrodes on 4 separate devices. System parameters (solution resistance, double layer capacitance, cell resistance and membrane capacitance) were extracted using the equivalent circuit modeling technique. A MATLAB program was derived to perform a complex non-linear least squares (CNLS) algorithm to fit and visualize the large data sets.

Applied Biophysics' commercial ECIS system was used to validate the measurements performed by the 8-electrode system and compare the electrical properties of normal and cancer ovarian cells and their responses to As_2O_3. Similar trends were seen between the commercial and 8-electrode systems. The work performed on the commercial system demonstrated that the 25 and 50μM concentrations of As_2O_3 were detrimental to both the T80 and the HEY cells. In contrast, the cell lines were able to resist 10 μM of As_2O_3 for a longer period of time. The T80 cells, however, were slightly more sensitive to the As_2O_3 than the HEY cells. When the cells settled and adhered for a longer period of time (24 hours) before adding the As_2O_3, they became more resilient to the drug.

Lastly, a comparison of the 2- and 4-electrode measurement configuration was performed to determine if one technique would be more sensitive to impedance changes than the other in a microfluidic system. It was found that measuring a change in resistance using the 4-electrode configuration was the most sensitive technique to detect the presence of *E. coli* at low frequencies in a flow focusing system. The 2-electrode technique showed a greater percent change in capacitance than the 4-electrode sensor because the cells were bound to the electrode surface and the 2-electrode configuration is more sensitive to changes at the electrode interface. The presence of the bacteria became less significant with increased focusing. This effect was attributed to the increased effect of the diffusion of ions out of the focused stream as the focused stream height decreased. If diffusion is properly controlled in order to prevent a loss in detection sensitivity using flow focusing and impedance measurements, the 4-electrode measurement configuration would be the more ideal to monitor changes in impedance.

A large percentage of cell research is focused on drug discovery and development. As technology advances, research is moving away from two-dimensional cell cultures to three-dimensional spheroids to reproduce in-vivo like behavior with more accuracy. 2D cultures are easy to maintain and provide valuable baseline information; however, they do not reproduce certain properties such as drug resistance and clonal dominance. Most tissue consists of distinct 3D spatial arrangements of cells in close contact and communication with each other. In particular, 3D architecture and communication with extracellular matrix are essential to reproduce in-vivo like behavior. Various studies have shown that 3D spheroidal cell cultures demonstrate significantly more in-vivo like behavior than 2D cultures [123-125]. Yet, significant challenges still exist in using these models reliably in the laboratory or clinical setting. Monitoring of 3D spheroids using impedance spectroscopy has begun to take root within the past decade. Researchers including [126-128] have used impedance spectroscopy to perform toxicology studies and study changes in the physiological parameters of spheroids when exposed to various drugs.

This work has laid a foundation for 3D studies, as spatial resolution, statistically relevant data, the ability to distinguish between normal and cancer cells, and reduced measurement parasitic are all essential for electrically characterizing the effects of toxins and chemotherapeutic drugs on 3D spheroids. Fabrication of the electrode device on plastic, such as polypropylene, is encouraged for future work since cells, especially normal cells, are more conditioned to thrive on such substratum. Also, a more advanced graphical user interface (GUI) is suggested for easier data visualization and analysis.

List of References

1. Keese, C.R., et al., *Real-Time Impedance Assay to Follow the Invasive Activities of Metastatic Cells in Culture* BioTechniques, 2002. **33**(4): p. 842-850.

2. Giaever, I. and C.R. Keese, *Micromotion of Mammalian Cells Measured Electrically.* Proceedings of the National Academy of Sciences of the USA, 1991. **88**(17): p. 7896-7900.

3. Keese, C., et al., *Electrical wound-healing assay for cells in vitro.* Proceedings of the National Academy of Sciences, 2004. **101**(6): p. 1554-1559.

4. Campbell, C.E., et al., *Monitoring viral-induced cell death using electric cell-substrate impedance sensing.* Biosensors and Bioelectronics, 2007. **23**(4): p. 536-542.

5. Xiao, C. and J.H.T. Luong, *On-Line Monitoring of Cell Growth and Cytotoxicity Using Electric Cell-Substrate Impedance Sensing (ECIS).* Biotechnol. Prog., 2003. **19**(3): p. 1000-1005.

6. Lo, C.-M., C.R. Keese, and I. Giaever, *Monitoring Motion of Confluent Cells in Tissue Culture.* Experimental Cell Research, 1993. **204**(1): p. 102-109.

7. Yin, H., et al., *Bioelectrical Impedance Assay to Monitor Changes in Aspirin-Treated Human Colon Cancer HT-29 Cell Shape during Apoptosis.* Analytical Letters, 2007. **40**: p. 85-94.

8. Keese, C.R. and I. Giaever, *A biosensor that monitors cell morphology with electrical fields.* Engineering in Medicine and Biology Magazine, IEEE, 1994. **13**(3): p. 402-408.

9. Arndt, S., et al., *Bioelectrical impedance assay to monitor changes in cell shape during apoptosis.* Biosensors and Bioelectronics, 2004. **19**(6): p. 583-594.

10. Ko, K., et al., *Cell-substrate impedance analysis of epithelial cell shape and micromotion upon challenge with bacterial proteins that perturb extracellular matrix and cytoskeleton.* Journal of Microbiological Methods, 1998. **34**(2): p. 125-132.

11. Chen, Y., et al., *Real-time monitoring approach: Assessment of effects of antibodies on the adhesion of NCI-H460 cancer cells to the extracellular matrix.* Biosensors and Bioelectronics, 2008. **23**(9): p. 1390-1396.

12. Yeon, J.H. and J.-K. Park, *Cytotoxicity test based on electrochemical impedance measurement of HepG2 cultured in microfabricated cell chip.* Analytical Biochemistry, 2005. **341**(2): p. 308-315.

13. Wang, L., et al., *An automatic and quantitative on-chip cell migration assay using self-assembled monolayers combined with real-time cellular impedance sensing.* Lab Chip, 2008. **8**(6): p. 837-992.

14. Wegener, J., C.R. Keese, and I. Giaever, *Electric Cell-Substrate Impedance Sensing (ECIS) as a Noninvasive Means to Monitor the Kinetics of Cell Spreading to Artificial Surfaces.* Experimental Cell Research, 2000. **259**(1): p. 158-166.

15. McCoy, M.H. and E. Wang, *Use of electric cell-substrate impedance sensing as a tool for quantifying cytopathic effect in influenza A virus infected MDCK cells in real-time.* Journal of Virological Methods, 2005. **130**(1-2): p. 157-161.

16. DePaola, N., et al., *Electrical Impedance of Cultured Endothelium Under Fluid Flow.* Annals of Biomedical Engineering, 2001. **29**(8): p. 648-656.

17. Atienza, J.M., et al., *Dynamic Monitoring of Cell Adhesion and Spreading on Microelectronic Sensor Arrays.* Journal of Biomolecular Screening, 2005. **10**(8): p. 795-805.

18. Jemal, A., et al., *Cancer Statistics, 2010.* CA Cancer J Clin, 2010. **60**(5): p. 277-300.

19. AmericanCancerSociety, *Cancer Facts & Figures 2011*, in *Atlanta: American Cancer Society*. 2011.

20. Vassilopoulos, A., et al., *Identification and characterization of cancer initiating cells from BRCA1 related mammary tumors using markers for normal mammary stem cells.* Int J Biol Sci, 2008. **4**: p. 133-142.

21. Weinberg, R.A., *The biology of cancer*. 2007, New York: Garland Science, Taylor & Francis Group.

22. Goodman, P.C., *The new light: discovery and introduction of the X-ray.* American Journal of Roentgenology, 1995. **165**(5): p. 1041-1045.

23. Liu, Q., et al., *Impedance studies of bio-behavior and chemosensitivity of cancer cells by micro-electrode arrays.* Biosensors and Bioelectronics, 2009. **24**(5): p. 1305-1310.

24. Atkinson, A.J., et al., *Biomarkers and surrogate endpoints: Preferred definitions and conceptual framework*.* Clin Pharmacol Ther, 2001. **69**(3): p. 89-95.

25. Rifai, N., M.A. Gillette, and S.A. Carr, *Protein biomarker discovery and validation: the long and uncertain path to clinical utility.* Nat Biotech, 2006. **24**(8): p. 971-983.

26. Chabinyc, M.L., et al., *An Integrated Fluorescence Detection System in Poly(dimethylsiloxane) for Microfluidic Applications.* Anal. Chem., 2001. **73**: p. 4491-4498.

27. Wang, J., *Electrochemical biosensors: Towards point-of-care cancer diagnostics.* Biosensors and Bioelectronics, 2006. **21**(10): p. 1887-1892.

28. Ding, L., et al., *Trends in Cell-Based Electrochemical Biosensors* Current Medicinal Chemistry, 2008. **15**(30): p. 3160-70.

29. *Application Note: Basics of Electrochemical Impedance Spectroscopy*. Gamry Instruments 2007 [cited; Available from: http://www.gamry.com/App_Notes/EIS_Primer/EIS_Primer_2007.pdf].

30. Jorcin, J.-B., et al., *CPE analysis by local electrochemical impedance spectroscopy.* Electrochimica Acta, 2006. **51**(8-9): p. 1473-1479.

31. Barsoukov, E. and J.R. Macdonald, *Impedance spectroscopy: theory, experiment, and applications*. 2nd ed. 2005, Hoboken: John Wiley & Sons. 595.

32. Macdonald, J., *Impedance spectroscopy.* Annals of Biomedical Engineering, 1992. **20**(3): p. 289-305.

33. Macdonald, J.R., *Impedance spectroscopy: old problems and new developments.* Electrochimica Acta, 1990. **35**(10): p. 1483-1492.

34. Macdonald, J.R., J. Schoonman, and A.P. Lehnen, *Applicability and power of complex nonlinear least squares for the analysis of impedance and admittance data.* Journal of Electroanalytical Chemistry, 1982. **131**: p. 77-95.

35. Miklavi, D., N. Pavšelj, and F.X. Hart, *Electrical Properties of Tissues*, in *Wiley Encyclopedia of Biomedical Engineering* 2006, John Wiley & Sons, Inc.

36. Schwan, H.P., *Electrical Characteristics of Tissues.* Biophysik, 1963. **1**(3): p. 198-208.

37. Polk, C. and E. Postow, *Handbook of biological effects of electromagnetic fields*. 2nd ed. 1996, Boca Raton: CRC Press.

38. Tamura, T., et al., *Modelling of the dielectric properties of normal and irradiated skin.* Physics in Medicine and Biology, 1994. **39**(6): p. 927.

39. Schepps, J. and K. Foster, *The UHF and Microwave Dielectric Properties of Normal and Tumour Tissues: Variation in Dielectric Properties with Tissue Water Content.* Phys. Med. Biol., 1980. **25**(6): p. 1149-1159.

40. Luong, J.H.T., et al., *Monitoring Motility, Spreading, and Mortality of Adherent Insect Cells Using an Impedance Sensor*. 2001. p. 1844-1848.

41. AppliedBioPhysics. *Electric Cell-substrate Impedance Sensing ECIS*. 2010 [cited 2011 16 April]; Available from: http://biophysics.com/index.php.

42. Zou, Y. and Z. Guo, *A review of electrical impedance techniques for breast cancer detection.* Medical Engineering & Physics, 2003. **25**(2): p. 79-90.

43. Han, A., L. Yang, and A.B. Frazier, *Quantification of the Heterogeneity in Breast Cancer Cell Lines Using Whole-Cell Impedance Spectroscopy.* Clinical Cancer Research, 2007. **13**(1): p. 139-143.

44. Beetner, D.G., et al., *Differentiation among basal cell carcinoma, benign lesions, and normal skin using electric impedance.* Biomedical Engineering, IEEE Transactions on, 2003. **50**(8): p. 1020-1025.

45. Cone, C., *Transmembrane potentials and characteristics of immune and tumor cells*. 1985, Boca Raton, Florida: CRC Press.

46. Cure, J., *Cancer an electrical phenomenon.* Resonant, 1991. **1**(1).

47. Foster, K. and J. Schepps, *Dielectric properties of tumor and normal tissues at radio through microwave frequencies.* J Microwave Power, 1981. **16**: p. 107-119.

48. Luong, J., *An Emerging Impedance Sensor Based on Cell-Protein Interactions: Applications in Cell Biology and Analytical Biochemistry.* Analytical Letters, 2003. **36**(15): p. 3147 - 3164.

49. Luong, J.H.T. and M. Habibi-Rezaei, *Insect cell-based impedance biosensors: a novel technique to monitor the toxicity of environmental pollutants.* Environmental Chemistry Letters, 2003. **1**(1): p. 2-7.

50. Hug, T., *Biophysical methods for monitoring cell-substrate interactions in drug discovery.* Assay and Drug Development Technologies, 2003. **1**(3): p. 479-488.

51. Xi, B., et al., *Review: The application of cell-based label-free technology in drug discovery.* Biotechnology Journal, 2008. **3**: p. 484-495.

52. Marcottea, L. and M. Tabrizian, *General Review: Sensing surfaces: Challenges in studying the cell adhesion process and the cell adhesion forces on biomaterials* ITBM-RBM, 2008. **29**: p. 77-88.

53. Price, D., A. Rahman, and S. Bhansali, *Design rule for optimization of microelectrodes used in electric cell-substrate impedance sensing (ECIS).* Biosensors and Bioelectronics, 2009. **24**(7): p. 2071-2076.

54. Wegener, J., C.R. Keese, and I. Giaever, *Electric Cell–Substrate Impedance Sensing (ECIS) as a Noninvasive. Means to Monitor the Kinetics of Cell Spreading to Artificial Surfaces* Experimental Cell Research, 2000. **259**(1): p. 158-166.

55. Xing, J.Z., et al., *Dynamic Monitoring of Cytotoxicity on Microelectronic Sensors.* Chemical Research in Toxicology, 2005. **18**(2): p. 154-161.

56. Boyd, J.M., et al., *A cell-microelectronic sensing technique for profiling cytotoxicity of chemicals.* Analytica Chimica Acta, 2008. **615**(1): p. 80-87.

57. Xing, J.Z., et al., *Microelectronic cell sensor assay for detection of cytotoxicity and prediction of acute toxicity.* Toxicology in Vitro, 2006. **20**(6): p. 995-1004.

58. Irelan, J.T., et al., *Rapid and Quantitative Assessment of Cell Quality, Identity, and Functionality for Cell-Based Assays Using Real-Time Cellular Analysis.* Journal of Biomolecular Screening, 2011. **16**(3): p. 313-322.

59. Aberg, P., et al., *Skin cancer identification using multifrequency electrical impedance-a potential screening tool.* Biomedical Engineering, IEEE Transactions on, 2004. **51**(12): p. 2097-2102.

60. Huang, X., et al. *Impedance based biosensor array for monitoring mammalian cell behavior*. in *Proceedings of IEEE Sensors*. 2003.

61. Judy, J.W., *Microelectromechanical systems (MEMS): fabrication, design and applications.* Smart Materials and Structures, 2001. **10**: p. 1115-1134.

62. Rahman, A.R.A., G. Justin, and A. Guiseppi-Elie, *Towards an implantable biochip for glucose and lactate monitoring using microdisc electrode arrays (MDEAs).* Biomedical Microdevices, 2009. **11**(1): p. 75-85.

63. Park, T.H. and M.L. Shuler, *Integration of Cell Culture and Microfabrication Technology.* Biotechnol. Prog., 2003. **19**(2): p. 243-253.

64. Matysik, F.-M., A. Meister, and G. Werner, *Electrochemical detection with microelectrodes in capillary flow systems.* Analytica Chimica Acta, 1995. **305**(1-3): p. 114-120.

65. Bard, A.J. and L.R. Faulkner, *Electrochemical methods: Fundamentals and applications*. 2001, New York: Wiley and Sons.

66. Fosdick, L.E. and J.L. Anderson, *Optimization of microelectrode array geometry in a rectangular flow channel detector.* Anal. Chem, 1986. **58**(12): p. 2481-2485.

67. Min, J. and Antje J. Baeumner, *Characterization and Optimization of Interdigitated Ultramicroelectrode Arrays as Electrochemical Biosensor Transducers.* Electroanalysis, 2004. **16**(9): p. 724-729.

68. Sandison, M.E., et al., *Optimization of the Geometry and Porosity of Microelectrode Arrays for Sensor Design.* Anal. Chem., 2002. **74**(22): p. 5717-5725.

69. Lempka, S.F., et al. *Optimization of Microelectrode Design for Cortical Recording Based on Thermal Noise Considerations*. in *Engineering in Medicine and Biology Society, 2006. EMBS '06. 28th Annual International Conference of the IEEE*. 2006.

70. Wang, L., et al., *Analysis of the sensitivity and frequency characteristics of coplanar electrical cell-substrate impedance sensors.* Biosensors and Bioelectronics, 2008. **24**(1): p. 14-21.

71. English, A.E., et al., *Instrumental noise estimates stabilize and quantify endothelial cell micro-impedance barrier function parameter estimates.* Biomedical Signal Processing and Control, 2009. **4**(2): p. 86-93.

72. Curtis, T.M., et al., *Improved cell sensitivity and longevity in a rapid impedance-based toxicity sensor.* Journal of Applied Toxicology, 2009 (http://dx.doi.org/10.1002/jat.1421).

73. Pejcic, B. and R. De Marco, *Impedance spectroscopy: Over 35 years of electrochemical sensor optimization.* Electrochimica Acta, 2006. **51**(28): p. 6217-6229.

74. Rahman, A.R.A., D.T. Price, and S. Bhansali, *Effect of electrode geometry on the impedance evaluation of tissue and cell culture.* Sensors and Actuators B, 2007. **127**: p. 89-96.

75. Rahman, A., L. Chun-Min, and S. Bhansali, *A Detailed Model for High-Frequency Impedance Characterization of Ovarian Cancer Epithelial Cell Layer Using ECIS Electrodes.* Biomedical Engineering, IEEE Transactions on, 2009. **56**(2): p. 485-492.

76. Brooks Shera, E., et al., *Detection of single fluorescent molecules.* Chemical Physics Letters, 1990. **174**(6): p. 553-557.

77. Lee, G.B., et al., *Hydrodynamic focusing for a micromachined flow cytometer.* Transactions- ASME Journal of Fluids Engineering, 2001. **123**(3): p. 672-679.

78. Nieuwenhuis, J.H., et al., *Integrated Coulter counter based on 2-dimensional liquid aperture control.* Sensors & Actuators: B. Chemical, 2004. **102**(1): p. 44-50.

79. Wolff, A., et al., *Integrating advanced functionality in a microfabricated high-throughput fluorescent-activated cell sorter.* Lab on a Chip, 2003. **3**(1): p. 22-27.

80. Knight, J.B., et al., *Hydrodynamic focusing on a silicon chip: mixing nanoliters in microseconds.* Physical Review Letters, 1998. **80**(17): p. 3863-3866.

81. Wong, S.H., M.C.L. Ward, and C.W. Wharton, *Micro T-mixer as a rapid mixing micromixer.* Sensors and Actuators B: Chemical, 2004. **100**(3): p. 359-379.

82. Golden, J.P., et al., *A portable automated multianalyte biosensor.* Talanta, 2005. **65**(5): p. 1078-1085.

83. Schwan, H.P., *Electrode polarization impedance and measurements in biological materials.* Annals of the New York Academy of Sciences, 1968. **148**(1): p. 191.

84. York, T., *Status of electrical tomography in industrial applications.* Journal of Electronic Imaging, 2001. **10**: p. 608.

85. Schwan, H.P., *Electrode polarization impedance and measurements in biological materials.* Annals of the New York Academy of Sciences, 1968. **148**(Bioelectrodes): p. 191-209.

86. Bragós, R., et al. *Four versus two-electrode measurement strategies for cell growing and differentiation monitoring using electrical impedance spectroscopy*. in *Annual International Conference of the IEEE Engineering in Medicine and Biology Society*. 2006.

87. Huh, D., et al., *Microfluidics for flow cytometric analysis of cells and particles.* Physiologial Measurement, 2005. **26**(3): p. 73.

88. Nasir, M., et al., *Hydrodynamic focusing of conducting fluids for conductivity-based biosensors.* Biosensors and Bioelectronics, 2010. **25**(6): p. 1363-1369.

89. Bard, A.J. and L.R. Faulkner, *Electrochemical methods*. 2001: Wiley New York.

90. Hong, J., et al., *A dielectric biosensor using the capacitance change with AC frequency integrated on glass substrates.* Japanese Journal of Applied Physics, 2004. **43**(no. 8 a): p. 5639-5645.

91. Langereis, G.R., *An integrated sensor system for monitoring washing processes*, in *MESA+*. 1999, University of Twente: Enschede. p. 228.

92. Ivorra, A., *Contributions to the Measurement of Electrical Impedance for Living Tissue Ischemia Injury Monitoring*, in *Electronic Engineering Department*. 2005, Universitat Politècnica de Catalunya: Barcelona. p. 224.

93. Robillard, P.N. and D. Poussart, *Spatial resolution of four electrode array.* IEEE Transactions on Biomedical Engineering, 1979: p. 465-470.

94. Linderholm, P., et al., *Two-dimensional impedance imaging of cell migration and epithelial stratification.* Lab on a Chip, 2006. **6**(9): p. 1155-1162.

95. Hasted, J.B., D.M. Ritson, and C.H. Collie, *Dielectric properties of aqueous ionic solutions. Parts I and II.* The Journal of Chemical Physics, 1948. **16**: p. 1.

96. Robinson, R.A. and R.H. Stokes, *Electrolyte solutions*. 2002: Dover Pubns.

97. Olthuis, W., W. Streekstra, and P. Bergveld, *Theoretical and experimental determination of cell constants of planar-interdigitated electrolyte conductivity sensors.* Sensors and Actuators B: Chemical, 1995. **24**(1-3): p. 252-256.

98. Leatzow, D.M., et al., *Attachment of plastic fluidic components to glass sensing surfaces.* Biosensors and Bioelectronics, 2002. **17**(1-2): p. 105-110.

99. Chatrathi, M.P., J. Wang, and G. Collins, *Sandwich electrochemical immunoassay for the detection of Staphylococcal enterotoxin B based on immobilized thiolated antibodies.* Biosensors and Bioelectronics, 2007. **22**: p. 2932-2938.

100. Kamholz, A.E., et al., *Quantitative analysis of molecular interaction in a microfluidic channel: the T-sensor.* Anal. Chem, 1999. **71**(23): p. 5340-5347.

101. Yang, R., D.L. Feeback, and W. Wang, *Microfabrication and test of a three-dimensional polymer hydro-focusing unit for flow cytometry applications.* Sensors & Actuators: A. Physical, 2005. **118**(2): p. 259-267.

102. Ismagilov, R.F., et al., *Experimental and theoretical scaling laws for transverse diffusive broadening in two-phase laminar flows in microchannels.* Applied Physics Letters, 2000. **76**: p. 2376.

103. Weigl, B.H. and P. Yager, *Microfluidics: microfluidic diffusion-based separation and detection.* Science, 1999. **283**(5400): p. 346.

104. Hatch, A., et al., *A rapid diffusion immunoassay in a T-sensor.* Nature Biotechnology, 2001. **19**: p. 461-465.

105. Larsen, U.D., G. Blankenstein, and J. Branebjerg. *Microchip Coulter particle counter*. in *Solid State Sensors and Actuators, 1997. TRANSDUCERS'97 Chicago., 1997 International Conference on*. 1997.

106. Schwan, H.P. and C.F. Kay, *The conductivity of living tissues.* Annals of the New York Academy of Sciences, 1957. **65**(6): p. 1007.

107. Guillot, P. and A. Colin, *Stability of parallel flows in a microchannel after a T junction.* Physical Review E, 2005. **72**(6): p. 66301.

108. Giaever, I. and C.R. Keese, *Monitoring fibroblast behavior in tissue culture with an applied electric field.* PNAS, 1984. **81**(12): p. 3761-3764.

109. Varshney, M. and Y. Li, *Interdigitated array microelectrodes based impedance biosensors for detection of bacterial cells.* Biosensors and Bioelectronics, 2009. **24**(10): p. 2951-2960.

110. Mamouni, J. and L. Yang, *Interdigitated microelectrode-based microchip for electrical impedance spectroscopic study of oral cancer cells.* Biomedical Microdevices, 2011: p. 1-14.

111. Wegener, J., M. Sieber, and H.-J. Galla, *Impedance analysis of epithelial and endothelial cell monolayers cultured on gold surfaces.* Journal of Biochemical and Biophysical Methods, 1996. **32**(3): p. 151-170.

112. Arias, L.R., C.A. Perry, and L. Yang, *Real-time electrical impedance detection of cellular activities of oral cancer cells.* Biosensors and Bioelectronics, 2010. **25**(10): p. 2225-2231.

113. Hennemeyer, M., et al., *Cell proliferation assays on plasma activated SU-8.* Microelectronic Engineering, 2008. **85**(5-6): p. 1298-1301.

114. Opp, D., et al., *Use of electric cell-substrate impedance sensing to assess in vitro cytotoxicity.* Biosensors and Bioelectronics, 2009. **24**(8): p. 2625-2629.

115. Fesik, S.W., *Promoting apoptosis as a strategy for cancer drug discovery.* Nature Reviews Cancer, 2005. **5**(11): p. 876-885.

116. Smith, D.M., et al., *Arsenic trioxide induces a beclin-1-independent autophagic pathway via modulation of SnoN/SkiL expression in ovarian carcinoma cells.* Cell Death and Differentiation, 2010. **17**(12): p. 1867-1881.

117. Liu, G., et al., *Stanniocalcin 1 and Ovarian Tumorigenesis.* Journal of the National Cancer Institute, 2010. **102**(11): p. 812-827.

118. Nanjundan, M., et al., *Amplification of MDS1/EVI1 and EVI1, Located in the 3q26.2 Amplicon, Is Associated with Favorable Patient Prognosis in Ovarian Cancer.* Cancer Research, 2007. **67**(7): p. 3074-3084.

119. Nanjundan, M., et al., *Overexpression of SnoN/SkiL, amplified at the 3q26.2 locus, in ovarian cancers: A role in ovarian pathogenesis.* Molecular Oncology, 2008. **2**(2): p. 164-181.

120. Ren, J., et al., *Lysophosphatidic Acid Is Constitutively Produced by Human Peritoneal Mesothelial Cells and Enhances Adhesion, Migration, and Invasion of Ovarian Cancer Cells.* Cancer Research, 2006. **66**(6): p. 3006-3014.

121. Sun, T., et al., *Culture of skin cells in 3D rather than 2D improves their ability to survive exposure to cytotoxic agents.* Journal of Biotechnology, 2006. **122**(3): p. 372-381.

122. Grimnes, S. and O.G. Martinsen, *Bioimpedance and Bioelectricity Basics*. 2000, San Diego: Academic Press.

123. Carlsson, J. and T. Nederman, *Tumour spheroid technology in cancer therapy research.* Eur J Cancer Clin Oncol., 1989. **25**(8): p. 1127-1133.

124. Kunz-Schughart, L.A., et al., *The Use of 3-D Cultures for High-Throughput Screening: The Multicellular Spheroid Model* J Biomol Screen, 2004. **9**: p. 273-285.

125. Pampaloni, F. and E.H.K. Stelzer, *Three-Dimensional Cell Cultures in Toxicology.* Biotechnology and Genetic Engineering Reviews, 2009. **26**(1): p. 117-137.

126. Thielecke, H., A. Mack, and A. Robitzki, *Biohybrid microarrays – Impedimetric biosensors with 3D in vitro tissues for toxicological and biomedical screening.* Fresenius' Journal of Analytical Chemistry, 2001. **369**(1): p. 23-29.

127. Kloß, D., et al., *Drug testing on 3D in vitro tissues trapped on a microcavity chip.* Lab Chip, 2008. **8**: p. 879-884.

128. Hildebrandt, C., et al., *Detection of the osteogenic differentiation of mesenchymal stem cells in 2D and 3D cultures by electrochemical impedance spectroscopy.* Journal of Biotechnology, 2010. **148**(1): p. 83-90.

Appendices

Appendix A: Copyright Permissions

Gmail - image reprint https://mail.google.com/mail/?ui=2&ik=505087f247&view=pt&search=i...

Dorielle P <doriellep@gmail.com>

image reprint

2 messages

Dorielle Price <dorielle@mail.usf.edu> **Wed, May 12, 2010 at 1:58 PM**

To: keese@biophysics.com

Hello Dr. Keese,

I would like to know if I can reproduce an image (from Overview: What is ECIS) on your Biophysics website to use in my dissertation?

Thank you.

Dorielle

--

Dorielle T. Price

Bio-MEMS & Microsystems Lab
Dept. of Electrical Engineering
University of South Florida

Email: dorielle@mail.usf.edu
Website: http://mems.eng.usf.edu

Charles Keese <keese@biophysics.com> **Thu, May 13, 2010 at 10:07 AM**

To: Dorielle Price <dorielle@mail.usf.edu>

Hi Dorielle,

Yes, you certainly are welcome to use any figures from our website. Good luck with the dissertation.

Best

Charlie Keese

At 12:58 PM 5/12/2010, you wrote:

> Hello Dr. Keese,
>
> I would like to know if I can reproduce an image (from Overview: What is ECIS) on your Biophysics website to use in my dissertation?
>
> Thank you.
>
> Dorielle
>
> --
>
> Dorielle T. Price
>
> Bio-MEMS & Microsystems Lab
> Dept. of Electrical Engineering

1 of 2 5/13/2010 10:52 AM

Appendix A (Continued)

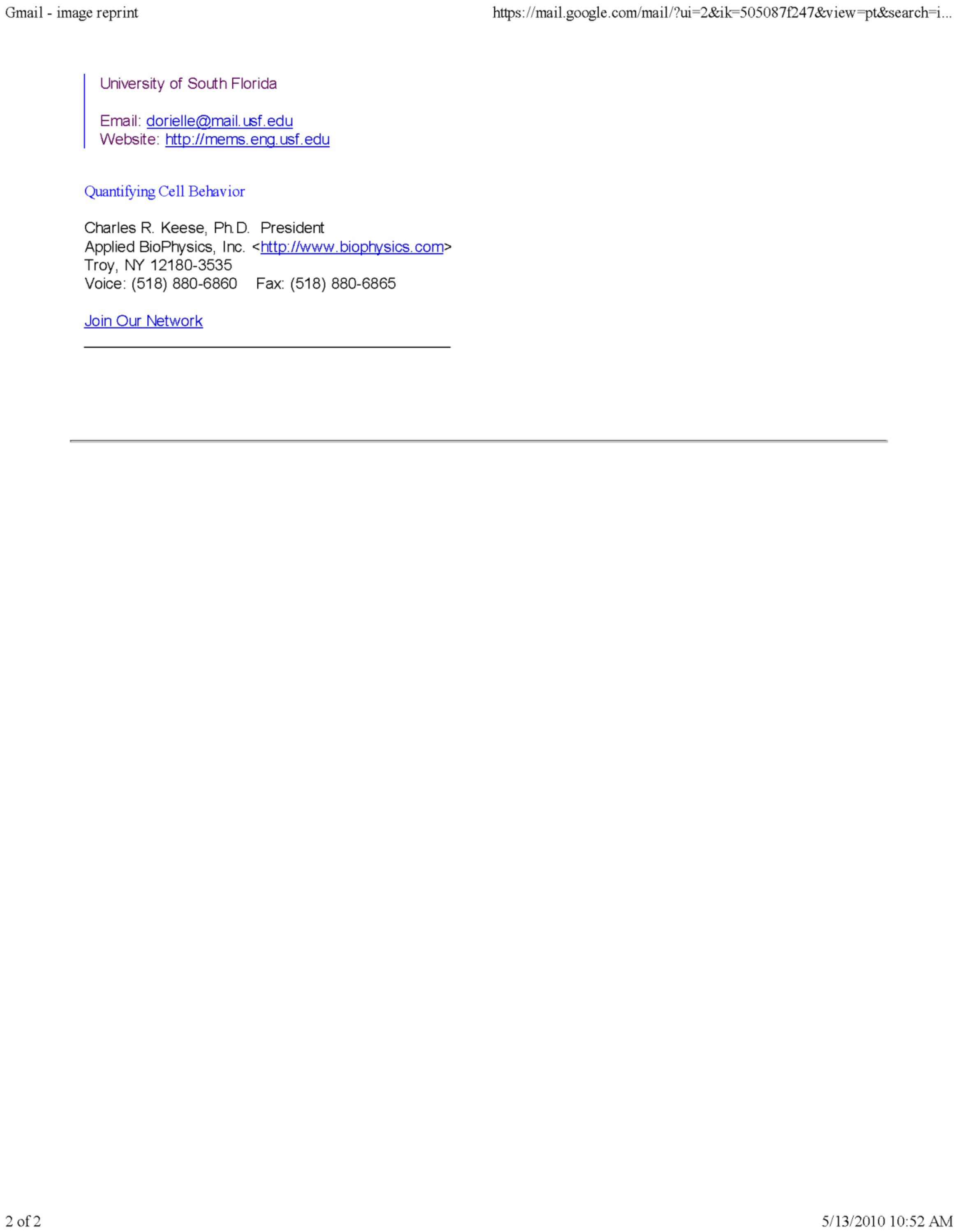

Gmail - image reprint https://mail.google.com/mail/?ui=2&ik=505087f247&view=pt&search=i...

University of South Florida

Email: dorielle@mail.usf.edu
Website: http://mems.eng.usf.edu

Quantifying Cell Behavior

Charles R. Keese, Ph.D. President
Applied BioPhysics, Inc. <http://www.biophysics.com>
Troy, NY 12180-3535
Voice: (518) 880-6860 Fax: (518) 880-6865

Join Our Network

2 of 2 5/13/2010 10:52 AM

Dorielle P <doriellep@gmail.com>

image reprint

2 messages

Dorielle Price <dorielle@mail.usf.edu> **Wed, May 5, 2010 at 10:43 AM**
To: info@biophysics.com

Hello,

Who can I contact to ask for permission to reproduce an image (from Overview: What is ECIS) on your website in my dissertation?

Thank you.

Dorielle

--
Dorielle T. Price

Bio-MEMS & Microsystems Lab
Dept. of Electrical Engineering
University of South Florida

Email: dorielle@mail.usf.edu
Website: http://mems.eng.usf.edu

Christian Renken <renken@biophysics.com> **Fri, Jun 18, 2010 at 2:49 PM**
To: Dorielle Price <dorielle@mail.usf.edu>

Hi Dorielle,

I am not sure if you got a reply, but please feel free to use that image.

Best Regards,

Christian

> **From:** doriellep@gmail.com [mailto:doriellep@gmail.com] **On Behalf Of** Dorielle Price
> **Sent:** Wednesday, May 05, 2010 10:43 AM
> **To:** info@biophysics.com
> **Subject:** image reprint
>
> [Quoted text hidden]

Appendix A (Continued)

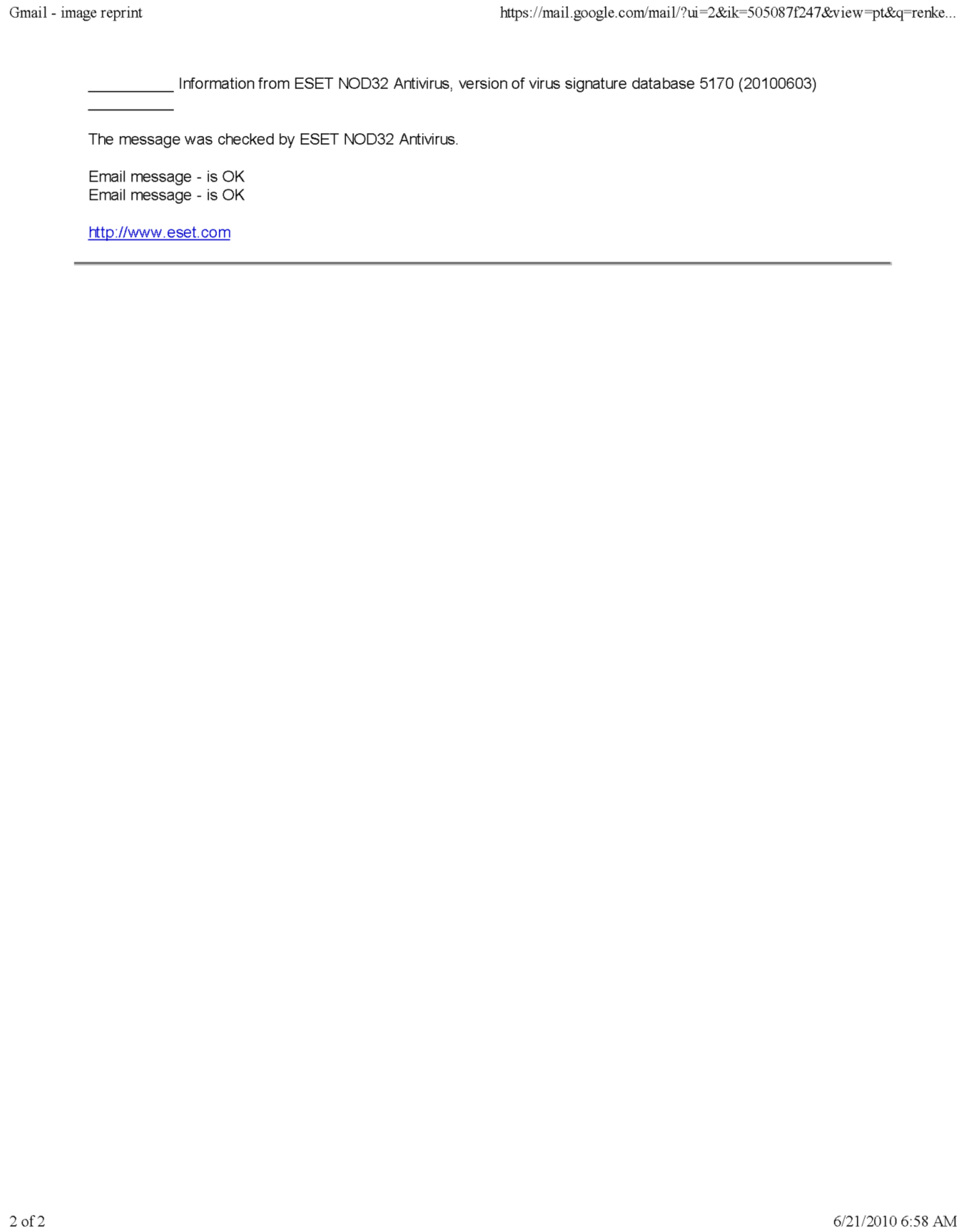

Gmail - image reprint https://mail.google.com/mail/?ui=2&ik=505087f247&view=pt&q=renke...

__________ Information from ESET NOD32 Antivirus, version of virus signature database 5170 (20100603) __________

The message was checked by ESET NOD32 Antivirus.

Email message - is OK
Email message - is OK

http://www.eset.com

2 of 2 6/21/2010 6:58 AM

Appendix A (Continued)

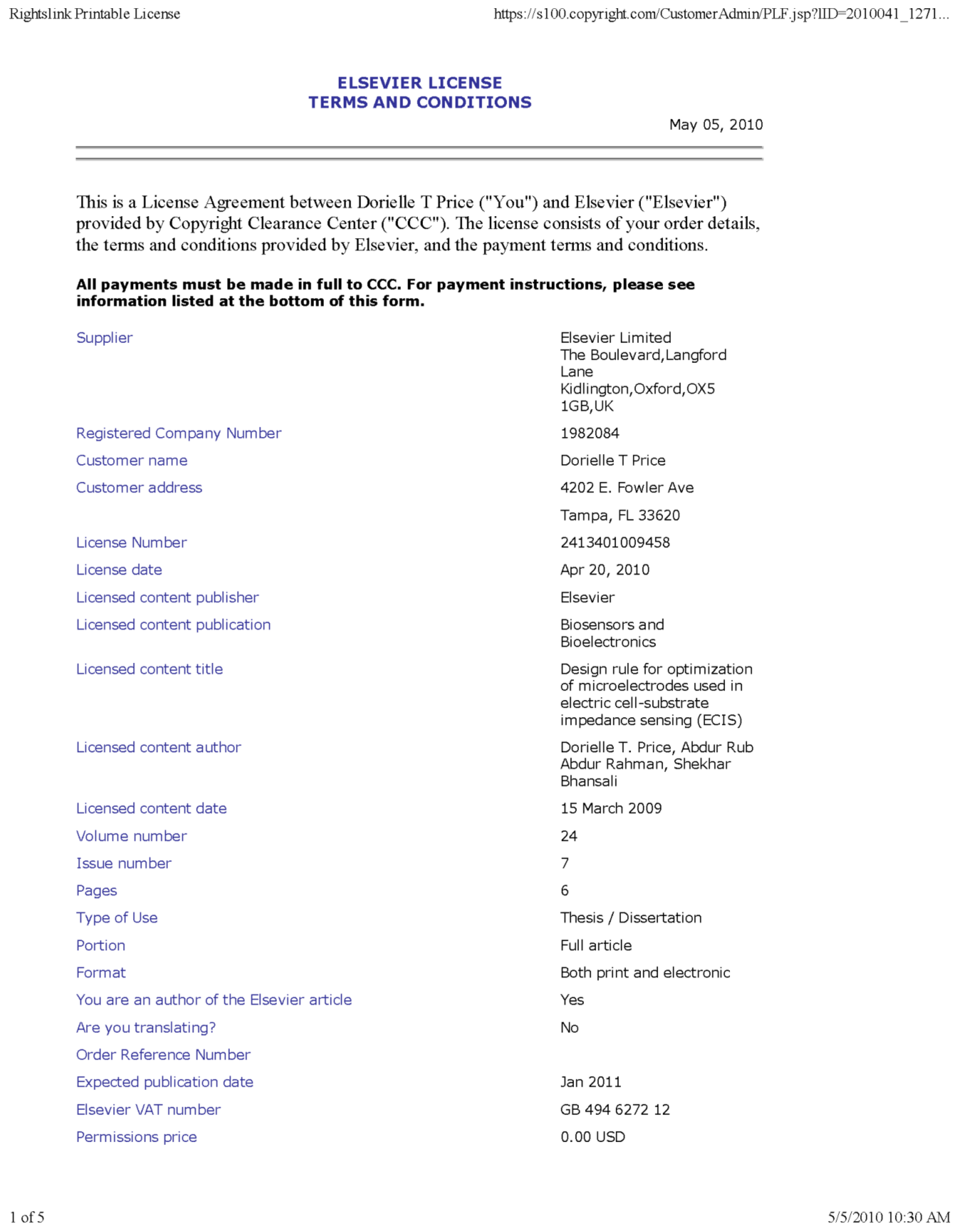

ELSEVIER LICENSE
TERMS AND CONDITIONS

May 05, 2010

This is a License Agreement between Dorielle T Price ("You") and Elsevier ("Elsevier") provided by Copyright Clearance Center ("CCC"). The license consists of your order details, the terms and conditions provided by Elsevier, and the payment terms and conditions.

All payments must be made in full to CCC. For payment instructions, please see information listed at the bottom of this form.

Supplier	Elsevier Limited The Boulevard,Langford Lane Kidlington,Oxford,OX5 1GB,UK
Registered Company Number	1982084
Customer name	Dorielle T Price
Customer address	4202 E. Fowler Ave
	Tampa, FL 33620
License Number	2413401009458
License date	Apr 20, 2010
Licensed content publisher	Elsevier
Licensed content publication	Biosensors and Bioelectronics
Licensed content title	Design rule for optimization of microelectrodes used in electric cell-substrate impedance sensing (ECIS)
Licensed content author	Dorielle T. Price, Abdur Rub Abdur Rahman, Shekhar Bhansali
Licensed content date	15 March 2009
Volume number	24
Issue number	7
Pages	6
Type of Use	Thesis / Dissertation
Portion	Full article
Format	Both print and electronic
You are an author of the Elsevier article	Yes
Are you translating?	No
Order Reference Number	
Expected publication date	Jan 2011
Elsevier VAT number	GB 494 6272 12
Permissions price	0.00 USD

Appendix A (Continued)

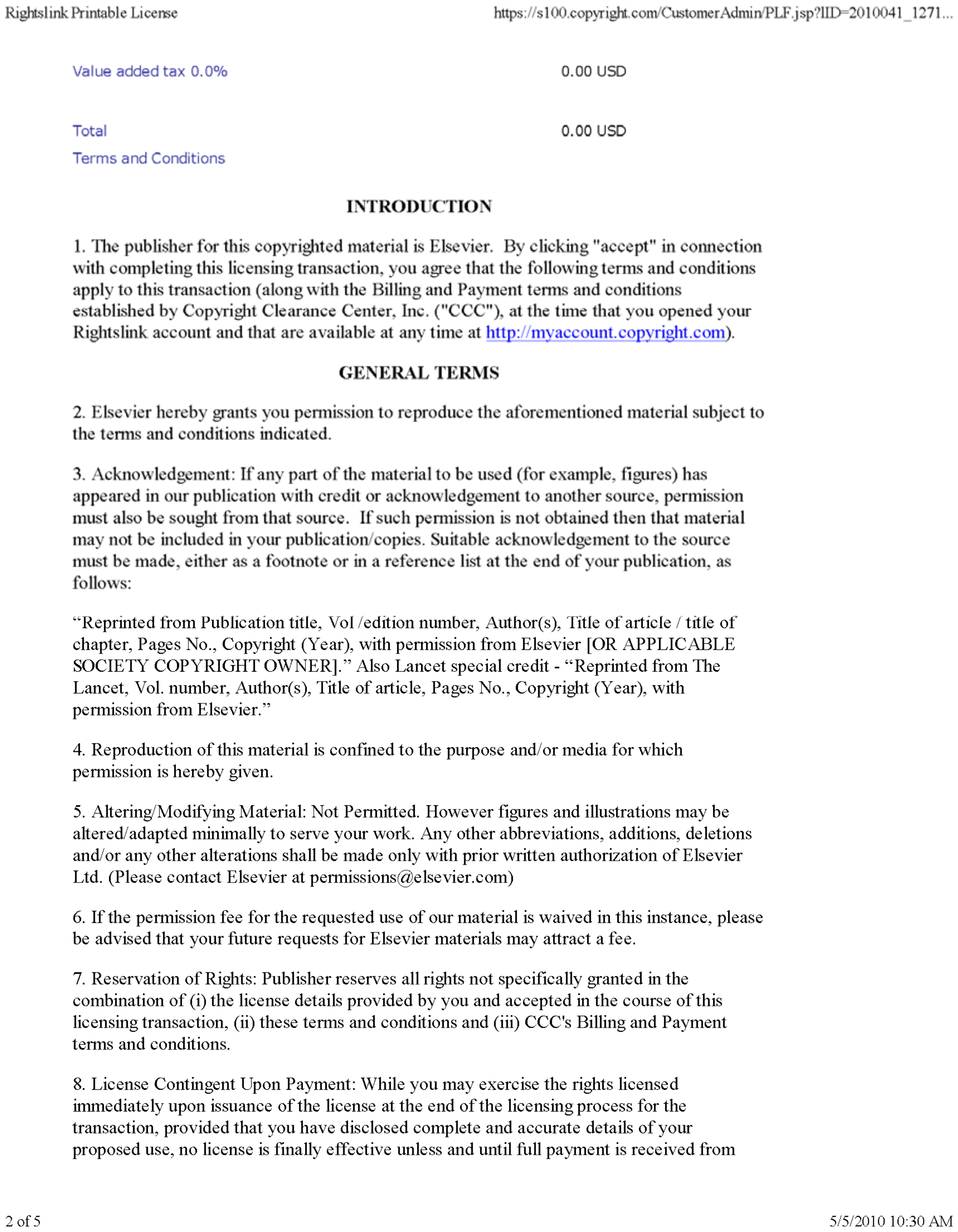

Value added tax 0.0%	0.00 USD
Total	0.00 USD

Terms and Conditions

INTRODUCTION

1. The publisher for this copyrighted material is Elsevier. By clicking "accept" in connection with completing this licensing transaction, you agree that the following terms and conditions apply to this transaction (along with the Billing and Payment terms and conditions established by Copyright Clearance Center, Inc. ("CCC"), at the time that you opened your Rightslink account and that are available at any time at http://myaccount.copyright.com).

GENERAL TERMS

2. Elsevier hereby grants you permission to reproduce the aforementioned material subject to the terms and conditions indicated.

3. Acknowledgement: If any part of the material to be used (for example, figures) has appeared in our publication with credit or acknowledgement to another source, permission must also be sought from that source. If such permission is not obtained then that material may not be included in your publication/copies. Suitable acknowledgement to the source must be made, either as a footnote or in a reference list at the end of your publication, as follows:

“Reprinted from Publication title, Vol /edition number, Author(s), Title of article / title of chapter, Pages No., Copyright (Year), with permission from Elsevier [OR APPLICABLE SOCIETY COPYRIGHT OWNER].” Also Lancet special credit - “Reprinted from The Lancet, Vol. number, Author(s), Title of article, Pages No., Copyright (Year), with permission from Elsevier.”

4. Reproduction of this material is confined to the purpose and/or media for which permission is hereby given.

5. Altering/Modifying Material: Not Permitted. However figures and illustrations may be altered/adapted minimally to serve your work. Any other abbreviations, additions, deletions and/or any other alterations shall be made only with prior written authorization of Elsevier Ltd. (Please contact Elsevier at permissions@elsevier.com)

6. If the permission fee for the requested use of our material is waived in this instance, please be advised that your future requests for Elsevier materials may attract a fee.

7. Reservation of Rights: Publisher reserves all rights not specifically granted in the combination of (i) the license details provided by you and accepted in the course of this licensing transaction, (ii) these terms and conditions and (iii) CCC's Billing and Payment terms and conditions.

8. License Contingent Upon Payment: While you may exercise the rights licensed immediately upon issuance of the license at the end of the licensing process for the transaction, provided that you have disclosed complete and accurate details of your proposed use, no license is finally effective unless and until full payment is received from

you (either by publisher or by CCC) as provided in CCC's Billing and Payment terms and conditions. If full payment is not received on a timely basis, then any license preliminarily granted shall be deemed automatically revoked and shall be void as if never granted. Further, in the event that you breach any of these terms and conditions or any of CCC's Billing and Payment terms and conditions, the license is automatically revoked and shall be void as if never granted. Use of materials as described in a revoked license, as well as any use of the materials beyond the scope of an unrevoked license, may constitute copyright infringement and publisher reserves the right to take any and all action to protect its copyright in the materials.

9. Warranties: Publisher makes no representations or warranties with respect to the licensed material.

10. Indemnity: You hereby indemnify and agree to hold harmless publisher and CCC, and their respective officers, directors, employees and agents, from and against any and all claims arising out of your use of the licensed material other than as specifically authorized pursuant to this license.

11. No Transfer of License: This license is personal to you and may not be sublicensed, assigned, or transferred by you to any other person without publisher's written permission.

12. No Amendment Except in Writing: This license may not be amended except in a writing signed by both parties (or, in the case of publisher, by CCC on publisher's behalf).

13. Objection to Contrary Terms: Publisher hereby objects to any terms contained in any purchase order, acknowledgment, check endorsement or other writing prepared by you, which terms are inconsistent with these terms and conditions or CCC's Billing and Payment terms and conditions. These terms and conditions, together with CCC's Billing and Payment terms and conditions (which are incorporated herein), comprise the entire agreement between you and publisher (and CCC) concerning this licensing transaction. In the event of any conflict between your obligations established by these terms and conditions and those established by CCC's Billing and Payment terms and conditions, these terms and conditions shall control.

14. Revocation: Elsevier or Copyright Clearance Center may deny the permissions described in this License at their sole discretion, for any reason or no reason, with a full refund payable to you. Notice of such denial will be made using the contact information provided by you. Failure to receive such notice will not alter or invalidate the denial. In no event will Elsevier or Copyright Clearance Center be responsible or liable for any costs, expenses or damage incurred by you as a result of a denial of your permission request, other than a refund of the amount(s) paid by you to Elsevier and/or Copyright Clearance Center for denied permissions.

LIMITED LICENSE

The following terms and conditions apply only to specific license types:

15. **Translation**: This permission is granted for non-exclusive world **English** rights only unless your license was granted for translation rights. If you licensed translation rights you may only translate this content into the languages you requested. A professional translator must perform all translations and reproduce the content word for word preserving the integrity of the article. If this license is to re-use 1 or 2 figures then permission is granted for

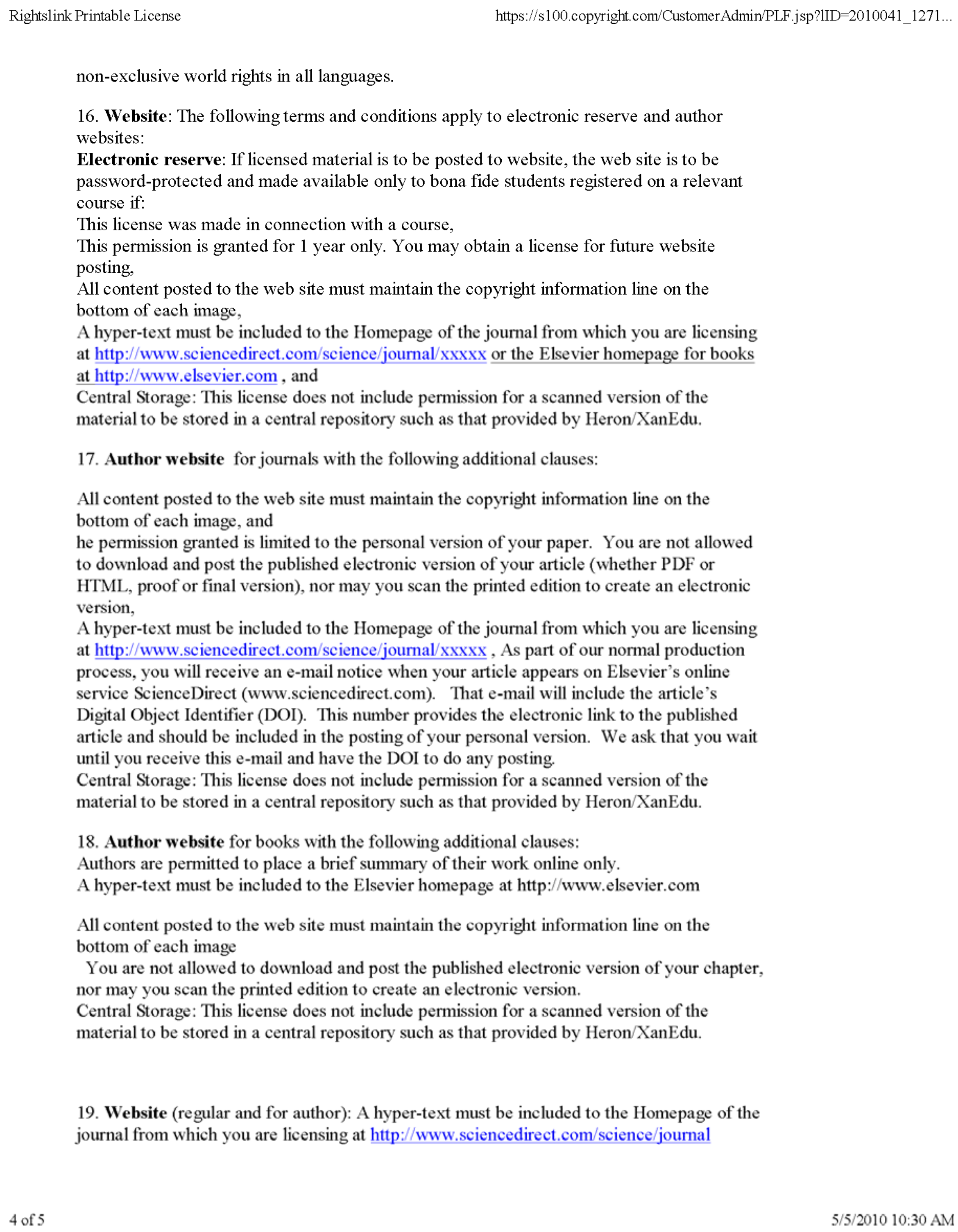

non-exclusive world rights in all languages.

16. **Website**: The following terms and conditions apply to electronic reserve and author websites:
Electronic reserve: If licensed material is to be posted to website, the web site is to be password-protected and made available only to bona fide students registered on a relevant course if:
This license was made in connection with a course,
This permission is granted for 1 year only. You may obtain a license for future website posting,
All content posted to the web site must maintain the copyright information line on the bottom of each image,
A hyper-text must be included to the Homepage of the journal from which you are licensing at http://www.sciencedirect.com/science/journal/xxxxx or the Elsevier homepage for books at http://www.elsevier.com , and
Central Storage: This license does not include permission for a scanned version of the material to be stored in a central repository such as that provided by Heron/XanEdu.

17. **Author website** for journals with the following additional clauses:

All content posted to the web site must maintain the copyright information line on the bottom of each image, and
he permission granted is limited to the personal version of your paper. You are not allowed to download and post the published electronic version of your article (whether PDF or HTML, proof or final version), nor may you scan the printed edition to create an electronic version,
A hyper-text must be included to the Homepage of the journal from which you are licensing at http://www.sciencedirect.com/science/journal/xxxxx , As part of our normal production process, you will receive an e-mail notice when your article appears on Elsevier's online service ScienceDirect (www.sciencedirect.com). That e-mail will include the article's Digital Object Identifier (DOI). This number provides the electronic link to the published article and should be included in the posting of your personal version. We ask that you wait until you receive this e-mail and have the DOI to do any posting.
Central Storage: This license does not include permission for a scanned version of the material to be stored in a central repository such as that provided by Heron/XanEdu.

18. **Author website** for books with the following additional clauses:
Authors are permitted to place a brief summary of their work online only.
A hyper-text must be included to the Elsevier homepage at http://www.elsevier.com

All content posted to the web site must maintain the copyright information line on the bottom of each image
You are not allowed to download and post the published electronic version of your chapter, nor may you scan the printed edition to create an electronic version.
Central Storage: This license does not include permission for a scanned version of the material to be stored in a central repository such as that provided by Heron/XanEdu.

19. **Website** (regular and for author): A hyper-text must be included to the Homepage of the journal from which you are licensing at http://www.sciencedirect.com/science/journal

Appendix A (Continued)

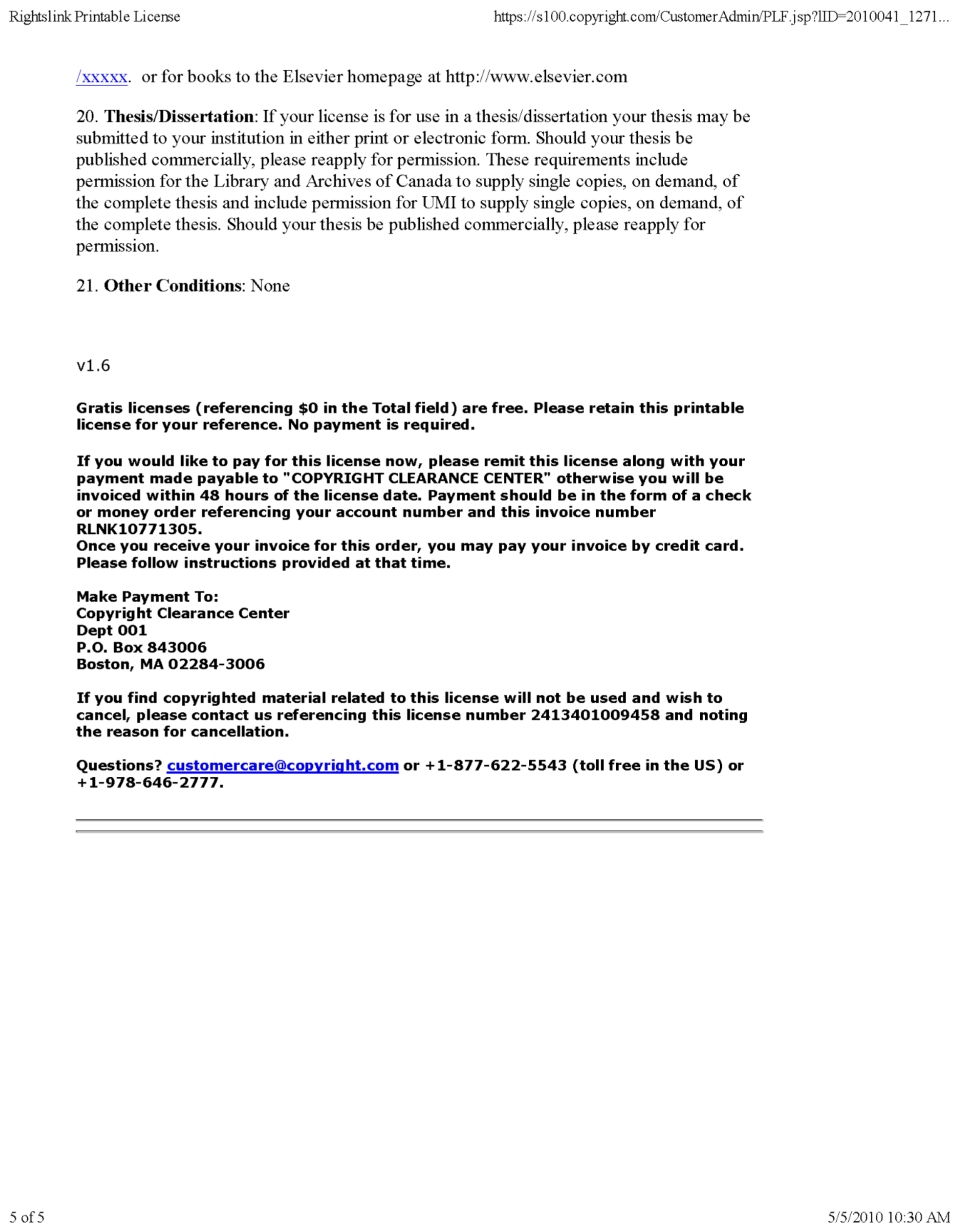

/xxxxx. or for books to the Elsevier homepage at http://www.elsevier.com

20. **Thesis/Dissertation**: If your license is for use in a thesis/dissertation your thesis may be submitted to your institution in either print or electronic form. Should your thesis be published commercially, please reapply for permission. These requirements include permission for the Library and Archives of Canada to supply single copies, on demand, of the complete thesis and include permission for UMI to supply single copies, on demand, of the complete thesis. Should your thesis be published commercially, please reapply for permission.

21. **Other Conditions**: None

v1.6

Gratis licenses (referencing $0 in the Total field) are free. Please retain this printable license for your reference. No payment is required.

If you would like to pay for this license now, please remit this license along with your payment made payable to "COPYRIGHT CLEARANCE CENTER" otherwise you will be invoiced within 48 hours of the license date. Payment should be in the form of a check or money order referencing your account number and this invoice number RLNK10771305.
Once you receive your invoice for this order, you may pay your invoice by credit card. Please follow instructions provided at that time.

Make Payment To:
Copyright Clearance Center
Dept 001
P.O. Box 843006
Boston, MA 02284-3006

If you find copyrighted material related to this license will not be used and wish to cancel, please contact us referencing this license number 2413401009458 and noting the reason for cancellation.

Questions? customercare@copyright.com or +1-877-622-5543 (toll free in the US) or +1-978-646-2777.

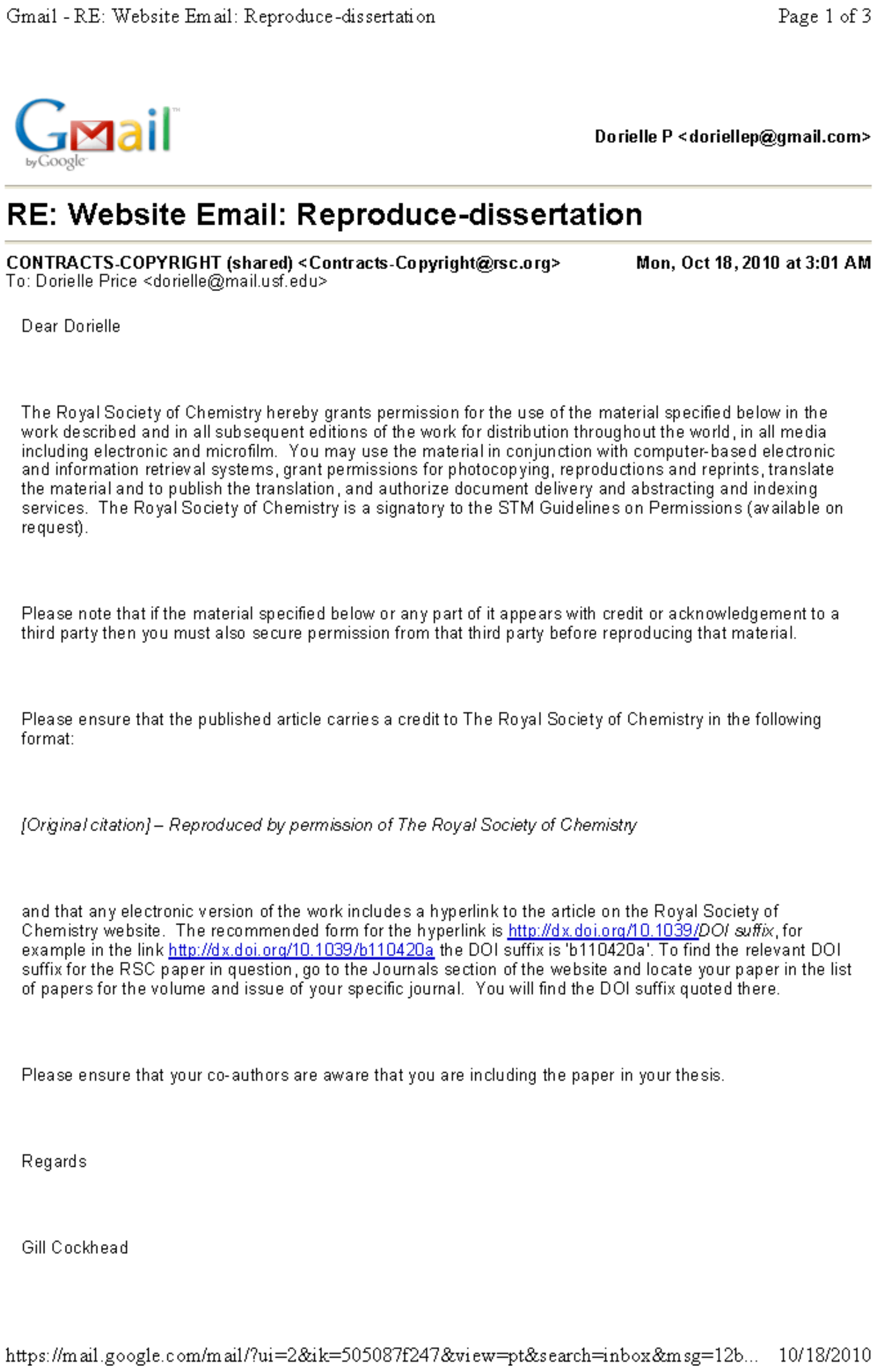

Gmail - RE: Website Email: Reproduce-dissertation

Page 1 of 3

Gmail by Google

Dorielle P <doriellep@gmail.com>

RE: Website Email: Reproduce-dissertation

CONTRACTS-COPYRIGHT (shared) <Contracts-Copyright@rsc.org> **Mon, Oct 18, 2010 at 3:01 AM**
To: Dorielle Price <dorielle@mail.usf.edu>

Dear Dorielle

The Royal Society of Chemistry hereby grants permission for the use of the material specified below in the work described and in all subsequent editions of the work for distribution throughout the world, in all media including electronic and microfilm. You may use the material in conjunction with computer-based electronic and information retrieval systems, grant permissions for photocopying, reproductions and reprints, translate the material and to publish the translation, and authorize document delivery and abstracting and indexing services. The Royal Society of Chemistry is a signatory to the STM Guidelines on Permissions (available on request).

Please note that if the material specified below or any part of it appears with credit or acknowledgement to a third party then you must also secure permission from that third party before reproducing that material.

Please ensure that the published article carries a credit to The Royal Society of Chemistry in the following format:

[Original citation] – Reproduced by permission of The Royal Society of Chemistry

and that any electronic version of the work includes a hyperlink to the article on the Royal Society of Chemistry website. The recommended form for the hyperlink is http://dx.doi.org/10.1039/*DOI suffix*, for example in the link http://dx.doi.org/10.1039/b110420a the DOI suffix is 'b110420a'. To find the relevant DOI suffix for the RSC paper in question, go to the Journals section of the website and locate your paper in the list of papers for the volume and issue of your specific journal. You will find the DOI suffix quoted there.

Please ensure that your co-authors are aware that you are including the paper in your thesis.

Regards

Gill Cockhead

https://mail.google.com/mail/?ui=2&ik=505087f247&view=pt&search=inbox&msg=12b... 10/18/2010

Appendix A (Continued)

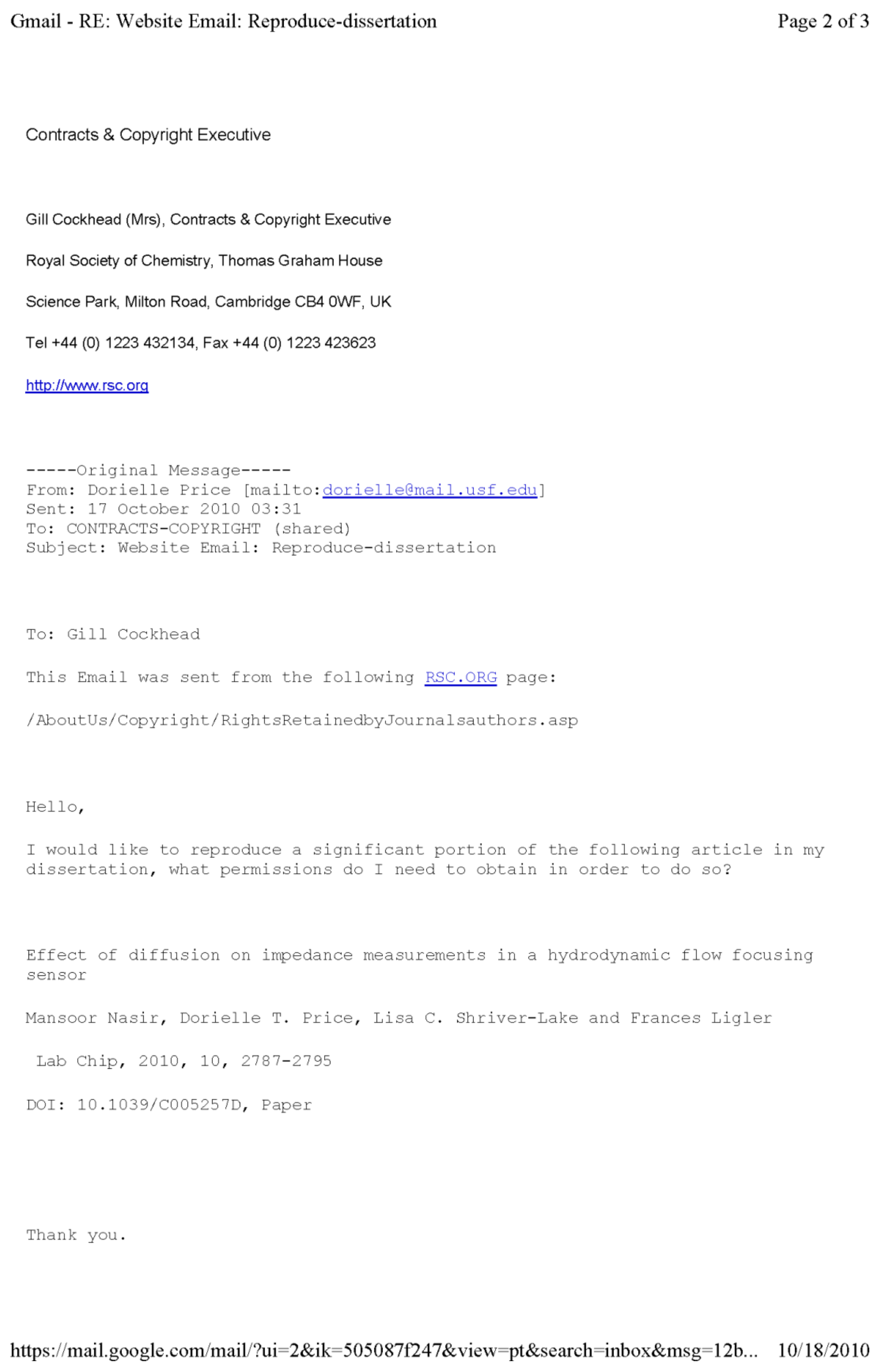

Gmail - RE: Website Email: Reproduce-dissertation Page 2 of 3

Contracts & Copyright Executive

Gill Cockhead (Mrs), Contracts & Copyright Executive

Royal Society of Chemistry, Thomas Graham House

Science Park, Milton Road, Cambridge CB4 0WF, UK

Tel +44 (0) 1223 432134, Fax +44 (0) 1223 423623

http://www.rsc.org

-----Original Message-----
From: Dorielle Price [mailto:dorielle@mail.usf.edu]
Sent: 17 October 2010 03:31
To: CONTRACTS-COPYRIGHT (shared)
Subject: Website Email: Reproduce-dissertation

To: Gill Cockhead

This Email was sent from the following RSC.ORG page:

/AboutUs/Copyright/RightsRetainedbyJournalsauthors.asp

Hello,

I would like to reproduce a significant portion of the following article in my dissertation, what permissions do I need to obtain in order to do so?

Effect of diffusion on impedance measurements in a hydrodynamic flow focusing sensor

Mansoor Nasir, Dorielle T. Price, Lisa C. Shriver-Lake and Frances Ligler

Lab Chip, 2010, 10, 2787-2795

DOI: 10.1039/C005257D, Paper

Thank you.

https://mail.google.com/mail/?ui=2&ik=505087f247&view=pt&search=inbox&msg=12b... 10/18/2010

Appendix A (Continued)

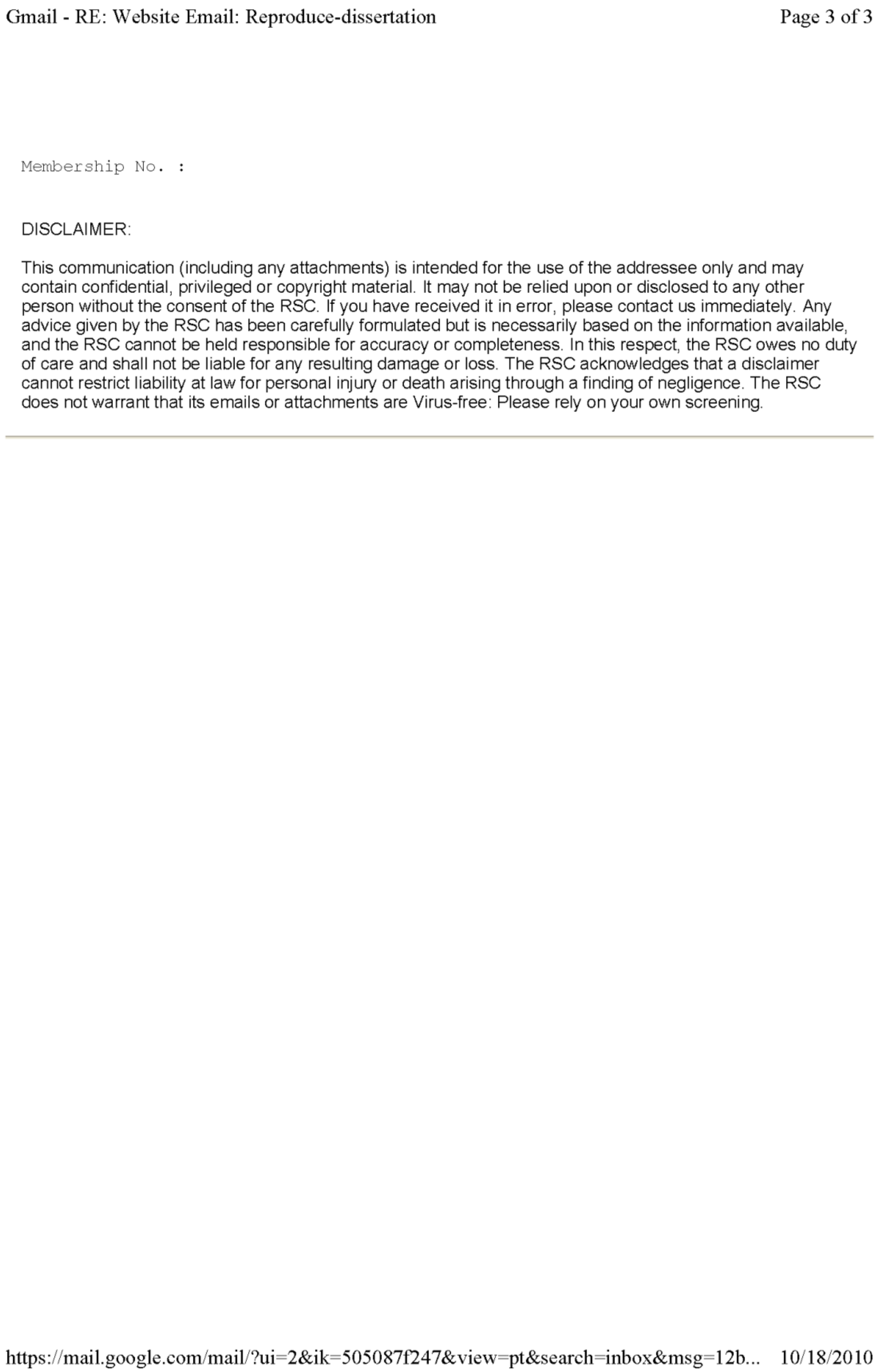

Gmail - RE: Website Email: Reproduce-dissertation Page 3 of 3

Membership No. :

https://mail.google.com/mail/?ui=2&ik=505087f247&view=pt&search=inbox&msg=12b... 10/18/2010

About the Author

Dorielle Tucker Price graduated *summa cum laude* with her B.S. from Clark Atlanta University (2005) and earned her M.S. from USF (2007) in Electrical Engineering. She is a recipient of the NSF Graduate Research Fellowship, McKnight Doctoral Fellowship (Florida Education Fund), Ford Foundation Predoctoral Diversity Fellowship programs. She has several peer-reviewed journal and conference publications, including one obtained from her 2009 internship with the Naval Research Laboratory in Washington, DC, under the advisement of Dr. Frances Ligler. She has recently (Spring 2012) completed her doctoral degree in Electrical Engineering, within the Bio-MEMS and Microsystems group, at the University of South Florida.